MULTINUCLEAR SOLID-STATE NMR OF FUEL CELL MATERIALS

by

SIMON TIMOTHY ORR

submitted for the degree

DOCTOR OF PHILOSOPHY

Department of Physics

University of Warwick

October 2010

Contents

List of Figures v
List of Tables x
List of Abbreviations xii
Acknowledgements xiv
Declaration xv
Abstract xvi

Chapter 1. Introduction 1

1.1 Introduction to Proton Exchange Membrane Fuel Cells 3
1.1.1 MEA Function, Design and Materials 5
1.1.2 Polymer Electrolyte Membrane Materials 7
1.1.3 PEMFC Catalyst Materials 10
1.2 Platinum(II) O,O'Dialkyldithiophosphates 12
1.2.1 The structure of Platinum(II) O,O'Dialkyldithiophosphates 12
1.3 Introduction to Borosilicate Glass and Ceramic Systems 13
1.3.1 The Structure of Borosilicate Glasses 14
1.3.2 ^{29}Si, ^{27}Al and ^{11}B NMR of Glasses and Ceramics 15

Chapter 2. Theory 17

2.1 Introduction 18
2.2 Interactions 21
2.2.1 Dipole-Dipole Coupling 22
2.2.2 Spin-Spin Coupling 22
2.2.3 Chemical Shift Anisotropy 23
2.2.4 The Knight Shift 24
2.2.5 Electric Quadrupole Coupling 26
2.3 The NMR Experiment 27
2.3.1 The Superconducting Magnet 27
2.3.2 The Probe and Coil 27
2.3.3 The Spectrometer 28
2.3.4 Magic Angle Spinning 29
2.4 NMR Techniques 30
2.4.1 One Pulse 30
2.4.2 Spin Echo 31
2.4.3 Wideline NMR Techniques 32
2.4.3.1 Frequency Stepped NMR 33
2.4.3.2 Field Sweep NMR 34
2.4.4 MQMAS 34
2.4.5 Cross Polarisation 35
2.4.6 Decoupling 36

Chapter 3. Experimental **38**

3.1 Proton Exchange Membranes 39
3.1.1 Sample Preparation 39
3.1.2 ^{19}F, ^{19}F-^{13}C and ^{1}H NMR 42
3.1.2.1 ^{1}H NMR 42
3.1.2.2 ^{19}F NMR 43
3.1.2.3 ^{13}C NMR 43
3.2 Fuel Cell Catalysts 44
3.2.1 Sample Preparation 44
3.2.2 ^{195}Pt Field Sweep NMR 45
3.2.3 ^{195}Pt Frequency Stepped NMR 46
3.3 Glass-Ceramics 47
3.3.1 Sample Preparation 47
3.3.2 ^{29}Si NMR 47
3.3.3 ^{27}Al NMR 47
3.3.4 ^{11}B NMR 48
3.4 Platinum(II) O,O'Dialkyldithiophosphates 48
3.4.1 Sample Preparation 48
3.4.2 ^{31}P NMR 49
3.4.3 ^{195}Pt NMR 49

Chapter 4. Proton Exchange Ionomers **51**

4.1 Introduction 52
4.2 ^{19}F and ^{1}H NMR of Proton Exchange Ionomers 52
4.2.1 ^{19}F NMR of Grated Proton Exchange Ionomers 52
4.2.2 ^{19}F and ^{1}H NMR of Rolled Proton Exchange Ionomers 56
4.3 ^{19}F and ^{1}H NMR of Cast Nafion Membranes 62
4.3.1 ^{19}F and ^{1}H NMR of Grated Cast Nafion Membranes 62
4.3.2 ^{19}F and ^{1}H NMR of Rolled Cast Nafion Membranes 75
4.3.3 ^{19}F-^{13}C NMR of Cast Nafion Membranes 86
4.4 ^{19}F and ^{1}H NMR of the Ionomer Component of Dried Nafion Inks 88
4.5 Undesirable effects of MAS on NMR Spectra of Ionomers 96
4.6 Conclusions 101

Chapter 5. Fuel Cell Catalysts **104**

5.1 Introduction 105
5.2 Point by Point ^{195}Pt NMR 105
5.3 Field Sweep ^{195}Pt NMR 109
5.4 Conclusions 116

Chapter 6. Aluminoborosilicate Glasses in the BN1 Ceramic **118**

6.1 Introduction 119
6.2 ^{27}Al NMR 119
6.2.1 One Dimensional Experiments 120

6.2.2 MQMAS 122
6.3 ^{11}B NMR 122
6.3.1 One Dimensional Experiments 124
6.3.2 MQMAS 124
6.4 ^{29}Si NMR 125
6.5 Discussion 127
6.6 Conclusions 132

Chapter 7. Crystalline Platinum (II) Dialkyldithiophosphates 133

7.1 Introduction 134
7.2 ^{31}P NMR 134
7.3 ^{195}Pt NMR 137
7.4 Conclusions 141

Chapter 8. Conclusions 142

8.1 Solid State NMR as a Probe of Complex Applied Materials 143
8.2 Proposed Further Study 144

References 147

List of Figures

Figure 1.1 : The separated layers of a membrane electrode assembly with the gas diffusion plates necessary to disperse reactants evenly over the catalyst surface. Adapted from [4]. p4

Figure 1.2: A schematic of a hydrogen PEMFC under operation. The broken lines outside the electrodes represent the gas permeable electrode support. p5

Figure 1.2: Diagram of the structure of PTFE based ionomers. The orientation of the polymer molecules is purely schematic. Taken from [22]. p8

Figure 1.3: TEM image of a platinum catalyst mounted on carbon. The large lighter spheres are the agglomerated carbon support upon which the smaller darker spots are the platinum particles. The ionomer coating of the catalyst is not visible at this scale. From [39]. p11

Figure 2.1: A schematic of the NMR experiment showing key equipment. p29

Figure 2.2: Example of a spin echo pulse sequence. p32

Figure 2.3: Example of a RAMP CP pulse sequence. p36

Figure 3.1: The chemical structures of (a) Nafion, (b) Solvay and (c) Aciplex ionomers. p40

Figure 4.1: Figure 4.1: Stacked plot of ^{19}F MAS NMR spectra of grated ionomers stored at 100% RH at standard temperature and pressure before packing. Inset: the region from -130 to -150 ppm is shown expanded. The structural groups to which nuclei belong are shown above their resonances. The manufacturer and equivalent weights are as follows; (a) Nafion EW 920, (b) Solvay EW 820, (c) Solvay EW 750, (d) Nafion EW 1100 and (e) Aciplex EW 1000. All spectra taken at 470 MHz, spinning at 30 kHz. p53

Figure 4.2: Overlaid plot of ^{19}F MAS NMR spectra of grated Solvay ionomers stored at 100% RH at standard temperature and pressure before packing. Both spectra taken at 470 MHz, spinning at 24 kHz. p55

Figure 4.5: Stacked plot of ^{19}F MAS spectra of rolled ionomers stored at 100% RH at standard temperature and pressure before packing. The manufacturer and quoted equivalent weights are as follows; (a) Nafion EW 920, (b) Solvay EW 820, (c) Solvay EW 750, (d) Nafion EW 1100 and (e) Aciplex EW 1000. All spectra taken at 470 MHz, spinning at 24 kHz. p57

Figure 4.6: Stacked plot of ^{1}H MAS spectra of water in rolled ionomers stored at 100% RH at standard temperature and pressure before packing . The manufacturer

and quoted equivalent weights are as follows; (a) Nafion EW 920, (b) Solvay EW 820, (c) Solvay EW 750, (d) Nafion EW 1100 and (e) Aciplex EW 1000. All spectra taken at 500 MHz, spinning at 12.5 kHz.

p61

Figure 4.7: Overlaid plot of ^{19}F MAS NMR spectra of a grated Nafion cast membrane stored in different humidity conditions. Spectra taken at 470 MHz, spinning at 24 kHz.

p63

Figure 4.8: Overlaid plot of ^{1}H MAS NMR spectra of water in grated Nafion cast membranes stored in different humidity conditions. Spectra taken at 500 MHz, spinning at 12.5 kHz.

p63

Figure 4.9: Stacked plot of ^{19}F MAS NMR spectra of grated Nafion cast membranes stored at 0% RH at standard temperature and pressure after packing. The membranes were cast and dried as follows; (a) aqueous solvent air dried, (b) aqueous solvent IR dried, (c) organic solvent air dried and (d) organic solvent IR dried. All spectra taken at 470 MHz, spinning at 24 kHz. p66

Figure 4.10: Stacked plot of ^{19}F MAS NMR spectra of grated Nafion cast membranes stored at 100% RH at standard temperature and pressure before packing. The membranes were cast and dried as follows; (a) aqueous solvent air dried, (b) aqueous solvent IR dried, (c) organic solvent air dried, (d) organic solvent IR dried. All spectra taken at 470 MHz, spinning at 24 kHz. p67

Figure 4.11: Stacked plot of ^{1}H MAS NMR spectra of water in grated Nafion cast membranes stored at 0% RH at standard temperature and pressure after packing. The membranes were cast and dried as follows; (a) aqueous solvent air dried, (b) aqueous solvent IR dried, (c) organic solvent air dried and (d) organic solvent IR dried. All spectra taken at 500 MHz, spinning at 12.5 kHz.

p68

Figure 4.12: Stacked plot of deconvoluted ^{1}H MAS NMR spectra of grated Nafion cast membranes stored at 0% RH at standard temperature and pressure after packing. The membranes were cast and dried as follows; (a) aqueous solvent air dried, (b) aqueous solvent IR dried, (c) organic solvent air dried and (d) organic solvent IR dried. All spectra taken at 500 MHz, spinning at 12.5 kHz. p70

Figure 4.13: Stacked plot of ^{1}H MAS NMR spectra of water in grated Nafion cast membranes stored at 100% RH at standard temperature and pressure before packing. The membranes were cast and dried as follows; (a) aqueous solvent air dried, (b) aqueous solvent IR dried, (c) organic solvent air dried, (d) organic solvent IR dried. All spectra taken at 500 MHz, spinning at 12.5 kHz. p72

Figure 4.14: Stacked plot of deconvoluted ^{1}H MAS NMR spectra of water in grated Nafion cast membranes stored at 100% RH at standard temperature and pressure before packing. The membranes were cast and dried as follows; (a) aqueous solvent air dried, (b) aqueous solvent IR dried, (c) organic solvent air dried. All spectra taken at 500 MHz, spinning at 12.5 kHz.

p73

Figure 4.15: Overlaid plot of ^{19}F spectra of rolled and grated Nafion cast membranes stored at ambient humidity before packing. Spectra taken at 470 MHz, spinning at 24 kHz. Spectra normalized to intensity of backbone peak.

p75

Figure 4.16: Overlaid plot of ^{1}H spectra of water in rolled and grated Nafion cast membranes stored at ambient humidity before packing. Spectra taken at 500 MHz, spinning at 12.5 kHz.

p76

Figure 4.17: Stacked plot of ^{19}F MAS NMR spectra of a rolled Nafion cast membrane kept at different temperatures during acquisition. Spectra taken at 470 MHz, spinning at 24 kHz. p78

Figure 4.18: Overlaid plot of ^{1}H MAS NMR spectra of water in a rolled Nafion cast membrane kept at different temperatures during acquisition. Spectra taken at 500 MHz, spinning at 12.5 kHz. p79

Figure 4.19: Overlaid plot of ^{19}F MAS NMR spectra of rolled Nafion cast membranes stored at 100% RH at standard temperature and pressure before packing. The temperature of the samples was regulated at 294K. All spectra taken at 470 MHz, spinning at 24 kHz. Spectra normalized to intensity of sidechain peaks. p80

Figure 4.20: Overlaid plot of ^{19}F MAS NMR spectra of rolled Nafion cast membranes stored at 100% RH at standard temperature and pressure before packing. The temperature of the samples was regulated at 343K. All spectra taken at 470 MHz, spinning at 24 kHz. Spectra normalized to intensity of sidechain peaks. p81

Figure 4.21: Overlaid plot of ^{1}H MAS NMR spectra of water in rolled Nafion cast membranes stored at 100% RH at standard temperature and pressure before packing. The temperature of the samples was regulated at 318K. All spectra taken at 500 MHz, spinning at 12.5 kHz. p82

Figure 4.22: Overlaid plot of ^{19}F MAS NMR spectra of rolled Nafion cast membranes stored at 0% RH at standard temperature and pressure after packing. All spectra taken at 470 MHz, spinning at 24 kHz. Spectra normalized to intensity of sidechain peaks. p83

Figure 4.23: Stacked plot of ^{1}H MAS NMR spectra of water in rolled Nafion cast membranes stored at 100% RH at standard temperature and pressure before packing. The temperature of the samples was regulated at 318K. The membranes were cast and dried as follows; (a) aqueous solvent air dried, (b) aqueous solvent IR dried, (c) organic solvent air dried, (d) organic solvent IR dried. All spectra taken at 500 MHz, spinning at 12.5 kHz. p84

Figure 4.24: Stacked plot of ^{19}F-^{13}C CP MAS NMR spectra of grated Nafion cast membranes stored at 100% RH at standard temperature and pressure before packing. The membranes were cast and dried as follows; (a) aqueous solvent air dried, (b) aqueous solvent IR dried, (c) organic solvent air dried, (d) organic solvent IR dried. All spectra taken at 75.5 MHz, spinning at 28 kHz. p87

Figure 4.25: Stacked plot of ^{19}F MAS NMR spectra of fuel cell catalyst inks stored at 100% RH at standard temperature and pressure before packing. The solvents and ionomer loadings were as follows: (a) aqueous solvent carbon ratio of 80, (b) aqueous solvent carbon ratio of 120, (c) organic solvent, carbon ratio of 80, (d) organic solvent, carbon ratio of 120. All spectra taken at 470 MHz, spinning at 24 kHz. p89

Figure 4.26: Stacked plot of ^{1}H MAS NMR spectra of water in fuel cell catalyst inks stored at 100% RH at standard temperature and pressure before packing. The solvents and ionomer loadings were as follows: (a) aqueous solvent carbon ratio of 80, (b) aqueous solvent carbon ratio of 120, (c) organic solvent, carbon ratio of 80, (d) organic solvent, carbon ratio of 120. All spectra taken at 500 MHz, spinning at 24 kHz.

p90

Figure 4.27: ^{1}H deconvoluted spectra of the ^{1}H MAS NMR spectra of water in fuel cell catalyst inks stored at 100% RH at standard temperature and pressure before packing. (a) organic ink with an ionomer carbon ratio of 80, (b) organic ink with an ionomer carbon ratio of 120. Spectra taken at 500 MHz, spinning at 24 kHz.

p91

Figure 4.28: Stacked plot of ^{19}F MAS NMR spectra of fuel cell catalyst inks stored at 0% RH at standard temperature and pressure after packing. The solvents and ionomer loadings were as follows: (a) aqueous solvent carbon ratio of 80, (b) aqueous solvent carbon ratio of 120, (c) organic solvent, carbon ratio of 80, (d) organic solvent, carbon ratio of 120. All spectra taken at 470 MHz, spinning at 24 kHz.

p93

Figure 4.29: Stacked plot of ^{1}H MAS NMR spectra of water in fuel cell catalyst inks stored at 0% RH at standard temperature and pressure after packing. The solvents and ionomer loadings were as follows: (a) aqueous solvent carbon ratio of 80, (b) aqueous solvent carbon ratio of 120, (c) organic solvent, carbon ratio of 80, (d) organic solvent, carbon ratio of 120. All spectra taken at 500 MHz, spinning at 12.5 kHz.

p94

Figure 4.30: ^{1}H deconvoluted spectra of ^{1}H MAS NMR spectra of water in fuel cell catalyst inks stored at 0% RH at standard temperature and pressure before packing. (a) aqueous ink with an ionomer carbon ratio of 80, (b) organic ink with an ionomer carbon ratio of 120. Spectra taken at 500 MHz, spinning at 12.5 kHz. p95

Figure 4.31: Overlaid plot of ^{19}F MAS NMR spectra at three different MAS speeds of rolled Nafion membrane cast from water and air dried, stored at 100% RH at standard temperature and pressure before packing. All spectra taken at 470 MHz. p97

Figure 4.32: Overlaid plot of a section of ^{19}F spectra at three different MAS speeds of rolled Nafion membrane cast from water and air dried, stored at 100% RH at standard temperature and pressure before packing. Samples were kept at 25°C by variable temperature control. All spectra taken at 470 MHz. p98

Figure 4.33: Overlaid plot of ^{1}H MAS NMR spectra at two different MAS speeds of water in a rolled Nafion membrane cast from water and air dried, stored at 100% RH at standard temperature and pressure before packing. Samples were kept at 25°C by variable temperature control. All spectra taken at 470 MHz. p99

Figure 4.34: Deconvolution of ^{1}H MAS NMR spectra of water in a rolled Nafion membrane cast from water and air dried, stored at 100% RH at standard temperature and pressure before packing. (a) spinning at 30kHz (b) spinning at 12.5 kHz. Samples were kept at 25°C by variable temperature control. Spectra taken at 470 MHz. p100

Figure 5.1: ^{195}Pt NMR spectrum of mesh325 platinum metal particles. p106

Figure 5.2: Point-by-point ^{195}Pt NMR spectrum of an unsupported platinum black. Particle size ~5nm. p107

Figure 5.3: Point-by-point ^{195}Pt NMR spectra of platinum (40% metal by weight) blacks supported on a graphitic carbon aggregate. (a) particle size 15 nm (b) particle size 7.7 nm. p108

Figure 5.4: ^{195}Pt Static Field Sweep NMR spectra of supported platinum blacks with different particles sizes. (a) 15 nm, (b) 7.7 nm, (c) 5 nm and (d) 1.8 nm. Sample (a) and (b) are 40% platinum by weight while (c) and (d) are 60% platinum. p110

Figure 5.5: ^{195}Pt deconvoluted static Field Sweep NMR spectra of supported platinum blacks with different particles sizes. (a) 15 nm, (b) 7.7 nm, (c) 5 nm and (d)

1.8 nm. Sample (a) and (b) are 40% platinum by weight while (c) and (d) are 60% platinum.

p112

Figure 6.1: Stacked plot of one pulse ^{27}Al NMR spectra of (a) BN1 as cast, (b) BN1 600 °C, (c) BN1 700 °C, (d) BN1 800 °C, (e) BN1 900 °C and (f) BN1 1000 °C. Acquisition at 156.2 MHz, spinning at 14880 Hz. p121

Figure 6.2: ^{27}Al z-filtered MQMAS spectra of (a) BN1 as cast, (b) BN1 800°C and (c) BN1 1000°C. All spectra acquired at 192.3 MHz spinning at 14880 kHz.

p123

Figure 6.3: Stacked plot of one pulse ^{11}B NMR spectra of (a) BN1 as cast, (b) BN1 600°C, (c) BN1 700°C, (d) BN1 800°C, (e) BN1 900°C, (f) BN1 1000°C. Acquisition at 192.3 MHz, spinning at 14880 Hz. p125

Figure 6.4: ^{11}B z-filtered MQMAS spectra of (a) BN1 as cast, (b) BN1 800°C, and (c) BN1 1000°C. All spectra acquired at 192.3 MHz spinning at 14880 Hz.

p126

Figure 6.5: Stacked plot of one pulse ^{29}Si NMR spectra of (a) BN1 as cast, (b) BN1 600°C, (c) BN1 700°C, (d) BN1 800°C, (e) BN1 900°C, (f) BN1 1000°C. Acquisition at 59.5 MHz, spinning at 4.5 kHz. p128

Figure 6.6: Stacked plot of deconvolutions of one pulse ^{29}Si NMR spectra of (a) BN1 as cast, (b) BN1 600°C, (c) BN1 700°C, (d) BN1 800°C, (e) BN1 900°C, (f) BN1 1000°C. Acquired at 59.5 MHz, spinning at 4.5 kHz. p129

Figure 7.1: Stacked ^{31}P MAS NMR of platinum (II) dialkyldithiophosphate complexes at 121.44 MHz (a): MAS speed 4 kHz, (b): MAS speed 2 kHz, inset: expanded view of isotropic peaks. p135

Figure 7.2: Stacked plot of ^{195}Pt field sweep NMR of all complexes, showing both experimental data (blue), and modelled CSA fits (green). p138

List of Tables

Table 3.1: Summary of ionomer containing samples received from JMTC. p40

Table 3.2: Summary of catalyst samples received from JMTC. p44

Table 3.3: Summary of Pt DTP samples received. p49

Table 4.1: Chemical shifts of each of the peaks in the assignment of the ^{19}F MAS NMR spectra of Nafion and Solvay Ionomers. The Nafion assignment from [35] is referenced to PTFE at –122ppm while the Solvay assignment is reference to PTFE at –123.2 ppm. The Nafion shifts have been adjusted to correct this discrepancy. p55

Table 4.2: Comparison of calculated and supplied values of the equivalent weight of Solvay ionomers. Ratio is expressed as a fraction of the supplier's value. p59

Table 4.3: ^{1}H NMR linewidths of water in rolled ionomers stored at 100% RH at standard temperature and pressure before packing. Ionomers are listed by manufacturer and equivalent weight. p61

Table 4.4: Deconvolution data for the fits of figures 4.12. Intensities are calculated by DMfit and given as a percentage of the total intensity of the fit (not the raw data) rounded to the nearest percent. Widths, also given by DMfit are FWHM in ppm. All peaks are a 50:50 weighted combination of Gaussian and Lorentzian lineshapes. p69

Table 4.5: Deconvolution data for the fits of figure 4.14. Intensities are calculated by DMfit and given as a percentage of the total intensity of the fit (not the raw data) rounded to the nearest percent. Widths, also given by DMfit are FWHM in ppm. p74

Table 4.6: ^{1}H NMR linewidths of rolled cast membranes stored at 100% RH at standard temperature and pressure before packing. p82

Table 4.7: ^{1}H NMR linewidths of rolled cast membranes stored at 0% RH at standard temperature and pressure before packing. p84

Table 4.8: Peak positions and widths from the deconvolutions of the spectra in figure 4.26-28. p92

Table 4.9: Peak positions and widths from the deconvolutions of the spectra in figure 4.30-31. p96

Table 4.10: Deconvolution data for the fits of figure 4.41. Intensities are calculated by DMfit and given as a percentage of the total intensity of the fit (not the raw data) to the nearest percent). Widths, also given by DMfit are FWHM in ppm. p100

Table 5.1: Positions and widths of all but the bulk peaks in the fits of figure 5.5 p111

Table 5.2: Comparison of relative peak intensities of fits displayed in figure 5.5 compared to those dictated by the layer model described in section 2.2.4. Errors in fit intensities are given below the corresponding result, for fit intensities of zero the maximum intensity within error, x, is denoted as + x. The discrepancy between experimental fit and theory are given below the values predicted by the model, these are presented as fit – model. Model particle sizes were as follows: (a) 14.90 nm 33 layers (b) 8.01 nm 18 layers, (c) 4.8 1nm 11 layers, (d) 1.62 nm 4 layers. p114

Table 5.3: Positions and widths of bulk peaks in the fits of figures 5-8. p115

Table 6.1: The NMR properties of the ^{27}Al nucleus. p119

Table 6.2: The NMR properties of Boron nuclei. p122

Table 6.3: The NMR properties of the ^{29}Si nucleus. p127

Table 6.4: Table of values of the fits shown in figure 6.6. p130

Table 7.1: ^{31}P chemical shift anisotropy parameters determined by analysis of the spinning sidebands of spectra in figure 7.1. p137

Table 7.2: ^{195}Pt chemical shift anisotropy parameters determined by the fits from figure 7.2. Errors supplied by DMfit except for $Pt\{S_2P(O\text{--}C_4H_9)_2\}_2$. p139

Table 7.3: Table of polymorphs of $Pt\{S_2P(O\text{-}C_4H_9)_2\}_2$ groups 1 and 2 are taken to be on the same ligand as are 3 and 4. p140

List of Abbreviations

δ	Chemical shift
δ_{aniso}	Chemical shift anisotropy parameter
η	Asymmetry parameter
θ	Angle between internuclear vector and applied field
μ	Magnetic moment
μ_0	Permeability of free space
σ	Chemical shielding
τ	Delay between pulses
φ_p	Phase of pulse
χ_Q	Quadrupolar coupling constant
ω	Frequency
ω_0	Larmor Frequency
ω_{ref}	Frequency of reference compound
B_0	Static applied magnetic field
B_1	Radio-frequency pulsed applied magnetic field
AqnAir	Aqueous solvent air dried
AqnIR	Aqueous solvent infra-red dried
BN	Bismuth Niobium
CP	Cross-polarisation
CSA	Chemical Shift Anisotropy
Cy	Cyclo-hexyl
D-LQH	Dielectrically-loaded quadrifilar helix
DAS	Dynamic angle spinning
DLA	Dielectrically-loaded antennae
DMFC	Direct methanol fuel cell
DOR	Double angle rotation
DOS	Density of states
EDS	Energy dispersive X-ray spectroscopy
E_f	Fermi energy
Et	Ethyl
EW	Equivalent weight
EXAFS	Extended X-ray absorption fine structure
FID	Free induction decay
FWHM	Full width half maximum
FT	Fourier transform
$\hbar$	Planck's constant divided by 2π
h	Planck's constant
$\hat{H}$	Hamiltonian
I	Nuclear spin
iPr	iso-propyl
IR	Infra-red
J	Spin-spin coupling constant
JM	Johnson-Matthey
JMTC	Johnson-Matthey technology centre
k	Boltzmann constant
K	Knight shift
LDOS	Local density of states
M	Magnetisation

MAS	Magic angle spinning
MEA	Membrane electrode assembly
$\boldsymbol{m_I}$	Spin angular momentum quantum number
MQ	Multiple quantum
MQMAS	Multiple quantum magic angle spinning
NBO	Non bridging oxygen
NMR	Nuclear magnetic resonance
OrgnAir	Organic solvent air dried
OrgnIR	Organic solvent infra-red dried
PEM	Proton exchange membrane
PEMFC	Proton exchange membrane fuel cell
Ppm	parts per million
PTFE	Polytetrafluoroethylene
q	Electric field gradient
Q	Electric quadrupole moment
$\boldsymbol{Q^n}$	Silicon species with *n* next nearest network forming neighbours
RC	Resistance Capacitance
RH	Relative Humidity
rf	Radio-frequency
SAXS	Small angle X-ray scattering
SEHS	Spin echo height spectroscopy
SEIS	Spin echo intensity spectroscopy
SEM	Scanning electron microscopy
SSNMR	Solid-state nuclear magnetic resonance
$\boldsymbol{T}$	Temperature
$\boldsymbol{T_1}$	Longitudinal relaxation time
$\boldsymbol{T_2}$	Transverse relaxation time
$\boldsymbol{T_2^*}$	Effective transverse relaxation time
TEM	Tunnelling electron microscopy
$\boldsymbol{U}$	Potential energy
XANES	X-ray absorption near edge structure
XRD	X-ray diffraction

Acknowledgements

I would like to thank the EPRSC and Johnson-Matthey for the funding of my project through the CASE scheme. Special thanks to my academic supervisors Prof. M. E. Smith and Dr. J. V. Hanna, and my industrial supervisors Dr. J. Fisher and Dr. D. Thompsett. Thanks is extended to whole of the solid-state NMR group at Warwick during my project, particularly to J. Griffin for helping me with the pulsed decoupling sequence for cross-polarisation experiments, to Dr. N. Barrow and G. Rees for support with MQMAS experiments and to Dr. K. Pike for various helpful discussions. Also to those at the Johnson-Matthey Technology Centre who prepared samples and shared information on materials and methods.

My other collaborators Prof. O. Antzutkin at the University of Warwick and the Lulea University of Technology and Prof. I. Reaney at the University of Sheffield are thanked for the opportunities and help offered.

Finally I would like to thank my fiancé Lisa for her love, support and patience and most of all the Lord Jesus Christ for the grace without which none of this would be possible.

Declaration

All work in this thesis is my own with the exception of sample preparation where noted, the Scherrer analysis carried out at JMTC and the spinning sideband analysis performed by Prof. Antzutkin. It was completed between October 2006 and October 2010 in the solid-state NMR group in the Department of Physics at the University of Warwick. No part of this thesis has been previously submitted for another degree. It is anticipated that the work in chapters 5, 6 and 7 will feature in three separate publications in recognised journals.

Signed ……

Date ……

Abstract

This thesis describes the application of multinuclear solid-state NMR to three materials systems: first, components of polymer-based proton-exchange fuel cells including the fluoropolymer membranes (Chapter 4) and the precious metal supported catalysts (Chapter 5); secondly, the formation of a complex bismuth niobium aluminoborosilicate glass-ceramic with novel dielectric properties (Chapter 6); finally, platinum (II) dialkyldithiophosphates which belong to a class of compounds (metal dialkyldithiophosphates) some of which are used in mineral separation processing (Chapter 7).

A full investigation into the effects of different conditions during sample preparation and ^{19}F NMR experiments on fluoropolymer membranes recommended unmilled preparation, dry storage and magic angle spinning below 24 kHz for the study of structural differences between membranes. The application of ^{19}F NMR to a range of commercial and experimental fluoropolymer membranes revealed that the equivalent weight does not affect the mobility of the polymer molecules such that can be detected by this technique. Calculations of equivalent weight from ^{19}F NMR differed with quoted values by up to 14%. Discrepancies were smallest in the short sidechain polymers, as low as 3%. The assignment of spectra was invariant with sidechain structure apart from a change in the number of ester links. The presence or absence of oxygen affected chemical shielding even around nuclei separated by several bonds. Differences in ^{1}H linewidths between membranes could not be interpreted without the control and comparison of manufacturing techniques. It is desirable to remove the necessity for organic solvents in membrane casting. However, membranes cast from aqueous solution do not possess the same properties as those from propanol. It had been proposed that rapid drying of water cast membranes would result in a structure more similar to those from organic solvent. ^{1}H NMR revealed that the opposite is the case, rapid drying makes the ordinarily more inhomogeneous aqueous membranes even more so. The application of both ^{19}F and ^{1}H NMR revealed that the monomolecular layers of fluoropolymer deposited on the surface of fuel cell catalysts to aid proton conductivity are categorically different in nature to the same materials in the bulk state. ^{19}F NMR suggests a polymer structure either more disordered, greatly less mobile or both. ^{1}H NMR displayed water environments that could not be reconciled to the standard model of rapid exchange between bulk water and water associated with acid groups. Spectral differences caused by solvent and polymer loading were discussed.

The first complete and quantitative Fourier transformed ^{195}Pt NMR spectra of platinum fuel cell catalysts, acquired using a field sweeping method, are analysed for deviation from the cubooctohedral particle model and surface oxidation.

A combination of ^{11}B, ^{27}Al and ^{29}Si studies of the BN1 ceramic system after different temperature heat treatments confirmed much of the previous work on phase evolution. However, it was shown that kyanite does not make up a significant proportion of the material until heat treatment reaches 1000 ºC and that aluminium impurities in bismuthbiobate crystals appear to increase with treatment temperature. The nature and abundance of glassy phases in the system are explored for the first time.

Field sweep ^{195}Pt NMR was employed to characterise the ^{195}Pt chemical shift anisotropy of five platinum (II) dialkyldithiophosphates complexes. Additionally the ^{31}P chemical shift anisotropies of two of the complexes, previously unpublished are presented

Chapter 1

1. Introduction

Solid state NMR spectroscopy is an increasingly important probe technique of materials. It is a method that is isotope specific, with only those that possess a magnetic moment of the nucleus accessible. The creation of nuclear magnetisation is usually brought about by the placing the sample in a high magnetic field (typically 4.7 - 21.1 T). The observation frequency is principally determined by the intrinsic magnetic moment of the nucleus, although other usually much smaller interactions that result from various interactions with of the nucleus with the surroundings exist and it is these interactions that provide information about the material. The key is the ability to interpret the spectral information to give new insight into the short-range structure and dynamics of a material. Short-range here means nearest neighbour and next nearest neighbour interactions, with the recent developments of the technique pushing the boundaries NMR can probe into the medium-range beyond this.

This thesis uses multinuclear solid state NMR to probe three materials systems:

- Components of polymer-based proton-exchange fuel cells including the fluoropolymer membranes (Chapter 4) and the precious metal supported catalysts (Chapter 5).
- Formation of a complex bismuth niobium aluminoborosilicate glass-ceramic with novel dielectric properties (Chapter 6).
- Platinum (II) dialkyldithiophosphates which belong to a class of compounds (metal dialkyldithiophosphates) some of which are used in mineral separation processing (Chapter 7).

The thesis is laid out as follows: the background to each of these systems is presented in more detail in the remainder of this chapter. Chapter 2 presents the physical background to the NMR technique while all the experimental details are provided in Chapter 3. The other four chapters present the data collected here and their analysis, as well as what this means for these technologically important systems. Suggestions are provided as to where further studies of these materials might be carried out.

1.1 Introduction to Proton Exchange Membrane Fuel Cells

Although the science behind fuel cell technologies has been understood since the 1830s [1] the social and economic drivers required for them to become more than a niche product in the energy conversion market have not existed until now. Fuel cells, like batteries, convert chemical energy into electrical energy, but unlike batteries they require a continuous external feed of reactants and the removal of products to function. All fuel cells share a common core design with two electrodes, electrically connected to an external circuit requiring power but also to one another by a medium which conducts positive, but not negative charges called the electrolyte. The main types of fuel cell are differentiated by the substance used as the electrolyte. Common electrolytes are phosphoric acid (PAFC), molten carbonate (MCFC), solid oxide (SOFC) and proton exchange membrane (PEMFC) which are the subject of this work [2-4]. For successful operation, especially in a commercial application, fuel cells require a number of components beyond the electrodes and electrolyte including the feeds of reactants and exhaust routes of products, pathways which allow the dispersion of substances over the reactive surfaces, physical supports and cooling apparatus. However, these aspects of fuel cell development are not the subject of this study. While the specific engineering solutions chosen for the above functions affect the conditions that a fuel cell must be optimised for only the materials which go into making the electrodes and electrolyte of a PEMFC will be considered.

Fuel cells, including the proton exchange membrane type (PEMFCs) along with other technologies that have the potential to reduce the amount of carbon dioxide produced by energy generation and distribution, have been the focus of renewed interest in the late 20^{th} and early 21^{st} Century. The potential for growth in PEMFC use is especially large as their high energy density and low temperature of operation allows them to compete in a wide variety of markets in which both combustion engine and battery technologies have been the norm. However, the high efficiency of fuel cells can be harnessed throughout the energy industry, a 200 kW gas power plant using phosphoric acid fuel cell technology has been developed in Japan which achieves an impressive 80% efficiency including recovery of thermal losses. Even larger generation plants with capacities an order of magnitude greater have been constructed from stacks of molten carbonate fuel cells, albeit with reduced efficiency

compared to PAFCs [5,6]. The proton exchange membrane fuel cell was first applied in the Germini space program, a 1 kW unit powered the spacecraft [7]. The first fuel cell car prototype was developed as early as the 1970s [8] but relied on alkaline fuel cells for its power rather than the PEMFCs found in modern fuel cell cars. More recently the DaimlerChrysler/Ballard/Ford NECAR 4 PEMFC car was specified to produce 70 kW from 320 fuel cells in stacks for a maximum range of 450 km using 100 litres of liquid hydrogen [9]. The development of PEMFCs is now most advanced for applications in which their inherent advantages, such as energy and power to weight ratios and harmless emissions, outweigh the premium in development and unit costs when compared to their competitors. Military, remote sensor and small scale remote energy generation are examples of areas in which PEMFCs are currently a commercially viable product without the consideration of environmental impact. Other markets, such as personal electronics, could see the introduction of PEMFCs within the next few years but for this to occur further progress must be made in the cost and efficiency of the core technology of the PEMFC, the membrane electrode assembly (MEA) [10-13].

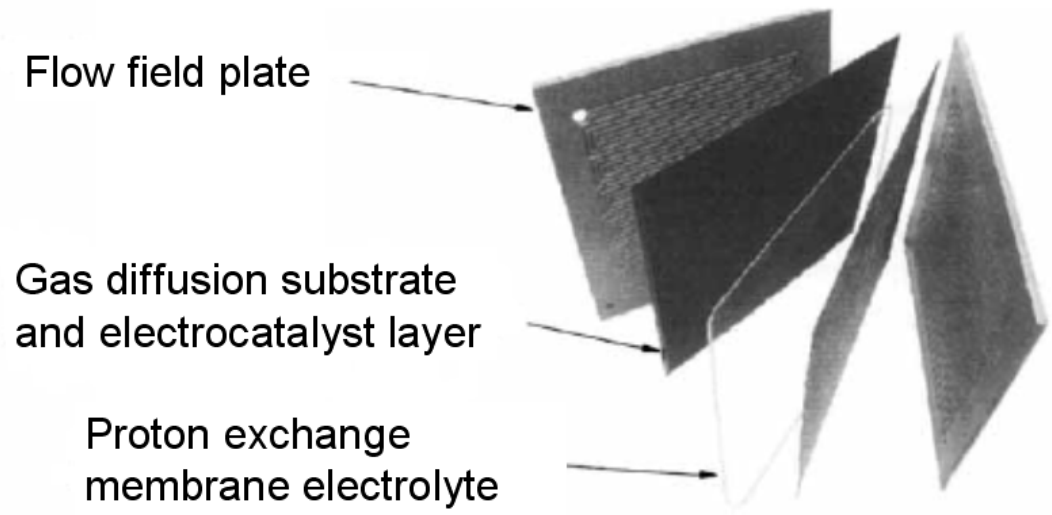

Figure 1.1: The separated layers of a membrane electrode assembly with the gas diffusion plates necessary to disperse reactants evenly over the catalyst surface. Adapted from [14].

1.1.1 MEA Function, Design and Materials

Like all fuel cells, PEMFCs are electrochemical cells that feature two electrodes separated by an electrolyte that conducts positive charges much more readily than negative charges. These components are sandwiched between surfaces which allow the even distribution of reactant gases to and removal of products from the electrodes. The example MEA in figure 1.1 shows a system with both diffusion plates and permeable substrate which is often a form of carbon. The reactions at both electrodes must be as efficient as possible so catalytic materials must be tailored separately for both the anode and cathode. Two different fuels are used in PEMFCs, hydrogen and methanol (direct methanol fuel cells, or DMFCs), each fuel presents its own challenges and requirements for MEAs, and both will be considered here. The main components of the MEA within a hydrogen PEMFC and the reactions that take place during operation are shown schematically in figure 1.2.

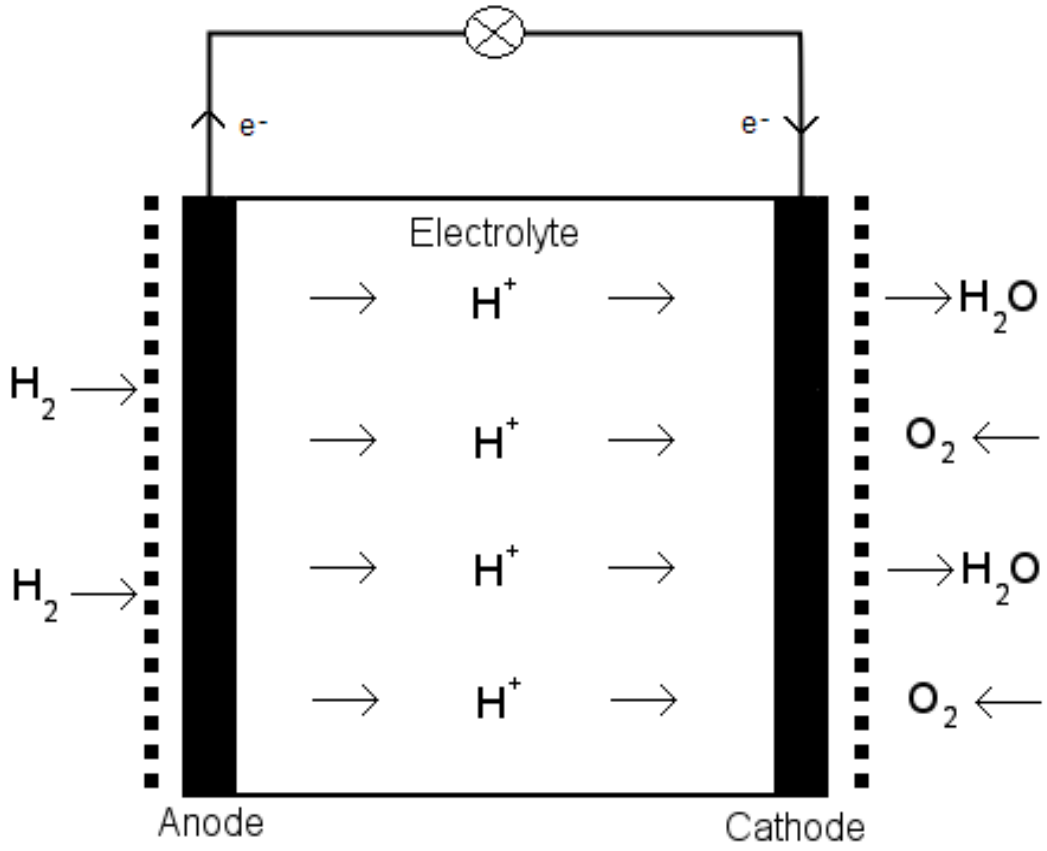

Figure 1.2: A schematic of a hydrogen PEMFC under operation. The broken lines outside the electrodes represent the gas permeable electrode support.

At the anode the fuel is oxidised and electrons are released to the circuit while the product protons are conducted by the electrolyte to the cathode. The anode reactions for molecular hydrogen and methanol are as follows:

$$H_2 \rightarrow 2e^- + 2H^+, \qquad [1.1]$$

$$CH_3OH + H_2O \rightarrow CO_2 + 6H^+ + 6e^-. \qquad [1.2]$$

Oxygen is required at the cathode and it is first reduced by combination with the electrons from the circuit:

$$O_2 + 4e^- \rightarrow 2O^{2-}. \qquad [1.3]$$

The oxygen then reacts with the protons produced at the anode to form water, which is the sole product of a hydrogen PEMFC:

$$O^{2-} + 2H^+ \rightarrow H_2O. \qquad [1.4]$$

The reactions in equations 1.1-1.4 all benefit from interaction with a platinum surface. Currently platinum or platinum alloy nanoparticles on a high surface area carbon support are the catalysts of choice for anode and cathode reactions in both hydrogen and methanol cells. Poisoning of the anode catalyst by species such as CO has led to other metals being alloyed with platinum in order to reduce efficiency losses, depending on the metal this can also reduce the material cost of the fuel cell [7, 15-16].

In order to maximize MEA efficiency optimal reaction conditions at both electrodes must be maintained. This creates additional requirements for the electrolyte material beyond excellent proton conductivity and charge selectivity. Firstly, the reagents and products must be kept well separated between the electrodes. The electrolyte must not be gas permeable and also restrict the amount of liquid cross-over, which is particularly relevant for DMFCs [17-18] but water management is also

a key challenge for hydrogen PEMFCs. Water produced at the cathode is absorbed and transported through the electrolyte by diffusive processes but is also pulled towards the cathode in the process of proton transport. As the materials used as electrolytes require water to increase proton conductivity [19-20]. Temperature of operation is key to fuel cell efficiency and the electrolyte must maintain its effectiveness at temperatures approaching and even exceeding 100°C [21]. As many of the applications envisioned for fuel cells would require tens of thousands of hours of use, and replacing the MEA would be very costly, any candidate material must be durable over this time scale under the heat and reducing/oxidising conditions of the MEA. DuPont's Nafion polymer has been the electrolyte material of choice for decades while development has focused on minor changes to polymer structure (such as the Dow Chemicals polymer) [22], impregnation of the membrane with other materials [23] or the control of the thickness and ordering of the solid membrane by various manufacturing methods [24-26].

1.1.2 Polymer Electrolyte Membrane Materials

The predominant understanding of the structure of sulfonated tetrafluoroethylene based ionic polymers such as Nafion assumes three phases in the solid material. However, the arrangement of these three phases is debated. Hydrophobic PTFE backbones bundle together and are coiled in a helix [27]. Neutron scattering and tunnelling electron microscopy (TEM) studies [21, 28-29] that reported water in the structure being bound in clusters of the order of 40 Å in diameter, an average of 70 Å apart and linked by water channels approximately 1 nm across supported the model suggested by Gierke [30] based on SAXS data. More recently a reinterpretation of the x-scattering work has proposed a parallel cylindrical water channels with a 2 nm average diameter [31]. The third phase linking the first two consists of the hydrophilic side chains, terminating in a sulphonic acid group, protruding into the water. A schematic of the structure is shown in figure 1.3. It is the nanoscale acid-water network that makes selective charge transport through the solid membrane possible [32].

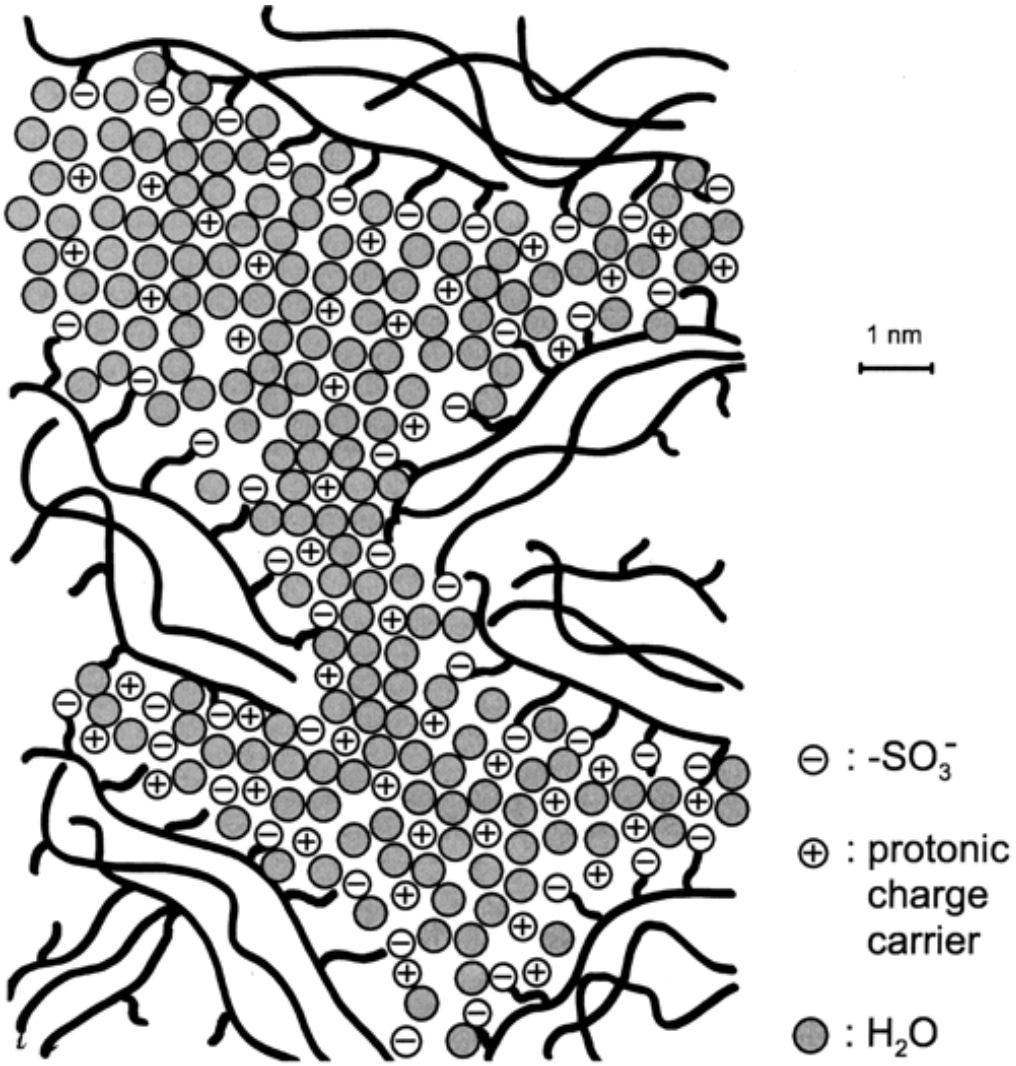

Figure 1.3: Diagram of the structure of PTFE based ionomers. The orientation of the polymer molecules is purely schematic. Taken from [22].

There have been many studies, summarised by [22, 33] of the structure and properties of these materials. This endeavour is made more complex by the dependence of both structure and properties on the humidity and temperature that the membrane experiences. These are key parameters in the function of a PEMFC and therefore must be considered and respected if any understanding gained is to be applied to real fuel cells. However, there is no single set of optimum conditions for PEMFCs, although in general higher temperatures of operation and water contents are desirable [11].

NMR work on PEMFC ionomers has been restricted to hydrogen, fluorine and carbon studies. ^{33}S NMR is very challenging given a mol content of less than 2% and

low isotopic abundance and ^{17}O NMR at natural abundance of 0.037% would require unrealistic experimental time scales if the oxygen nuclei that are part of the ionomer are to be detected. Each of the three studied nuclei will be considered in turn.

While there is no hydrogen in the structure of the ionomer itself, ^{1}H NMR of the water contained in the structure of proton exchange membranes has regularly appeared in the literature for many years [34-36]. The water network is the key to understanding the mechanism by which charges move through the material and combined with the ubiquitous nature of ^{1}H NMR it is unsurprising that so many studies have been conducted. While it would be expected that NMR would be able to distinguish water protons closely associated with acid groups from those that are more distant from them, given the technique's sensitivity to electronic environment, this is not the case. Exchange faster than the NMR time scale results in an averaging of the two resonances at a chemical shift between the two extremes which varies according to the abundance of protons in each state [37]. This makes ^{1}H NMR of ionomers very sensitive to water content as the proportion of 'bulk-like' water increases with water adsorption. While the water molecules being studied are in a liquid phase of the material they are inside a solid framework, which has resulted in both liquid [38-40] and solid-state [41-44] NMR treatments that provide different perspectives.

The NMR spectra acquired vary greatly in complexity, even within the range of static studies. Commercially purchased Nafion will give a single ^{1}H Gaussian peak, less than 0.5 ppm wide, its position and width varying with hydration [45]. The inverse proportionality between water content and peak width is explained by increasing water mobility. At the other extreme commercial Nafion dried by running air over the sample *in-situ* produced spectra with complex lineshapes, several ppm wide [40]. However, this broad lineshape is reduced to a single Gaussian with heating to 358 K, and remains as such on cooling to room temperature. In addition to water content and thermal history, other factors known to affect the ^{1}H spectra of ionomers include casting method [38,41,42] and sidechain length [35].

The assignment of the ^{19}F NMR spectrum of Nafion has only been settled relatively recently, and although the most abundant nucleus in the Nafion system it has not been as widely studied as ^{1}H NMR. Although ^{19}F NMR has a much larger

chemical shift range than ^{1}H (>200 ppm compared to ~35 ppm) the number of different chemical environments of fluorine in Nafion require high speed MAS to ensure resolution and that spinning sidebands (see section 2.3.4) can be distinguished and separated [45-46]. ^{19}F NMR has contributed to understanding of the mobility of both the sidechain and backbone of Nafion in the solid-state. It has been found that the mobility of the sidechain groups increases with distance from the branch point [47] and is dependent upon water content and temperature [48]. increasing either results in greater mobility. However, the mobility of fluorines on the backbone is affected by water content, but not detectably by temperature.

^{13}C NMR has only been attempted at natural abundance and in order to achieve high resolution this requires ^{19}F-^{13}C NMR in combination with magic angle spinning at speeds >15 kHz [49]. Using the ^{13}C static CSA and pseudo-2D ^{19}F-^{13}C experiments the backbone has been determined to be a stiff but rotating helix [46].

1.1.3 PEMFC Catalyst Materials

Increases in catalyst activity and reductions in their cost require ever more efficient catalysts. The most obvious way of achieving both goals is to maximize the proportion of platinum found at an accessible surface. It is for this reason that very small particles (1-7 nm in diameter) of platinum are supported on conglomerated graphite-like carbon particles, themselves only 20-30 nm across. A tunnelling electron microscope (TEM) image of such a catalyst is shown in figure 1.4.

In order for the electrode to function the catalyst surface must be in contact with the reactants while being linked to the external circuit by a conductor and to the electrolyte. Contact between the electrolyte and catalyst is achieved by dissolving the supported material with the electrolyte in a solvent. The mixture contains a ratio of carbons in the support to carbons in the ionomer of approximately 1:1. This liquid is called the catalyst ink and several methods are used to transfer it onto a porous carbon paper support that gives the electrode structure and provides the link to the circuit. Once dry the catalyst is left with a coating of ionomer electrolyte only a few molecules thick. This provides a route for protons to be conducted into the electrolyte once the MEA is assembled.

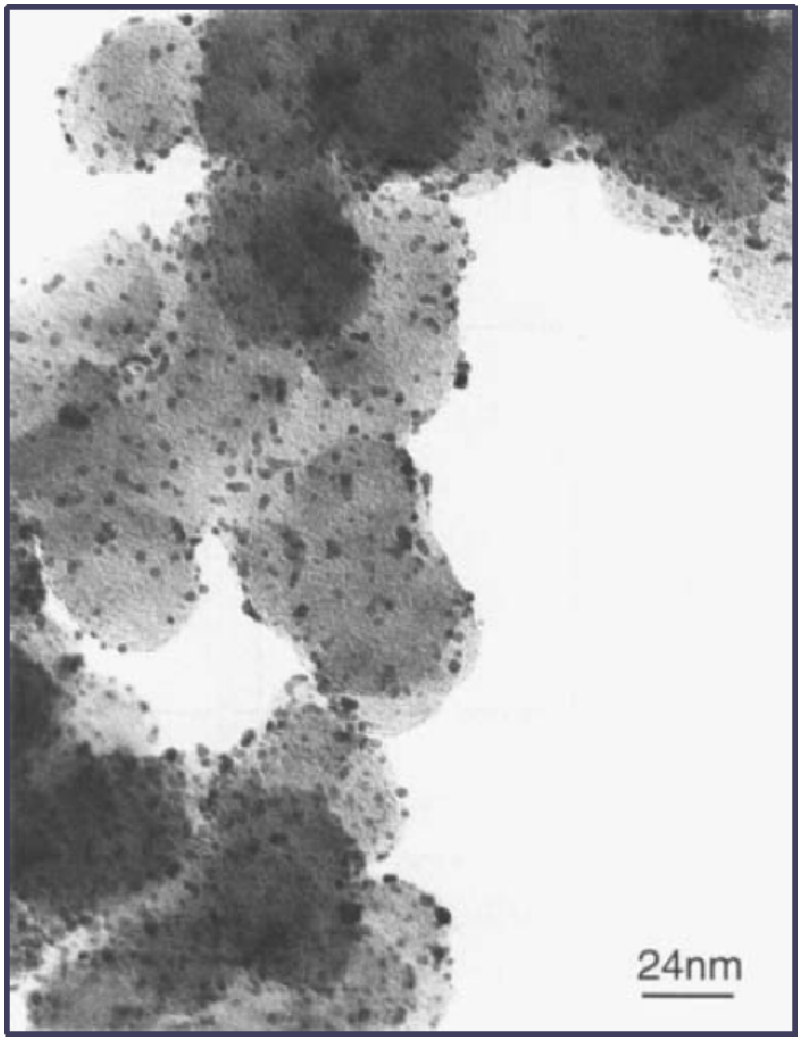

Figure 1.4: TEM image of a platinum catalyst mounted on carbon. The large lighter spheres are the agglomerated carbon support upon which the smaller darker spots are the platinum particles. The ionomer coating of the catalyst is not visible at this scale. From [50].

Counter intuitively, for cathode catalysts it has been found that particles approximately 5 nm across give the greatest catalyst activity per gram of platinum [51-53]. Even though smaller particles offer greater surface area per gram of metal their activity is not as high. Several reasons have been proposed for this. While it has been suggested that it is in fact the dispersion of the particles on the carbon surface that limits the effectiveness of smaller particle catalysts [54] most explanations centre on the properties of the platinum particles. Two of the variables that could be causing this size effect are the geometry and d-band vacancy of the metal particles.

Several analytical techniques have contributed to the understanding and development of these materials, including both imaging [55] and averaging analytical techniques such as XANES and EXAFS [56-58]. However, NMR is able to characterise the entirety of the catalyst while also supplying spatially specific information about the local electronic structure [59-66] and the effect of surface adsorbates [67-68]. This is key as it allows the local environment of the surface and the geometry of the particles to be distinguished. This is explored in section 2.2.4. It has become increasingly common [69-71] to analyse these materials in combination with electrochemical measurements or during operation but this study focuses on the application of solid-state NMR to samples which undergo extensive electrochemical measurements and testing at JMTC.

1.2 Platinum(II) O,O'Dialkyldithiophosphates

Transition metal dialkyldithiophosphates have long been of commercial and scientific interest due to the role they play in the separation of certain mineral components of mined ore in the flotation enrichment process [72]. For example, dialkyldithiophosphate ions can be used to isolate galena (a mineral form of lead sulphide) by precipitating it out of solution. Lead(II) dialkyldithiophosphates are formed on the surface of the galena particles which results in a change in the hydrophobic properties of the surface. This causes the galena to rise to the surface allowing it to be siphoned off from the mix. These compounds are also found as anti-oxidants and additives to lubrication oils for use in automotive engines [73]. The manner in which solid structures are formed from transition metal dialkyldithiophosphate molecules is dependent on the nucleus and ligand type with mono-, bi- and polynuclear configurations possible. While platinum(II) O,O'dialkyldithiophosphates of the form $Pt\{S_2P(O\text{-}R)_2\}_2$ are not yet used in the applications above it is hoped that the study of their solid structures will aid the understanding of the way in which ligands and metal atoms interact and bond with one another in the applications described above.

1.2.1 The structure of Platinum(II) O,O'Dialkyldithiophosphates

Given that many platinum(II) O,O'dialkyldithiophosphates have melting points below or close to room temperature, few have been previously studied in crystalline

form [74]. It has been found that there is a significant degree of variation in both molecular and supramolecular structure between dithiophosphates that vary only in the terminal R groups. Therefore generalisations to the whole series of complexes with the same metal nucleus cannot be relied upon and that each ligand species must be studied individually to be understood [75]. The studies that have been conducted identify a common PtS_4 chromophore at the centre of the molecule which shows some distortion of the square planar orientation found in the mineral Cooperite (PtS) [76-77]. X-ray diffraction analysis has found that the PtS bond distances are invariant across the series R = Et, ^{i}Pr and Cy [75]. While a single value for the isotropic chemical shift of ^{31}P NMR of $Pt\{S_2P(O\text{-}C_4H_9)_2\}_2$ suggests structural equivalence between dithiophosphate fragments in the same molecule, in equivalent adjacent butyl chains are indicated by peak splitting in the ^{13}C NMR. In summary, all existing analysis suggests that if the solid-state structural differences between complexes are to be explained it is the arrangement and interaction between the alkyl ligands which requires the most in depth consideration.

It has been shown that the chemical shift anisotropies of both the platinum and phosphorus nuclei can be useful for determining the geometry of dialkyldithiophosphate complexes [75, 77-78]. While some information pertaining to the ^{195}Pt chemical shift anisotropy of these materials has been deduced from magic angle spinning (MAS) NMR, the Pt chemical shift anisotropy (CSA) is usually too large for acquisition at a single frequency. A full analysis of the CSA has yet to be made, but previous work has shown that a clear difference between the Pt CSA of Cooperite (PtS) and platinum dialkyldithiophosphates exists [75-78].

1.3 Introduction to Borosilicate Glass and Ceramic Systems

A common problem encountered in the design of mobile communication devices is the issue of body-loading. That is to say variations in the performance of the antenna are caused by a disruption of the electromagnetic field close to the device (the near-field) by the dielectric effect of the users body. Dielectrically loaded antennas (DLAs) are an attempt to make the variations caused by body-loading more predictable. While two main designs exist, it has been shown that dielectric-loaded quadrifilar helix (D-LQH) antennae can provide better performance using a

comparable dielectric material at a given size than an equivalent microstrip system. However, the multi-step process currently used to produce the cylindrical dielectric core necessary for a D-LQH antenna is more expensive than the cost of a microstrip antenna. Costs could be reduced if the core could be first cast from a glass and then heat treated such that the desired dielectric crystalline phase was formed. $BiNbO_4$ is one such dielectric material but a Bi_2O_3 and Nb_2O_5 system will not form a glass, so oxides with stronger network forming properties must be added. B_2O_3 and silica in sufficient quantities allow the formation of a glass without liquid-liquid phase separation. While the formation of crystalline phases containing Bi and Nb under different heat treatments has been observed by XRD it is currently unclear what happens to the boron and silicon in the system as is the nature of the remaining glassy phase.[79-80].

1.3.1 The Structure of Borosilicate Glasses

Before discussing the structural units and compositional trends of borosilicate glasses it is helpful to review the structure of borate and silicate glasses and their modification by modifier ions. Just like the crystalline forms of silica, in pure SiO_2 glass the network consists solely of silicon atoms bonded to four oxygens with distributions of bond angles and no long-range order[81]. The presence of metal ions decreases the connectivity of the network as non-bridging oxygens (NBOs), which have a negative charge associated with them, appear to charge balance the positively charged metal ions. Silicon atoms in the network all remain four coordinated, but are classified by the number of other network forming next nearest neighbours they are connected to, denoted as Q^0 to Q^4. Clustering of modifier ions can occur even in otherwise apparently homogeneous glasses. This can be detected by measuring the relative quantities of Q^n species[82]. Unlike alkali or alkali earth metal ions, aluminium can play several roles in the formation of borosilicate based glasses. The Al^{3+} ions can be coordinated with either 4, 5 or 6 oxygen atoms [83]. The AlO_4 species replaces a silicate tetrahedron in the network and its negative charge removes the necessity for a NBO to charge balance a positive ion. In the five and six

coordinated sites the aluminium takes up a network modifying role and NBOs are required in the vicinity to balance charges.

The building block of the unmodified borate network is the plane trigonal BO_3 ring [84-85]. In contrast to silicate systems the connectivity of a borate glass will increase initially with the addition of a network modifier as negatively charged BO_4 groups arise within the network rather than NBOs [86]. At higher alkali concentrations however, NBOs begin to form instead of borate tetrahedra. Tetrahedral borate groups do not occur at random throughout the glass but rather form certain superstructural units [87] which are made up of a combination of BO_3 and BO_4 groups.

When glasses are formed from a mixture of B_2O_3 and SiO_2 there is a non-random distribution of boron and silicon atoms within the network. The silicon continues to form a vitreous silica-like structure and only four coordinated boron atoms will share a bridging oxygen with a silicon tetrahedron. The introduction of network modifiers has similar effects as in the binary systems containing silicon or boron. The appearance of BO_4 groups is preferred to NBO formation up to a critical modifier concentration dependent upon boron content. Beyond this NBOs in the silicon network appear. The addition of aluminium to a borosilicate system containing other modifiers will result in a reduction of 4-coordinated boron in favour of $[AlO_4]^-$ [81].

1.3.2 ^{29}Si, ^{27}Al and ^{11}B NMR of Glasses and Ceramics

Solid-state NMR has long been applied to the polycrystalline and amorphous forms of borates and silicates [88-90]. Relevant knowledge and work concerning the information that can be obtained from ^{29}Si, ^{27}Al and ^{11}B NMR of glasses is summarised below. Although the distribution of bond angles in silicate tetrahedra in glasses cause a broadening of ^{29}Si NMR lineshapes, it is still possible to distinguish between Q^n species and to quantify their intensities. Care must be taken to also consider crystalline phases when assigning spectra of materials that may be phase separated as these can also appear as distinct peaks in a spectrum. The disorder in

glasses causes a similar broadening in ^{27}Al NMR which can make quantification of the amounts of 4-, 5- and 6-coordinated aluminium difficult and quantification is further complicated as ^{27}Al is a quadrupolar nucleus, for more details see section 2.2.5. Fortunately several techniques exist to either remove the broadening or create multi-dimensional spectra allowing the separation of the different species[91-93]. At field strengths of 14 T or greater there is complete separation of BO_3 and BO_4 sites by ^{11}B NMR regardless of the degree of disorder in the system. However, 1D NMR is insufficient to distinguish between different sites within those species and again more complex techniques to remove broadening from or harness differences in quadrupolar properties of the sites are required.

Chapter 2

Chapter 2: NMR Theory

2.1 Introduction

NMR spectroscopy is capable of providing information about the structure of a material by detecting proportionally small variations in the response of nuclei to radio frequency radiation in an applied magnetic field. Nuclei with a non-zero intrinsic spin have a magnetic moment (μ) that will precess in an applied field (B_0) around the direction of B_0 (z-axis) at a rate known as the Larmor frequency (ω_0), this is given by

$$\omega_0 = \gamma |B_0|, \tag{2.1}$$

where γ is the gyromagnetic ratio, a property of the isotope being studied [94-95]. The variation of ω_0 within nuclei of the same isotope, which can be linked to the structure of a material, is a result of its dependence on the local electromagnetic conditions at each nucleus. In the case of a material on the macroscopic scale with no internal magnetic field and a large number of randomly orientated spins the application of a magnetic field results in an energy difference

$$\Delta U = -\gamma \eta m_I B_0, \tag{2.2}$$

between spin states (m_I) is created, this is called the Zeeman effect. These differences cause a thermal population difference between spin states. A net magnetisation (M) aligned in the direction of the applied field is created. If an additional magnetic field (B_1) which is weak compared to B_0 and is applied in a perpendicular direction (x-axis) then an additional torque on the nucleus' magnetic moment will result. However, due to the magnetic moment's existing precession, if B_1 is fixed in direction it will merely cause μ to nutate. The only condition in which B_1 can significantly alter the motion of μ is if it is rotating around B_0 at or close to the Larmor frequency of the spins, ω_0. This is a resonance effect and results in a torque on μ away from B_0 which over an ensemble of spins will tip M out of alignment with B_0. For this reason B_1 is an oscillating rf. field of the form:

$$\underline{B}_1 = B_1 \cos(\omega_{ref} + \phi_p)\underline{e}_x , \tag{2.3}$$

where ω_{ref} is the frequency of the pulse and φ_p is its phase, $\underline{e}_x$ is the unit vector in the x direction.

The behaviour of M after the cessation of B_1 is the source of the information on the magnetic environment of nuclei on which NMR relies. As B_0 is still being applied, the individual spins will continue to precess around it at ω_0, but now so will M. The precession of the macroscopic magnetisation can be detected by the current it will induce in nearby conductors through electromagnetic induction. This is the method by which ω_0 is measured in an NMR experiment. The precession of M around B_0 will continue only for a finite time as it is subject to relaxation which will return it to the equilibrium state that existed before the application of B_1. The relaxation of the components of M aligned with and perpendicular to B_0 are treated separately.

The relaxation of M in the plane perpendicular to the applied field is known as spin-spin relaxation which is characterised by the time T_2, known as the transverse relaxation time. As mentioned above, the perturbation of the magnetic field caused by magnetic moments in the sample results in a variation in the field experienced by the nuclei. Equation 2.1 tells us ω_0 is dependent on the magnetic field strength experienced by the nucleus so a distribution of ω will exist across the spin ensemble. If M is made up of spins with different precession rates then there will be a progressive loss of coherence which over time which will reduce the components of M perpendicular to B_0. The decay of the transverse magnetisation is described by:

$$M_x = M_0 \sin(\omega_0 t) e^{-t/T_2} \tag{2.4}$$

$$M_y = -M_0 \cos(\omega_0 t) e^{-t/T_2} \tag{2.5}$$

where M_0 is the magnitude of the transverse magnetisation at time $t = 0$ when B_1 has just ceased to be applied.

Relaxation in the direction of B_0 is known as longitudinal or spin-lattice relaxation and occurs over time T_1. It involves the relaxation of spin populations

rather than just coherences and so requires the loss of energy from the spin system to its surroundings. The spin populations return to equilibrium as the spins experience modulations in their local magnetic fields at the Larmor frequency which have a similar effect to an applied EM field. In spin ½ nuclei in the solid state these modulations are caused by variations in the direct coupling of spin dipoles, the coupling of spins through bonding electrons and anisotropy in the magnetic shielding around the nuclei. Nuclei of spin > ½ have an electric quadrupolar moment which interacts with local electric field effects and enables an additional relaxation pathway that is typically dominant. All these interactions are vital to the interpretation of solid-state NMR spectra and so are treated in more detail in Section 2.2. The growth of the longitudinal magnetisation after the application of a rf pulse that has created purely transverse magnetisation is described by:

$$M_z = M_0(1 - e^{-t/T_1}) \tag{2.6}$$

where M_0 is the magnitude of the longitudinal magnetisation at time $t = 0$ when B_1 has just ceased to be applied.

It has been mentioned above that the magnetic environment of a nucleus affects its frequency of precession and therefore the frequency detected in an NMR experiment. The largest perturbation to the local magnetic field at a nucleus is caused by chemical shielding due to surrounding electrons. Its effect on the Larmor frequency of a nucleus is known as the chemical shielding, σ, which modifies equation 2.1 to:

$$\omega_0 = \gamma|B_0|(1 - \sigma) \tag{2.7}$$

It is this chemical shielding that makes it possible to distinguish between nuclei of the same isotope in different structural (chemical) environments. From equation 2.7 we can see that in order to calculate chemical shielding both the resonant frequency and magnetic field strength must both be accurately measured. As the field strength of the superconducting magnets used in NMR varies over a time scale of

days and is not routinely measured, it is chemical shift, δ, that is measured and used a proxy for the chemical shielding. It is defined as

$$\delta = \frac{\omega_0 - \omega_{ref}}{\omega_{ref}} \tag{2.8}$$

where ω_0 is the frequency of the chemical site and ω_{ref} is the frequency of a structural site within a compound (the reference compound) with a well defined chemical shift, measured at the same field strength as ω_0. Chemical shift is measured in parts per million (ppm) of the reference frequency. From equation 2.7 it is apparent that changes in resonant frequency and chemical shielding are negatively proportional meaning that the scales of δ and σ increase in opposite directions.

2.2 Interactions

The treatment of the magnetisation of a spin ensemble given above assumed that the magnetic moments of nuclear spins did not interact with one another and that the electric charge within them was spherical. However, as mentioned in Section 2.1, spins will couple with one another and with nearby electrons through a number of interactions. Understanding these interactions is necessary to interpret spectra and to understand pulse sequences and techniques designed to reduce, eliminate or utilise them. These interactions mean that the spin Hamiltonian of a nucleus is more complex than simply the nuclear Zeeman interaction ($\hat{H} = -\gamma B_0 \hat{I}_z$), and the resonant component of the interaction with B_1 during a pulse ($\hat{H} = -\frac{1}{2}\gamma B_1 \left(\cos\{\omega_{ref} t + \phi_p\} \hat{I}_x + \sin\{\omega_{ref} t + \phi_p\} \hat{I}_y \right)$), the full spin Hamiltonian is given by:

$$\hat{H}_{full} = \hat{H}_{static} + \hat{H}_{rf} + \hat{H}_J + \hat{H}_{CS} + \hat{H}_{DD} + \hat{H}_Q + \hat{H}_{KS}, \tag{2.9}$$

where the J, CS, DD, Q and KS terms are the contributions from spin-spin coupling (or J-coupling), chemical shift, dipole-dipole coupling, quadrupole coupling and the Knight shift respectively, all of which are discussed below.

2.2.1 Dipole-Dipole Coupling

It is a basic tenet of magnetism that magnetic moments will interact with one another, and those caused by the spins of nuclei are no different. The most direct way the spins will influence one another will be their interaction with the magnetic fields caused by neighbouring spins. This is a through space interaction, dependent upon the distance between spins and known as dipole-dipole coupling as the orientation of the magnetic moments are also key to the strength of the coupling. The full Hamiltonian of the dipolar coupling between two spins *j* and *k* is given by:

$$\hat{H}_{DD} = \frac{\gamma_j \gamma_k \eta^2 \mu_0}{4\pi r^3}\left(\hat{\underline{I}}_j \cdot \hat{\underline{I}}_k - 3\left(\hat{\underline{I}}_j \cdot \underline{r}\right)\left(\hat{\underline{I}}_k \cdot \underline{r}\right)\right) \qquad (2.10)$$

where *r* is the internuclear distance, $\underline{r}$ the internuclear vector and $\underline{I}_j$ and $\underline{I}_k$ the spins of the nuclei. By applying the secular approximation which holds true for the high magnetic fields found in NMR the Hamiltonian is simplified to:

$$\hat{H}_{DD} = \frac{\gamma_j \gamma_k \eta^2 \mu_0}{8\pi r^3}(3\cos^2\Theta_{jk} - 1)\left(\hat{\underline{I}}_j \cdot \hat{\underline{I}}_k - 3I_{jz}I_{kz}\right) \qquad (2.11)$$

where Θ_{jk} is the angle between the applied field and the inter-nuclear vector. In a system in which the spins are randomly oriented with respect to one another the angular dependence of the dipolar coupling strength creates a Gaussian distribution of energies and thus precession frequencies often broaden the NMR linewidth significantly more than the inhomogeny in B_0.

2.2.2 Spin-Spin Coupling

As well as direct through-space interaction between nuclear spins an indirect mode of coupling must be considered. If two I = ½ nuclei are connected to one another via a pair of electrons in a chemical bond then the spin states of the electrons will further split the nuclear spin energy states through the electron-nucleus hyperfine interaction. The spins of the electrons in the bond must be anti-parallel according to the exclusion principle, but the nuclear spins may be parallel or anti-parallel with

respect to one another. When the nuclear spins are anti-parallel the electron spins can be oriented in a manner which minimises the hyperfine interaction energy. However, if the nuclear spins are parallel, either nuclear spin state will result in one of the electrons being in the high energy state. The Hamiltonian of the isotropic component of the spin-spin coupling between two spins *j* and *k* is given by:

$$\hat{H}_J^{iso} = 2\pi J_{jk} \hat{\underline{I}}_j \cdot \hat{\underline{I}}_k \tag{2.12}$$

where J_{jk} is the isotropic scalar coupling. While there is also an anisotropic component in the solid-state it is difficult to distinguish from the dipolar coupling which it is usually dwarfed by.

In systems with more than two spins connected by chemical bonds, the energy splitting becomes more complex. In a three spin system in which spin *j* is bonded to spins *k* and *l*, but *k* and *l* are not bonded to one another, the eight possible nuclear spin states can be sorted into four cases. When all three spins are parallel the hyperfine interaction cannot be minimised in either bond and spin *j* is in a high energy state. Conversely, if both *k* and *l* are anti-parallel with respect to *j* then the electrons can flip spin states to lower the hyperfine energy. Two other states exist in which one of *k* or *l* is parallel with *j*, but the other is anti-parallel. This spin state of the system is at an energy intermediate between the two previous states and will be twice as populated as them. This spin-spin coupling manifests itself in NMR spectroscopy by dividing peaks into multiplets. In the two spin system outlined above a doublet made up of two peaks of equal intensity separated by the coupling strength *J*. While the three spin system results in a triplet of peaks with intensity ratios 1:2:1, separated by the coupling constants J_{jk} and J_{jl}.

2.2.3 Chemical Shift Anisotropy

In Section 2.1 the chemical shielding was introduced as the change in the frequency of the precession of the nucleus due to the perturbation of the magnetic field at the nucleus by the presence of local electrons. If the electron density around a particular structural site is not spherically symmetrical then this shielding will vary according to the orientation of B_0. In a powdered sample the orientation of B_0 with respect to the local magnetic environment will be randomly distributed over the many

spins in the sample, so the shielding and thus the chemical shift must be considered as a tensor quality. In an axially symmetric system the chemical shift anisotropy (CSA) is characterised with respect to principal axes parallel and perpendicular to the plane of symmetry. In lower symmetry environments three unique principal axes are required. The chemical shielding constant when B_0 is aligned with each axis is denoted by $\sigma_{11,}$ σ_{22} and σ_{33}, where $\sigma_{11}<\sigma_{22}<\sigma_{33}$. Giving the general expression:

$$\sigma = \sum_{j=1}^{3} \sigma_{jj} \cos^2 \theta_j \tag{2.13}$$

where θ_j is the angle between j and B_0. For the axially symmetrical case $\sigma_{11} = \sigma_{22}$. The chemical shifts of the principal components can be easily identified from the lineshape of a powdered solid, δ_{11} is the closest to the isotropic value, δ_{33} the furthest and δ_{22} intermediate. Several other parameters used to describe the CSA in this work are defined as follows. The isotropic shift is given by the average of the three principal values while the shift anisotropy, $\delta_{aniso} = 3/2(\delta_{33} - \delta_{iso})$ and asymmetry parameter, $\eta = (\delta_{22} - \delta_{11})/(\delta_{33} - \delta_{iso})$ (where X, Y and Z are the principal axes of the shielding tensor) are also used to give a complete description of the tensor.

2.2.4 The Knight Shift

The effect of electron shielding on the Larmor frequency of nuclei in ionic and covalent bonded materials is known as the chemical shift and is dominated by the effect of the electron's orbital magnetism. However, in metallic solids the spin magnetism of the electrons is dominant and this effect is referred to as the Knight shift. It is possible for the Knight shift to be either positively or negatively shifted with respect to a chemical shift reference as s-like conduction electrons give positive shifts while d-like electrons contribute negative shifts [96]. The Knight shift range of nuclei is often much larger than the chemical shift range, this is true for platinum for example for which the chemical shift range is ~15000 ppm [97] but the Knight shift can vary over tens of thousands of ppm. Spin magnetism is significant for metals because its band structure results in a much smaller energy gap between the lowest occupied and highest unoccupied electron states. When an external magnetic field is applied to a metal those electrons which are within kT of the Fermi energy (E_f, the

energy of the highest occupied state at zero temperature) are susceptible to being excited and spin states with and against the applied field are differentiated, resulting in a population difference of excited electrons and a weak form of paramagnetism known as Pauli paramagnetism. This magnetism is the cause of the Knight shift and means that the magnetic properties and energy levels in a metallic sample can be probed by NMR. From the reasoning above it follows that the number of states close to E_f effects the strength of the Pauli paramagnetism and the resulting Knight shift. It is the density of the energy states over a given energy interval which is of significance and this is known as the density of states (DOS).

In metallic particles sufficiently small so that surface boundary effects cannot be ignored the DOS at the Fermi energy will vary across the particle depending on the distance to the surface. This parameter, the local density of states LDOS, is linked to the size of the Knight shift as the difference between the integral of LDOS between E_f – kT and E_f between the spin up and spin down states is a measure of the local magnetism [95]. At a point at the surface of a metallic particle there will be fewer electrons within a given distance than at the centre of a particle. This is turn means fewer overlapping orbitals and a lower LDOS. For this reason the surface is less magnetic than the centre of a particle and the Knight shift is correspondingly weaker. The paramagnetism and Knight shift becomes stronger as the centre of the particle is approached and may reach close to bulk values if the particle is of sufficient size.

Bucher *et al.*[63] developed a model for the interpretation of NMR spectra of metal particles small enough for surface LDOS effects to be significant. It assumes the particles are cubooctohedral and spectra are fit using a series of Gaussians each representing the contribution from a layer of the nanoparticle and proportional in intensity to the number of atoms in the layer. The number of atoms in the p^{th} layer from the centre of a cubooctohedral particle is simply:

$$N(p) = \frac{10p^3 - 15p^2 + 11p - 3}{3}. \qquad (2.14)$$

The widths of the peaks are not quantitatively predicted but must decrease monotonically as the centre of the particle is approached. The Knight shift of the n^{th} layer below the surface is given by:

$$K_n = (K_\infty - K_0)e^{-\frac{n}{m}} \tag{2.15}$$

where m is the healing length in units of layer thickness.

2.2.5 Electric Quadrupole Coupling

In discussing the perturbations in the magnetic field caused by the presence of the particles that make up the sample, the electromagnetic field created by the nucleus itself cannot be ignored. Nuclei of spin > ½ have an electric quadrupole moment, Q. This quadrupole moment interacts with electric field gradients ($eq_{xx} = d^2V/dx^2$, $eq_{yy} = d^2V/dy^2$, $eq_{zz} = d^2V/dz^2$) across the nucleus. The energy of each spin state of a nucleus is split by the Zeeman interaction so that $2I$ lines appear in the NMR spectrum. For half-integer spin nuclei the central ½ ↔ –½ spin transition is dominant and the others are usually neglected. In the high field limit quadrupolar effects can be considered a perturbation of the Zeeman interaction. The first-order perturbation does not effect the central transition and like other interactions proportional to $3\cos^2\theta - 1$ (θ here is the angle between eq_{zz} and B_0) it can be averaged by Magic Angle Spinning (see Section 2.3.5). However, the second-order effect does alter the energy of the central transition and cannot be averaged by spinning at the magic angle as this component is instead related to $4\sin^2\theta - 2\sin^4\theta$. As the energy splitting is dependent upon θ the spectrum of a non-crystalline solid results in a powder pattern. For any particular quadrupolar nucleus in a certain structural environment the powder lineshape pattern can be fit using only two quadrupolar parameters, χ_Q and η, where χ_Q is the quadrupolar coupling constant and is equal to

$$\chi_Q = \frac{e^2Qq_{zz}}{h}, \tag{2.16}$$

and η is the asymmetry parameter

$$\eta = (q_{xx} - q_{yy}) / q_{zz}, \tag{2.17}$$

2.3 The NMR Experiment

2.3.1 The Superconducting Magnet

The sensitivity of an NMR experiment is dependent upon the size of the magnetisation of the bulk sample. This is proportional to the population difference at equilibrium, Δn_0, between the spin states aligned and opposed to the applied field, which is given by:

$$\Delta n_0 = N(\frac{\Delta U}{2kT}) \tag{2.18}$$

where N is the number of nuclei in the sample. So the NMR signal can be maximised by reducing T or increasing ΔU. Equation 2.2 shows us that ΔU scales with B_0 so the majority of modern NMR utilises a superconducting solenoid magnet which offers the high field strength required combined with stability of only a few Hz over a time scale of several days. The solenoid is designed to create a highly homogeneous volume of field at its centre which is only a few cubic centimetres. This point is accessed by a hollow bore in the magnet that extends the length of solenoid's axis. The probe containing the sample is inserted into this bore.

2.3.2 The Probe and Coil

In order to generate B_1 a second coil around the sample is required, which is located inside the probe. This solenoid coil is made from a room temperature conductor, usually silver, and is scaled to fit closely around the sample holder. The coil acts as a transmitter of the rf B_1 field, as well as a receiver in which a current is induced by the evolving magnetisation of the nuclei in the sample. The signal created by induced currents in the coil is called the free induction decay (FID) as the signal decays according to the relaxation of the magnetisation as described in Section 2.1 The probe contains RC circuitry which allows the frequency response of the electronics to be manually tuned to the frequency of the type of nucleus under

investigation. Most modern probes have between two and four separate electrical channels which are designed for different frequency ranges. As well as greater experimental flexibility this allows probes to be used for multiple channel experiments which observe or manipulate the magnetisation of multiple nuclear isotopes simultaneously.

2.3.3 The Spectrometer

The NMR experiment begins and ends with a spectrometer capable of generating and gating the radiofrequency pulses sent to the probe and digitising the signal generated by the current induced in the coil. A low power rf signal with a well defined frequency is generated by the radiofrequency synthesizer. The signal then passes through a phase shifter which is capable of rapidly changing the phase of the oscillating signal as required by the pulse program as defined by the user. It is necessary to cycle the phases of pulses in a sequence between four values $\pi/2$ apart, in multiple pulse sequences it is common for the complete cycle to include each possible combination of phases across the sequence. Phase cycling is important for many NMR experiments as it eliminates any component of the signal which is due to imperfections and resulting biases in the spectrometer hardware. After any necessary shifting the radio frequency is gated into discrete pulses as determined by pulse programming. Before entering the probe the signal is amplified to the power levels required to excite the spins. A duplexer switches between allowing power from the amplifier to the probe and allowing flow between the probe and receiver. The NMR signal detected by the coil is many orders of magnitude weaker than the transmitted pulses so first must be boosted in strength by a preamplifier. As analogue to digital conversion is much easier at lower frequencies the signal is first converted from an absolute frequency in the MHz range to a frequency relative to the transmission frequency of the order of tens of kHz. As mentioned in Section 2.1 B_1 can only resonate with spins with Larmor frequencies close to its own frequency. The method by which the transmitted and detected frequencies are compared can only determine the magnitude of the difference in frequencies and not its sign.

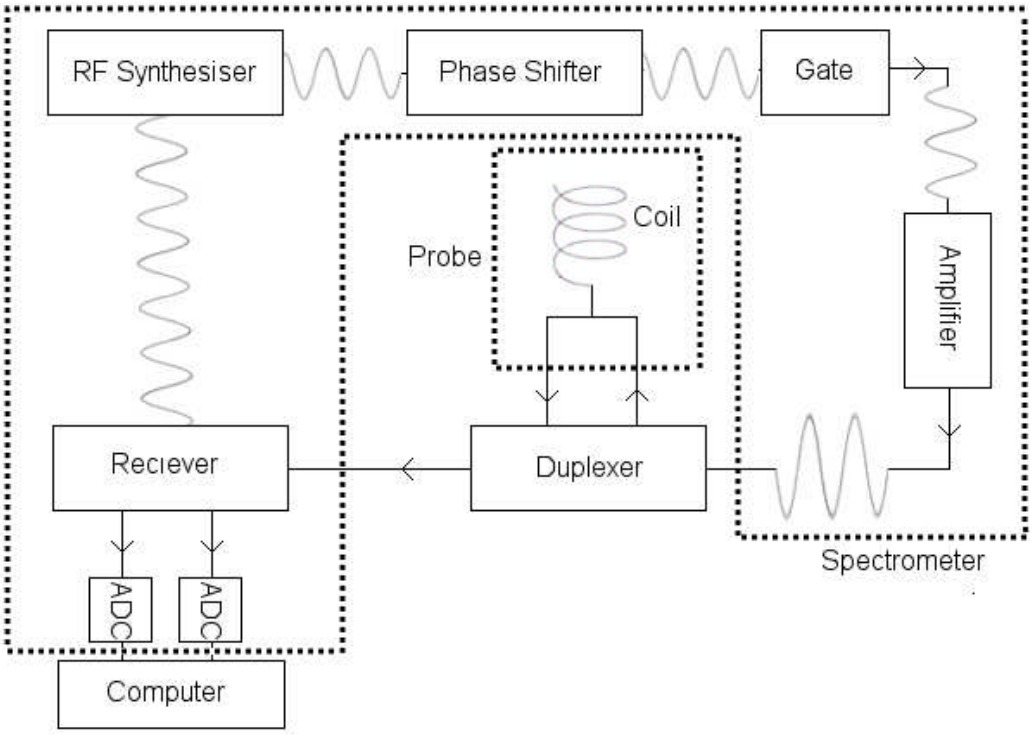

Figure 2.1: A schematic of the NMR experiment showing key equipment.

This is resolved by splitting the detected signal into two equal parts and phase shifting one by $\pi/2$ by making it travel an effective half wavelength further before recombination. The twin signals are known as the real and imaginary components of the signal. By comparison of the reference, real and imaginary signals the sign of the relative frequencies present in the received signals can be determined. The signals are then turned into digital information by an analogue to digital converter to enable processing and analysis through computer software.

2.3.4 Magic Angle Spinning

In Section 2.2 several interactions sensitive to the anisotropy of the local environments were introduced. They introduce a broadening distribution of precession frequencies of nuclei with different orientations with respect to the applied field B_0 even if they are in identical chemical environments. This can be useful as it can provide extractable information on the orientation of the electronic environment of the nucleus. However, it is commonplace that it is desirable to remove this broadening either to enhance signal to noise or to improve resolution for the sake of distinguishing between nuclei in different chemical or magnetic environments. Magic

angle spinning (MAS) is the technique that achieves the removal or reduction of broadening caused by chemical shift anisotropy, dipolar coupling or 1st order quadrupolar coupling, all of which contain terms of $(3\cos^2\theta - 1)$. A value of θ = 54.74° (the magic angle) reduces this expression, and thus the scale of the interaction, to zero. However, the nuclear spins are randomly oriented in the material and so no single sample alignment will achieve this condition for all spins. The solution is to physically spin the whole sample with an axis of rotation tilted 54.74° from the direction of B_0. This ensures that over the course of a rotation the average angle between the spin of the nucleus and B_0 is the magic angle, as the angular component perpendicular to the axis of physical rotation is averaged to zero.

In order to completely remove the broadening from the spectrum the MAS speed must be much faster than the time scale of the interaction in question. If this is not the case then MAS causes the appearance of spinning side bands as well as a narrowing of the lineshape. Sidebands appear at points that are integer multiples of the spinning frequency away from the central isotropic resonance in both directions. The amplitudes of the sidebands can be used to determine the interaction, this is useful in cases in which signal would be too weak to record a static experiment.

2.4 NMR Techniques

In this section the various techniques and pulse sequences used in experiments in Chapters 4-7 will be introduced and explained to a level that is necessary for the interpretation of the results presented in those chapters.

2.4.1 One pulse

The simplest of NMR pulse sequences, the one pulse experiment consists of single rf pulse followed by a period of acquisition. Most commonly the power and length of the pulse is optimised so as to tip the magnetisation of the spins at an angle of 90° to B_0 to ensure maximum initial signal. Sometimes the tip-angle of the pulse will be reduced so that less time between pulses is required to allow full relaxation. The relative intensities of resonances in one pulse experiments are considered quantitative if the time between pulses is at least 3-5 times the longest T_1 of the

environments. While the evolution of the FID begins instantaneously from the end of the excitation pulse, the detection of the FID cannot as the receiver coil will suffer from dead time acoustic ringing for a period after the pulse, corrupting any data acquired simultaneously. The importance of this data loss depends on the length of this period determined by various properties of the probe system and the length of the FID.

2.4.2 Spin Echo

The spin echo experiment [98] utilises the effect first observed by Hahn that the transverse magnetisation of nuclear spins lost to dephasing can be refocused as spin echoes by the application of certain rf pulses after the initial pulse. The simplest experiment exploiting this effect begins by applying a pulse which creates transverse magnetisation in the plane *xy*, perpendicular to the direction of B_0 defining *z*. The magnetisation is then left to evolve for a time, *t*, before a second pulse is applied which flips the magnetisation 180º around the axis *y*, orthogonal with both B_0 and the axis of rotation caused by the first pulse. As the local magnetic field strength and thus ω_0 varies across the spin population the spins will have precessed around *z* at different rates during *t* causing a spread in the components of the spins perpendicular to *z*, as described in Section 2.1. The effect of the second 180º pulse is to reverse the spread of spins in the direction of their rotation so that the fastest evolving spins are now behind the slower spins. This creates the condition that after an additional time t after the beginning of the 180º pulse the spins have been refocused in the *xy* plane. The effect observed in the FID of the experiment is a rebuilding of the decayed signal after the 2nd pulse which peaks at time *2t* after the end of the first pulse. The intensity of the echo signal decays once more as dictated by spin-spin relaxation. The peak signal intensities of the echo will not be same as that observed immediately after the excitation pulse due to the transverse relaxation that has occurred during *2t*. As discussed in section 2.1 transverse relaxation is characterised by the time T_2, however the loss of coherence actually occurs according to T_2^*, the effective transverse relaxation time. This includes the effect of an inhomogeneous applied field and can result in much shorter measured relaxation timescales in practice.

While manipulation of spin echoes has been harnessed in many complex experiments [99-100] the simple spin-echo itself is useful for experiments which require a delay between pulse and acquisition that makes up a significant portion of the FID. The spin echo can be observed independent of any ringing or dead time due to the delay of *t* between pulse and peak signal. Additionally in the case that the loss of peak signal due to relaxation before refocusing is less than a factor of 2 then signal to noise can be increased by the collection of both the build up and decay of the echo. In addition to the considerations required for single pulse experiments the differential spin-spin relaxation rates of peaks in spin-echo experiments must be accounted for if relative intensities are to be considered quantitative.

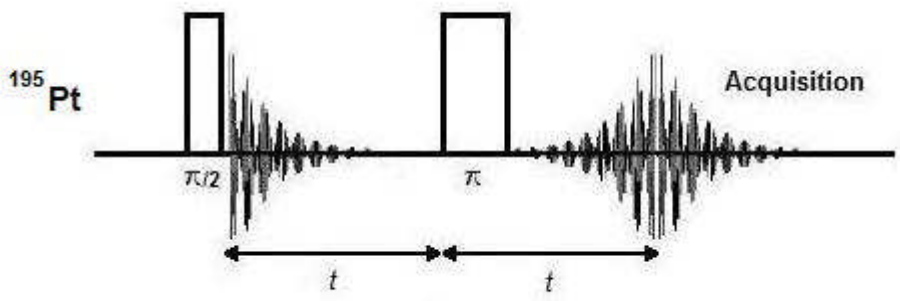

Figure 2.2: Example of a spin echo pulse sequence.

2.4.3 Wideline NMR Tchniques

The width of frequencies that can be excited in an NMR experiment is limited by a number of factors including the resonant condition between the transmission frequency of B_1 and ω_0 (discussed in Section 2.1), the finite width of the excitation pulse and the ability of the probe to detect frequencies far from ω_{ref}. The frequency excitation profile of a pulse is given by the Fourier transform of its temporal profile. Most rf pulses used in NMR are top hat functions, the Fourier transform of which is a Sinc function, its width inversely proportional the width of the pulse. The lower limit of the pulse width is constrained by the maximum power that can be safely withstood by the probe. The RC properties of the probe are configured such that only a finite width of frequencies can be transmitted or received. If the spectrum of a nucleus is

broader than can be excited and detected without intolerable losses in quantification across the spectrum then wideline acquisition techniques must be used.

2.4.3.1 Frequency Stepped NMR

There are several methods of recreating a lineshape wider than single frequency Fourier transform NMR is capable of by the combination of multiple acquisitions at different frequencies. The most basic approach is to plot the maximum FID intensity or integrated area of the FID against the frequency of each acquisition in order to create a point-by-point spectrum. These techniques are known as Spin Echo Height Spectroscopy (SEHS) and Spin Echo Integration Spectroscopy (SEIS) respectively [101]. They are unable to resolve spectral features lower than the sampling resolution on the frequency axis and SEHS will not reproduce a lineshape faithfully if the acquired spectrum contains components with different relaxation times as it will under represent the intensity from slow relaxing nuclei. The advantage of point-by-point spectra is that the sampling resolution is not prescribed as for summed FT techniques and therefore fewer acquisitions can be made and the full spectrum reproduced in a shorter timescale. The plotted spectrum will be most accurate if only spins with Larmor frequencies close to ω_{ref} contribute to the signal. A narrow excitation profile is achieved through the use of very long pulse time (i.e. the use of so called soft pulses).

The alternative to point-by-point techniques is to acquire at multiple frequencies and to sum the FT spectra to more faithfully recreate the lineshape. However, in order to avoid significant distortions to the lineshape (distortions are less than 4% of the signal strength) due to insufficiently frequent sampling the acquisitions must be no further apart than 0.75 times the full width at half height of the signal acquired at each frequency [101]. So it is advantageous to maximise the excitation width and thus minimise the pulse lengths so that fewer acquisitions are required over a given frequency range. While summed FT frequency stepping NMR does not suffer from the resolution issues of the point-by-point technique it shares a common weakness in the variability of signal detection strength that the probe can achieve across a frequency range. Unless carefully monitored and accounted for this will add an unknown error in the intensities of different regions of the recreated spectrum.

2.4.3.2 Field Sweep NMR

While field sweep NMR could be utilised to produce spectra by any of three processing methods outlined above, for frequency stepping NMR only the summed FT approach will be considered as it is the only one which harnesses all the advantages of the technique. While the processing of the spectra at multiple frequencies is unchanged the manner in which they are acquired is radically different. The probe is tuned at a single frequency throughout all acquisitions but the applied field, B_0, is varied between acquisitions. This has the effect of exciting a different set of spins in each acquisition. Equation 2.20 calculates $\omega_{0\alpha}$ the Larmor frequency at the initial field, $B_{0\alpha}$, for spins for which $\omega_{0\beta} = \omega_{ref}$ at the swept field strength, $B_{0\beta}$.

$$\omega_{0\beta} = \omega_{0\alpha} \frac{B_{0\beta}}{B_{0\alpha}} \tag{2.20}$$

By converting the different field steps into frequencies in the initial field the spectra can be referenced with respect to one another and summed as before. As well as retaining all the benefits of summed FT frequency stepped NMR, field sweeping eliminates the errors and labour associated with retuning of the probe between acquisitions.

2.4.4 MQMAS

Section 2.2.5 outlined the manner in which the quadrupolar nature of nuclei can be used to distinguish between chemically different sites by comparing electric field gradients at the nucleus and thus the symmetry of the electrical charges close to it. However, 2nd order quadrupolar effects can broaden the central transition lineshapes so that chemical differences between different structural sites cannot be resolved. While dynamic (DAS) and double (DOR) angle spinning techniques can be used to eliminate higher order effects by spinning at multiple frequencies, sequentionally or simultaneously, during evolution times these methods are technically demanding and have remained uncommon as they require highly specialised equipment. It has also been observed that multiple quantum (MQ) excitation of nuclei can refocus higher order effects and therefore produce higher resolution spectra which distinguish chemical differences by identification of separate

isotropic quadrupolar shifts in a 2D spectrum [102-103]. Multiple quantum experiments work by averaging higher-order quadrupolar terms through the use of two spin state transitions and a single spinning frequency, rather than two frequencies and a single transition. Therefore an MQMAS experiment consists of an initial excitation of one transition, a period of evolution of the MQ transition, followed by a second excitation of a different transition, a second evolution time and finally the acquisition of a referenced signal. The two evolution times are related in length and can be varied in tandem. A 2D FT of the data leads to a spectrum with inequivalent sites appearing as spectral ridges parallel to one another. The spectrum can then be sheared to make one axis the isotropic shift axis.

2.4.5 Cross Polarisation

The relative sensitivities of NMR active nuclei vary greatly across the Periodic Table. Low abundance nuclei like ^{13}C can have sensitivities many orders of magnitude lower than protons. It is often impractical to try the same simple experiments with low sensitivity nuclei due to the time scales necessary to achieve sufficient signal to noise. In the case where low sensitivity nuclei are in proximity to high sensitivity nuclei in a material it is possible to transfer the magnetisation from high to low sensitivity nuclei using a technique called Cross Polarisation (CP). This transfer is mediated by means of the heteronuclear dipolar coupling. The most common application is to organic systems with carbon atoms close to at least one hydrogen atom, but many other combinations of elements are used as long as there is a significant difference in gyromagnetic ratio and thus sensitivity between the nuclei. The experiment begins with the excitation of the high sensitivity donor nuclei (S) by a $\pi/2$ pulse immediately followed by a period known as the contact time. During this interval, that is typically on the order of milliseconds, continuous rf is supplied to the channels of both donor and receptor nuclei. Magnetisation is transferred between the nuclei during the contact time when the Hartmann-Hahn matching condition is met. This condition states the product of the applied field strength and the gyromagnetic ratio for the donor and receptor nuclei (I) must be equal, e.g.:

$$\gamma_I B_{1,I} = \gamma_S B_{1,S} \tag{2.21}$$

Where $B_{1,I}$ and $B_{1,S}$ are the rf fields applied to the nuclei during the contact time. As discussed in Section 2.3.4 it is often necessary to reduce or eliminate dipolar couplings in solid samples by means of MAS to achieve spectral resolution. However, it is the dipolar coupling by which magnetisation is transferred and this has the effect of splitting the matching condition into peaks corresponding to the spinning speed which in turn makes experimental set up more difficult, especially in the case of low sensitivity nuclei. To counteract this effect, new CP techniques were developed to remove the necessity to locate the exact matching condition by varying the rf power on one of the channels during the contact time[104]. Of these, RAMP-CP was chosen for ^{19}F-^{13}C experiments to be undertaken in this work. While the donor rf power is kept constant during the contact time the carbon power is increased linearly in identical discrete steps to create a 'ramp' power profile with time. As long as the total range of carbon power is large enough and the incremental steps are sufficiently small it is possible to find a condition in which the CP signal strength is invariant with respect to the starting and final rf. power of the ramp. This makes experimental set up a great deal easier and less sensitive to experimental variations that can occur over the relatively long experiments necessary to record ^{13}C spectra even with the aid of magnetisation transfer.

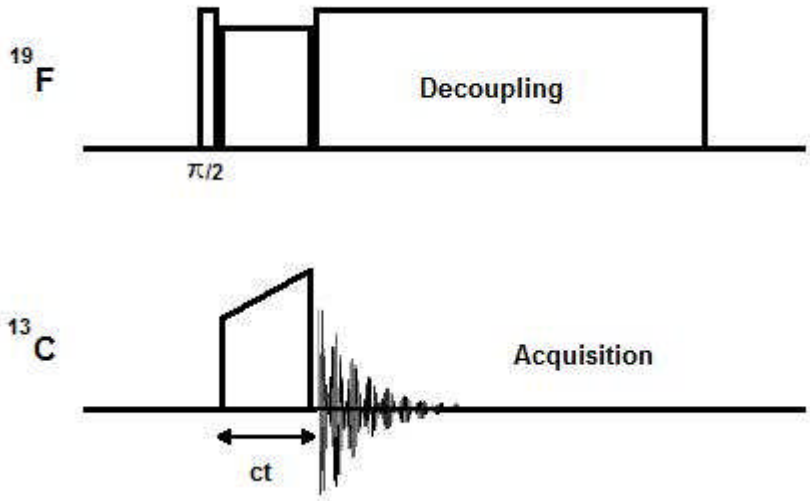

Figure 2.3: Example of a RAMP CP pulse sequence.

2.4.6 Decoupling

While the observation and measurement of spin coupling can be a useful probe of material structure it is often desirable to remove such effects from solid-state

experiments as they broaden resonances and reduce spectral resolution. In Section 2.3.4 MAS was discussed as a way of narrowing resonances that are broadened due to spin interactions, however the rate at which the sample can be spun is limited by mechanical considerations and is not always sufficient to completely remove such broadening. In certain circumstances decoupling is useful instead or as a complement to MAS. It involves the continuing irradiation of spins during acquisition to suppress interactions and is most commonly used to remove heteronuclear coupling. In this case the spins of the nuclei coupled to those which are being observed are irradiated on one channel while acquisition occurs on another. The effect of decoupling is to cause the magnetic moment of the interacting spins to precess at the same rate regardless of the spin state they are in, eliminating signal splitting and therefore broadening over an ensemble.

While decoupling must continue throughout acquisition it need not consist of continuous rf. on the decoupling channel. Several different pulsed decoupling sequences have been developed including [105-106]. In this work two different sequences have been utilised. Continuous wave decoupling for ^{1}H-^{31}P CP NMR and a rotor synchronised pulsed sequence for ^{19}F-^{13}C CP [107]. Continuous wave decoupling must be limited to around 40 ms after each acquisition as the continuous transmission of rf puts stress on the probe which can lead to permanent damage. Pulsed sequences allow for longer periods of decoupling as the coil is only active for a small proportion of the time.

Chapter 3

Chapter 3: Experimental

This chapter of experimental details is divided into sections according to which chapter the experimental results are presented in.

3.1 Proton Exchange Ionomers

3.1.1 Sample Preparation

Two types of ionomer samples were received from the Johnson Matthey Technology Centre (JMTC). The first series were uniform sheets of ionomer supplied to JM as commercial or experimental products by their original producers. Ionomers from the Solvay, Aciplex and Nafion brands [22] were included. JM also supplied fragmented membranes cast from solutions of Nafion ionomers with equivalent weights of 1000 and 1100. These membranes were produced by dissolving the ionomer in water or propanol and then casting them in either standard laboratory conditions or whilst heated under an infrared lamp at 140°C for 5 seconds, which was sufficient to remove all surface water from the membrane. In addition to these 100% ionomer preparations, JM also supplied dried material from experimental catalyst inks suitable for printing into electrodes. These consist of platinum nanoparticles supported on carbon and coated with Nafion. The ink solutions were either organic or aqueous based and mixed such that the carbons in the ionomer to carbons in the catalyst support were in the ratio of either 0.8 or 1.2 (carbon ratio 0.8 or 1.2). The collection of samples received is summarised below. The equivalent weights (EW) of the ionomers in Table 3.1 are values given by their manufacturers and defined as the molecular mass of a repeat unit which includes one side chain (and the associated length of backbone) and thus one sulphonic acid group. The structures of the ionomers are shown in figure 3.1.

Ionomer	Equivalent Weight	Solvent	Drying Temperature / °C	Carbon Ratio
Nafion	1000	Aqueous	20	N/A
Nafion	1000	Aqueous	140	N/A
Nafion	1100	Propanol	20	N/A
Nafion	1100	Propanol	140	N/A
Nafion	1000	Aqueous	N/A	0.8
Nafion	1000	Aqueous	N/A	1.2
Nafion	1100	Propanol	N/A	0.8
Nafion	1100	Propanol	N/A	1.2
Nafion	920	N/A	N/A	N/A
Solvay	820	N/A	N/A	N/A
Solvay	750	N/A	N/A	N/A
Nafion	1100	N/A	N/A	N/A
Aciplex	1000	N/A	N/A	N/A

Table 3.1: Summary of ionomer containing samples received from JMTC

(a)

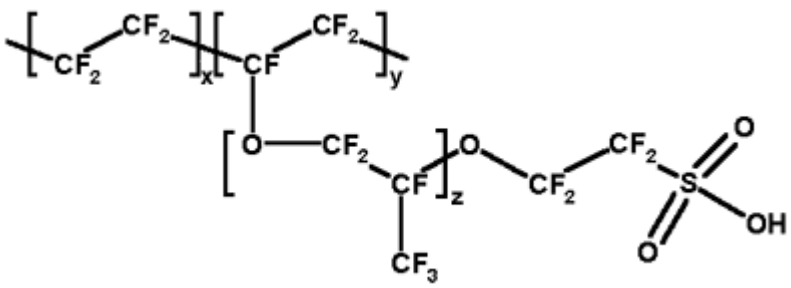

(b)

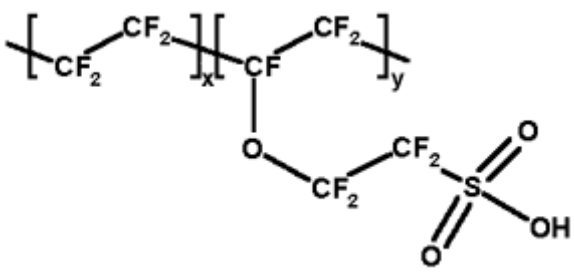

(c)

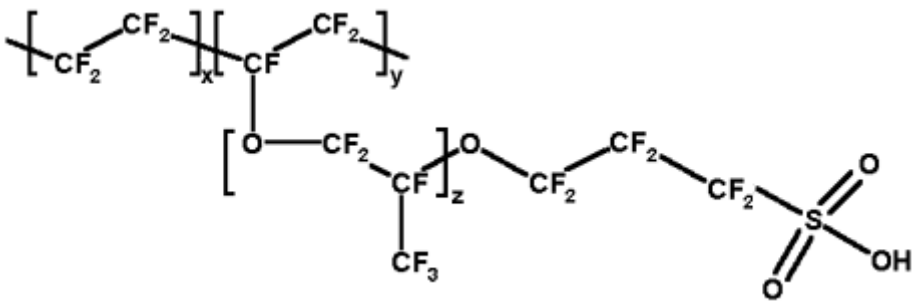

Figure 3.1: The chemical structures of (a) Nafion, (b) Solvay and (c) Aciplex ionomers.

The preparation of fluorocarbon ionomers for magic angle spinning (MAS) solid-state NMR presents an atypical combination of challenges. It is a requirement of MAS that samples be packed tightly and uniformly within the rotor to ensure stable spinning at high speeds. This is commonly achieved by grinding a solid sample to a fine powder, but this is not possible with fluorocarbon ionomers even when the sample is frozen by liquid nitrogen. Samples were delivered as either uniform sheets with a typical thickness of 50 μm or as membrane or dried ink fragments. The samples that arrived as uniform ionomer sheets could be cut and rolled so as to fit into rotors. This preparation allows for stable spinning but only a small quantity (<5 mg) of ionomer is then contained within the rotor.

The ionomer fragments could be powdered between two metal files and subsequently packed into a rotor in a way similar to a standard powder. However, when prepared in such a manner the grated ionomer reforms into a continuous solid, and the common assumption of a low contact volume between sample grains does not hold. Therefore pressure effects on the sample cannot necessarily be ignored. Additionally, the long-range order and plastic nature of the ionomer solids leave open the possibility of the stress of grating resulting in a change in the disorder of the ionomer chains. Section 4.5 addresses these concerns experimentally. This tight

packing method allowed stable high speed MAS and a sample mass of 20 mg in a 2.5 mm Bruker rotor.

The dried ink samples were supplied in the form of grains too large to fit inside a MAS rotor but could be readily powdered. The problems mentioned above are not thought to apply to inks as the catalyst is a loose aggregate with no long-range order and microscopy suggests the ionomer component of the ink does not constitute a continuous phase [39].

As discussed earlier in 1.1.2, these materials will readily exchange water with their environment. Initial studies discovered that ambient humidity changes in the laboratory resulted in variations in water content that had sufficient structural implications to noticeably alter the NMR spectra. Water content was controlled by storing samples in sealed, controlled conditions at 100% RH and 0% RH at standard temperature and pressure to equilibrate for at least 48 hours before rapid transfer to a Bruker MAS rotor which can be considered air tight over the time scale of these experiments. When materials were stored at 0% RH transfer to a rotor took place under nitrogen.

3.1.2 ^{19}F, ^{19}F-^{13}C and ^{1}H NMR

Two spectrometer systems were used for solid-state NMR studies of ionomers. A 7.05 T Oxford Spectrospin magnet with a Varian/Chemagnetics Infinity Plus 300 console and an 11.7 T Bruker Ultrashield magnet with Bruker Advance III 500 console. Both magnets have a 89 mm wide room temperature bore. ^{1}H NMR was conducted at 500 MHz, ^{19}F-^{13}C NMR at 300 MHz and ^{19}F at both fields. Bruker MAS II spin controllers were used to keep MAS speeds within ± 5 Hz for the course of all experiments. Variable temperature experiments were controlled using a Bruker BVT 3000 variable temperature control unit and a Bruker BCU 20 cooling unit integrated with the Bruker Topsin spectrometer software.

3.1.2.1 ^{1}H NMR

A Bruker 2.5 mm dual channel H/FX MAS probe was tuned to 500 MHz for ^{1}H detection. Standard 2.5 mm Bruker rotors with Vespel caps were used in all

experiments. Single pulse experiments consisted of a 2.5 μs π/2 pulse every 3 seconds with 16384 points 5 μs apart. The acquisition delay was 5 μs. The lowest frequency peak (CH_3 at 1.1 ppm) of alanine spun at 28 kHz was used to reference all spectra.

3.1.2.2 ^{19}F NMR

A π/2-τ-π-τ Hahn echo sequence was used for ^{19}F experiments at 300 MHz in order to solve baseline and phasing issues. A low fluorine background Bruker 2.5 mm dual channel HFX MAS probe tuned to 282.37 MHz was used to pulse every 3 seconds with 90° and 180° pulse lengths of 2 and 4 μs respectively, the delay between initial and refocusing pulses was 33.33 μs. Each acquisition began 23.3 μs after the pulse, was 10.24 ms long with 8192 points. At higher field, the greater resolution allowed unambiguous manual baseline correction and so echo experiments were unnecessary. A Bruker 2.5 mm dual channel H/FX MAS probe was tuned to 470.5 MHz using 2.5 μs π/2 pulses, sent with a pulse delay of 10 seconds. Each acquisition consisted of 16384 points, 2.5 μs apart and beginning after 5 μs. All spectra at both fields were referenced to the peak of PTFE at –123.2 ppm.

3.1.2.3 ^{13}C NMR

The H/F channel of Bruker 2.5 mm dual channel H/FX MAS probe was tuned to 282.37 MHz for ^{19}F magnetisation transfer and decoupling while the X channel was tuned to 75.4 MHz for ^{13}C detection. As high speed MAS is required to achieve excitation of a sufficient proportion of ^{19}F nuclei at a single frequency[46], a ramped CP sequence was used. A 2.5 μs π/2 pulse on the ^{19}F channel preceded a CP RAMP which consisted of 100 steps, 15μs long, to step through the power range of 80 kHz to 100 kHz pulses. The contact time of 1.5 ms was chosen as it optimised signal intensity for ^{13}C acquisition. A 3 second pulse delay was necessary to allow the ^{19}F nuclei to relax. Acquisition was 102.4 ms long with 2048 points, and was accompanied by a rotor synchronized decoupling regime of one 5 μs 180° ^{19}F pulse every rotor period. ^{19}F-^{13}C CP NMR was optimised by and referenced to PTFE at 111.3 ppm for ^{13}C.

3.2 Fuel Cell Catalysts

3.2.1 Sample Preparation

Catalyst samples were prepared by JMTC [14]. The received sample series are summarised in Table 3.2 below.

Table 3.2: Summary of Catalyst Samples Received from JMTC			
Metal(s)	Support	% Metal by Weight	Particle Size / nm
Pt	None	100	5
Pt	Carbon	40	<2
Pt	Carbon	40	4.7
Pt	Carbon	40	7.7
Pt	Carbon	40	15.6
Pt	Carbon	60	1.8
Pt	Carbon	60	5

Table 3.2: Summary of catalyst samples received from JMTC

Crystallite sizes are averages calculated from XRD line broadening using the Scherrer equation[108]. As the samples contain metallic particles it is important to calculate whether the pulsed rf field necessary to excite and detect nuclei in NMR will be able to penetrate through the conductive material to the centre of the particles. The skin depth equation gives the distance into a conductor after which the current induced by an applied electromagnetic field is reduced to 1/e of its initial value. It is given by:

$$\partial_s = \sqrt{\frac{2}{\omega\sigma\mu}}, \qquad [3.1]$$

where σ is the conductivity of the conductor and μ is the permeability of the conductor. For platinum with a resistivity of 105×10^{-9} Ωm and a permeability of

1.26×10^{-6} Hm^{-1} the skin depth is 20.85 μm at 62.2 MHz, the resonant frequency of bulk platinum metal. The skin depth is important because it is an indication of the distance scale on which the dielectric effect of the currents induced in a conductor will significantly reduce the effective pulsed rf field strength in a conductive sample. Although the skin depth appears much larger than the size of the particles shown in table 3.2 it is worth calculating the exact power loss at the centre of a spherical conductor which can be calculated from equations 12, 16, 19 and 20 given in [109] as (approximated to the 2nd term):

$$B_z = B_1\sqrt{\left[1-\frac{\mu_0^2\sigma^2\omega^2r^4}{105}\right]}\left[1-\frac{\mu_0^2\sigma^2\omega^2r^4}{1260}\right], \qquad [3.2]$$

where r is the radius of the particle and μ_0 is the permeability of free space. The field is entirely in the z-direction. For a material like platinum for which $\mu \approx \mu_0$ equation 3.2 can be simplified to:

$$B_z = B_1\sqrt{\left[1-\frac{4a^4}{105}\right]}\left[1-\frac{4a^4}{1260}\right], \qquad [3.3]$$

where a is the radius of particle in multiple of the skin depth. In the case of platinum at 62.2 MHz at the centre of a particle with radius equal to the skin depth the effective B_1 is 0.976 times the field strength at the surface of the particle. However, B_1 at the centre of a particle with radius $2\delta_s$ is 0.56 times the surface value. The skin depth is therefore an important indication of whether the NMR signal from the centre of a conducting particle will be comparable to the contribution from the surface.

3.2.2 ^{195}Pt Field Sweep NMR

^{195}Pt field sweep solid-state NMR was performed on a customised Magnex 7.05 T magnet with a Chemagnetics Infinity 300 spectrometer. The magnet was equipped with a secondary superconducting coil capable of sweeping the field ± 0.5 T. The current to the secondary coil was controlled by the spectrometer through a Lakeshore magnet power supply. A Bruker Z33 v HP static probe with a 10 mm coil head was tuned for ^{195}Pt detection. Approximately 20 mg of catalyst was loaded into a

9.5 mm PTFE sample holder. In order to isolate the very rapidly decaying FID signal from probe ringing and dead time a π/2-τ-π-τ Hahn echo sequence was used. The length of the π/2 pulse was 5 μs and τ was 10 μs. Each acquisition began 4 μs after the second pulse and consisted of 512 points 1 μs apart with a 40 ms recycle delay. All spectra were referenced to the peak of $K_2Pt(CN)_6$ at –3833.5 ppm. The sweeps began with zero current in the secondary coil and a resultant field of 7.05 T, the bore field of the magnet. The probe was tuned to a frequency below the known position of the low frequency edge of the lineshape to be recorded. The current was then increased in equal increments each of which reduced the resultant field applied to the sample. At each increment of applied field the FID was recorded as normal for FT NMR. The maximum current required for the sweep to cover the entire lineshape is given below:

$$A_{\max} = \frac{(F_{init} - F_{end})}{F_{init}} \frac{B_0}{C} \qquad [3.4]$$

Where F_{init} and F_{end} are the initial and end frequencies below and above the known edges of the lineshape to be swept and C is the secondary coil's unique conversion factor equal to 0.0254615 TA^{-1}.

The probe was tuned to 61.9 MHz and acquisitions were made at 65 different field strengths. The field strength was increased to 14.314A in increments of 224 mA in a direction as to oppose B_0. This corresponds to a positive 50 kHz frequency step which is below the maximum prescribed in equation 2.15. The total sweep range is 3.2 MHz. An overview of how the acquisitions are combined is given in section 2.4.3.

3.2.3 ^{195}Pt Frequency Stepped NMR

Static field experiments were conducted by disabling the sweep coils of the magnet and removing the Q-spoiling resistors from a Bruker Z33 v HP 10 mm probe head. Otherwise the hardware used was identical to that used in the field sweep experiments. The same π/2-τ-π-τ Hahn echo sequence was also used, with the length and power of the pulses being the only parameters to change. These were set to 30 μs and 60 μs to ensure a narrow excitation profile. The probe was tuned to frequencies

between 62.1 and 65 MHz which varied according to the sample being studied and its particular lineshape. Sufficient acquisitions were taken at each frequency to ensure a minimum acceptable signal-to-noise ratio in the FID. Lineshapes were constructed by recording the peak intensity of the FID of the echo at each frequency. Intensities were then normalised for the number of acquisitions recorded for that frequency. The match of the probe was not altered during the tuning for each experiment. Instead the matching loop was deformed so as to give the optimum match at 64.7 MHz for each sample. Again all spectra were referenced to $K_2Pt(CN)_6$ at –3833.5 ppm.

3.3 Glass-Ceramics

3.3.1 Sample Preparation

All glass ceramic samples were provided by Prof. Reaney's group at the University of Sheffield and consisted of a series of the cast glass BN1 and glass-ceramics formed by heat treating BN1. The glass was formed by melting a mixture of Bi_2O_3, Nb_2O_5, H_3BO_3 and SiO_2 in a covered aluminium crucible at 1250°C for 2 hours, cast into moulds and annealed at 550°C for a further hour before being allowed to cool at 1°C/min to room temperature. The reactants were combined in quantities that give a composition of 30% Bi_2O_3, 30% Nb_2O_5, 30% B_2O_3 and 10% SiO_2 by mol, however XRD reveals that up to 8% by mol of Al_2O_3 enters the glass most likely from dissolution of the crucible. The thermal history of the samples after casting varied with one sample experiencing no heat treatment and the others being treated at 600, 700, 800, 900 and 1000°C respectively for 2 hours [79]. All samples were supplied as powders sufficiently fine for packing into MAS rotors without any additional processing.

3.3.2 ^{29}Si NMR

A wide bore Oxford Spectrospin 7.05 T magnet with a Varian/Chemagnetics Infinity Plus 300 console was used in conjunction with a Varian HX 7.5 mm probe. The X channel was tuned to 59.48 MHz and samples were spun at 4.5 kHz. A single 2 μs $\pi/2$ pulse every 20 seconds was followed after 30 μs by a 3.84 ms acquisition of 256 points. All spectra were referenced to kaolinite at –92 ppm.

3.3.3 ^{27}Al NMR

^{27}Al NMR experiments were conducted on a wide bore Magnex 14.1 T magnet, Bruker Avance II^{+} console with a 3.2 mm Varian HX T3 probe tuned to 156.2 MHz and samples were spun at 15kHz. A single 0.5 μs π/12 pulse was applied with a recycle delay of 13 s. Each acquisition began 6 μs after the end of the pulse and consisted of 2048 points 5 μs apart. All spectra were reference to 1 M aluminium nitrate solution which was taken as 0 ppm.

^{27}Al MQMAS experiments at 14.1 T utilised a z-filtered [110] sequence with π/2 and 3π/2 hard pulses of 1 and 3 μs and π/2 soft pulses of 20 μs. The spectrometer acquired in States mode and the frequency was set to 156.2 MHz. Each acquisition was 17.2 ms and had 1024 points. There were 64 acquisitions across a 15 kHz spectral width in the indirect dimension. The recycle delay was again 13 s.

3.3.4 ^{11}B NMR

All ^{11}B NMR experiments were carried out on the same wide bore Magnex 14.1 T magnet and Bruker Avance II+ console. Single pulse ^{11}B experiments used a Bruker 4 mm HXY probe tuned to 192.3 MHz. The probe exhibited an ^{11}B background that was recorded and subtracted from all spectra. A single 1 μs π/18 pulse was applied with a recycle delay of 8 s. Each acquisition began 12.6 μs after the end of pulse and consisted of 2048 points 12.6 μs apart.

^{11}B MQMAS experiments utilised a z-filtered sequence with π/2 and 3π/2 hard pulses of 1.2 and 3.6 μs and π/2 soft pulses of 20 μs. The spectrometer acquired in states mode and the frequency was set to 192.313 MHz. Each acquisition was 17.2 ms and had 1024 points. There were 64 acquisitions across 15 kHz spectral width in the indirect dimension. The recycle delay was again 8 s.

3.4 Platinum(II) O,O'Dialkyldithiophosphates

3.4.1 Sample Preparation

All samples were provided by Prof. Oleg Antzutkin of the Lulea University of Technology, Sweden. Five crystalline complexes were obtained by reacting $K_2[PtCl_4]$ and salts of the form $K\{S_2P(OR)_2\}$ in aqueous solution at 60ºC overnight. The reaction products were filtered leaving yellow precipitates that were washed and left to dry. .

Sample	Formula
Ethyl	$Pt\{S_2P(O\text{-}C_2H_5)_2\}_2$
sec-Butyl	$Pt\{S_2P(O\text{-}C_4H_9)_2\}_2$
iso-Butyl	$Pt\{S_2P(O\text{-}C_4H_9)_2\}_2$
Cyclo-hexyl	$Pt\{S_2P(O\text{-}C_6H_{12})_2\}_2$
iso-Propyl	$Pt\{S_2P(O\text{-}C_3H_7)_2\}_2$

Table 3.3: Summary of Pt DTP samples received

3.4.2 ^{31}P NMR

^{31}P NMR spectra were recorded using an Oxford Spectrospin 7.05 T magnet with a CMX-300 console. ^{1}H-^{31}P cross-polarization was used in conjunction with continuous wave proton decoupling at 300.098 MHz to suppress heteronuclear dipolar interactions. Samples of the complexes (~200 mg) were packed into 4 mm zirconia rotors and loaded into a Bruker 4 mm MAS probe tuned to 121.482 MHz for ^{31}P detection. Spectra consisting of 400 acquisitions of each sample were taken at spinning frequencies of 2 and 4 kHz. The proton $\pi/2$ pulse length was 3.5 μs and the contact time 2 ms. The recycle delay was 3 s. ^{31}P chemical shifts were referenced to ammonium dihydrogen phosphate at 0.9ppm.

The ^{31}P chemical shift anisotropy, $\delta_{aniso} = 3/2(\delta_{33} - \delta_{iso})$, and the asymmetry parameter of the chemical shift tensor, $\eta = (\delta_{11} - \delta_{22})/(\delta_{33} - \delta_{iso})$, were calculated from diagrams of χ^2 statistics based on quantitative analysis of the integrated intensity

ratios of spinning sidebands in spectra recorded at two difference spinning frequencies. These calculations were performed by Prof. Antzutkin with the Mathematica program (version 4.1.2) [75].

3.4.3 ^{195}Pt NMR

^{195}Pt field sweep experiments were conducted as detailed in section 3.2.3 unless otherwise stated. Approximately 200 mg of sample was loaded into a 9.5 mm PTFE sample holder. Acquisitions began after 11 μs and were separated by a 35 s recycle delay except for the sec-Butyl sample for which the recycle delay was 4 s. The probe was tuned to 64.08 MHz and acquisitions were made at 7 different field strengths. The field strength was increased to 3.143 A in increments of 524 mA in a direction so as to oppose B_0. This corresponds to a positive 50 kHz sweep in frequency for each slice for a total of 300 kHz.

Chapter 4

4. Proton Exchange Ionomers

4.1 Introduction

This chapter presents results from experiments on the three most NMR favourable nuclei found in the fluorocarbon ionomers introduced in Section 1.1. These nuclei are ^{1}H, ^{13}C and ^{19}F and each provides information about different parts of the complex multiphasic structure of these materials. All samples studied in this chapter were commercial ionomers as supplied by JMTC or are materials made at JMTC labs. The chapter is broken down by the sample set studied, with 4.2 concerned with commercial ionomers, 4.3 with cast Nafion membranes and 4.4 with the Nafion component of dried catalyst inks. Within these sections, divisions are made according to sample preparation and nucleus of study.

4.2 ^{19}F and ^{1}H NMR of Proton Exchange Ionomers

Solid-state NMR is well suited to elucidating the structure and dynamics of multiphase disordered materials such as the ionomers considered here. The ability to distinguish between ionomers that differ by only a couple of CF_2 groups on their sidechains is potentially very valuable to understanding their significantly different properties and performance in fuel cells [7]. While Nafion has featured in many NMR studies [22, 111] its alternatives have had less attention, likely due to the difficultly in obtaining non-commercial ionomers. This section will compare the ^{19}F and ^{1}H NMR spectra of a range of ionomer types, supplied by JM.

In order to directly compare the effects of sidechain structure and equivalent weight of a PTFE-based PEM with the solvent and casting effects investigated in section 4.3, the ionomers were prepared for SSNMR by both the grating and rolling methods detailed in section 3.1.1.

4.2.1 ^{19}F NMR of Grated Proton Exchange Ionomers

The assignment of the ^{19}F spectrum of Nafion by Schmidt-Rohr *et al.*[46] has been used as a basis to identify the spectra of Aciplex, Solvay and Nafion ionomers shown in figure 4.1.

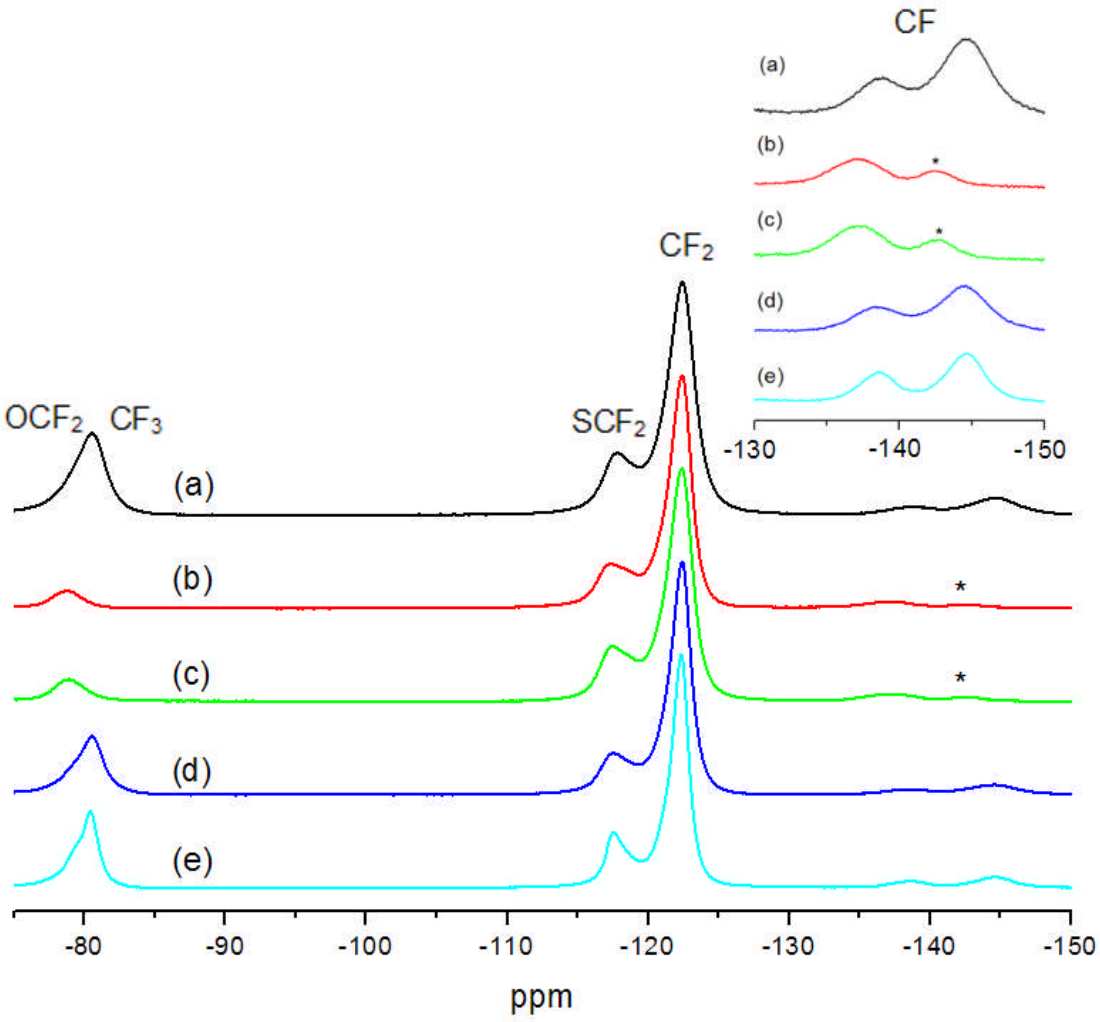

Figure 4.1: Stacked plot of ^{19}F MAS NMR spectra of grated ionomers stored at 100% RH at standard temperature and pressure before packing. Inset: the region from -130 to -150 ppm is shown expanded. The structural groups to which nuclei belong are shown above their resonances. The manufacturer and equivalent weights are as follows; (a) Nafion EW 920, (b) Solvay EW 820, (c) Solvay EW 750, (d) Nafion EW 1100 and (e) Aciplex EW 1000. All spectra taken at 470 MHz, spinning at 30 kHz.

All models and quantitative data relating to one pulse ^{19}F spectra in this chapter originate from deconvolutions made in DMfit2008 [112]. It was possible to obtain very good agreement between experimental line shapes and an automatic fit based on parameters from [46]. However, this approach does not produce peak intensities that match given sidechain structures with the exception of the Solvay system. This can be attributed to insufficient resolution between peaks in the CF_3/OCF_2 and SCF_2/CF_2 regions of the spectra. Indeed the deconvolution from [46] does not have the correct intensity contribution from the SCF_2 peaks. It is therefore

impossible to guarantee that the peak widths, intensities and locations of these fits are correct in these regions and analysis is therefore limited to a qualitative comparison and the use of the overall intensities of these regions to calculate the equivalent weight of the ionomer. Each area of the spectra will be considered and compared in turn beginning with the backbone CF_2 resonances found at –123.1 ppm. Schmidt-Rohr's deconvolution of the backbone resonances included a separate peak for each unique fluorine site along the backbone. The number of these sites will vary with equivalent weight, but it was found that all ^{19}F spectra of ionomers in this chapter could have this spectral feature fitted with just three peaks. While this does not allow us to distinguish between backbone sites its simplicity allows the use of automatic fitting algorithms. General statements about the width of the backbone resonances can still be made, but caution must be exercised when comparing ionomers with different EW. Higher EW membranes will have a greater number of fluorines between each pair of side chains. The deconvolutions in this work and those found in [46] both suggest that fluorines on the $–CF_2–$ backbone further from a sidechain branch point will be narrower and more negatively shifted towards –123.2 ppm where the ^{19}F shift of PTFE is located.

Taking the above into account when considering figure 4.1 it is observed that all peaks of the Aciplex spectra appeared at the same chemical shift positions as they did in the Nafion spectrum, but that their relative intensities and widths varied considerably. The same was not true for the ^{19}F NMR spectra of Solvay as the sidechain resonances appeared positively shifted with respect to those of the other ionomers. Two conclusions about the relationship between the structure of perfluorinated ionomers and their ^{19}F chemical shifts can be drawn from the above data. Firstly, the equivalent weight of an ionomer and number of CF_2 groups on its sidechain do not discernibly affect any ^{19}F chemical shifts. So any resulting shielding or morphological variation between the samples do not cause systematic shifts under MAS, but may well affect the interaction and anisotropy of these resonances, manifesting as variation in peak widths. In fact the lack of any affect on the ^{19}F NMR spectrum of equivalent weight change is illustrated in figure 4.2.

Assignment	Chemical Shift of Peaks (ppm)					
	OCF_2	CF_3	SCF_2	CF_2	CF(b)	CF(s)
Nafion	–81.2 –81.4	–81.7	–118.4	–119.5 –122.7 –123.2 –123.4	–139.7	–145.1
Solvay	–79.1	-	–117.7	–119.2 –121.7 –123.1	–138.1	-
Difference	2.1	-	-	-	1.6	-

Table 4.1: Chemical shifts of each of the peaks in the assignment of the ^{19}F MAS NMR spectra of Nafion and Solvay Ionomers. The Nafion assignment from [46] is referenced to PTFE at –122ppm while the Solvay assignment is reference to PTFE at –123.2 ppm. The Nafion shifts have been adjusted to correct this discrepancy.

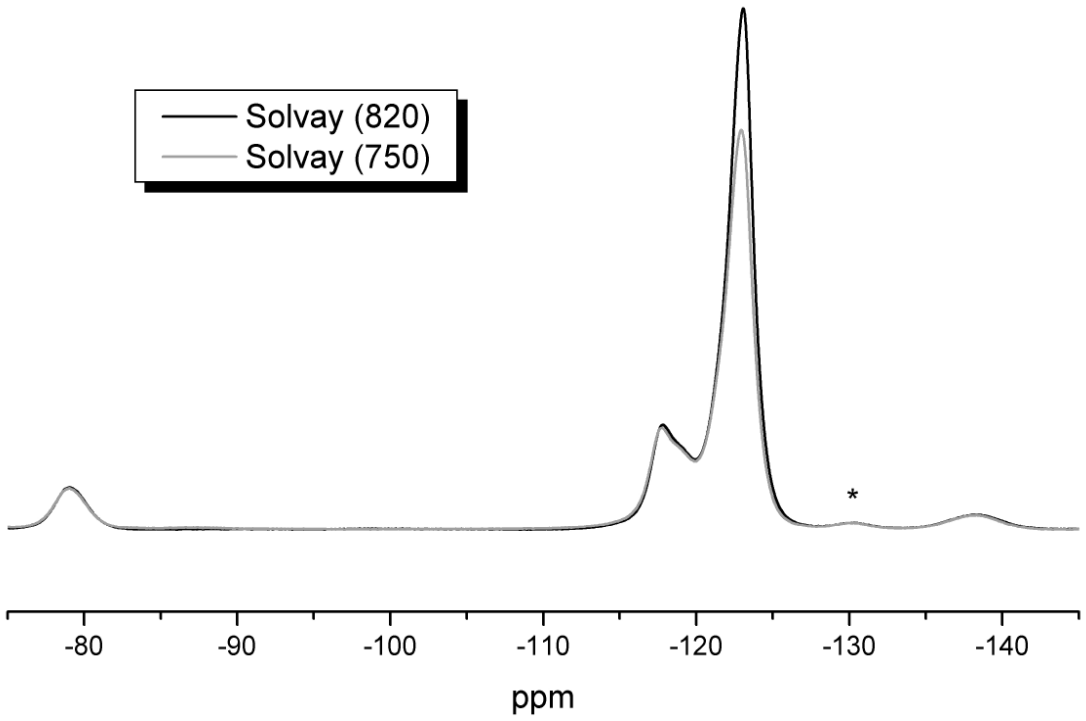

Figure 4.2: Overlaid plot of ^{19}F MAS NMR spectra of grated Solvay ionomers stored at 100% RH at standard temperature and pressure before packing. Both spectra taken at 470 MHz, spinning at 24 kHz.

The complete lack of chemical shift or peak width changes with EW suggest that even at low EW the chemical environment and mobility of the fluorines along the sidechain are not affected by one another at all. Secondly, the chemical shielding, and therefore bonding, along the entire length of the ionomer sidechain is significantly affected by the loss or gain of an ester link. Indeed, the effect on a fluorine separated from such a link by five bonds is still measurable. The sulphonic group at the terminus of the chain however, seems to have little influence beyond its next nearest neighbour. This is entirely expected from the chemical shift assignment from [46] as a next nearest neighbour ester oxygen shifts a fluorine resonance by around 40 ppm rather than 5 ppm for the next nearest neighbour of the sulphonic group. This effect was not noted by a study on the degradation products of Nafion and Hyflon [113] another short chain fluoropolymer like the Solvay ionomer. Some difference can be seen in the published spectra but not as large as observed here. It is useful to note for later analysis that only a change in the bonding environment of the fluorines has resulted in a chemical shift and that the length and frequency of side chains and any morphological consequences do not result in systematic shift changes.

Although there is a large variation in the widths of peaks across the sample set, this is not observed in figure 4.5 in section 4.2.2 and must therefore derive from either a variation in water content or differences in the level of disorder introduced into the system by the grating of the ionomer. Neither cause contributes to an understanding of the structure or dynamics of these materials in the state they would be used and therefore will attract no further comment here. ^{1}H NMR of the grated ionomers was excluded from this section for same reasons.

4.2.2 ^{19}F and ^{1}H NMR of Rolled Proton Exchange Ionomers

In order to be confident that the ^{19}F and ^{1}H NMR spectra of the ionomers being considered are not affected by stresses caused by grating, the samples were also prepared for NMR by the rolling method in section 3.1.1. The importance of the preparation method is best displayed in Figure 4.20 in Section 4.3.2. Figure 4.5 shows the ^{19}F spectra of the ionomers prepared by rolling after storage at 100% humidity. These spectra must be compared to those in figure 4.1 to understand any affect the preparation methods have on the structure of the ionomers. Considering first the

Solvay ionomers, (b) and (c), the only significant change in peak width is that of the fluorines assigned the SCF_2 group close to the end of the sidechain in both samples, which is narrower in the spectra of rolled samples compared to the grated ionomer.

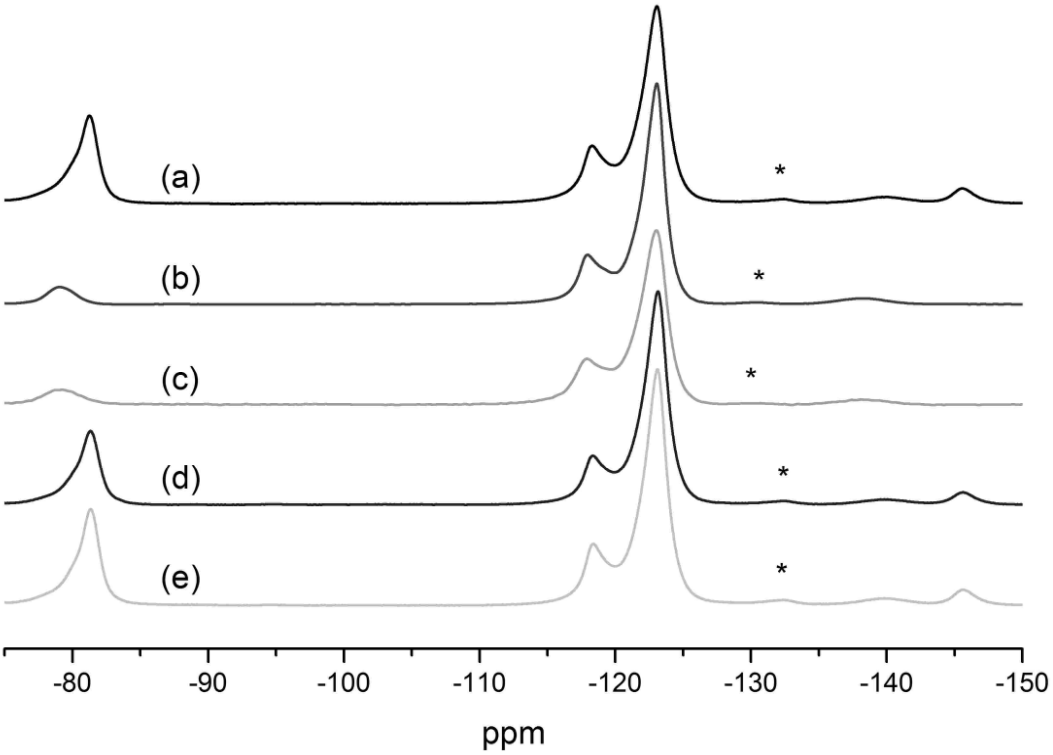

Figure 4.5: Stacked plot of ^{19}F MAS spectra of rolled ionomers stored at 100% RH at standard temperature and pressure before packing. The manufacturer and quoted equivalent weights are as follows; (a) Nafion EW 920, (b) Solvay EW 820, (c) Solvay EW 750, (d) Nafion EW 1100 and (e) Aciplex EW 1000. All spectra taken at 470 MHz, spinning at 24 kHz.

The mobility of this group is consistently the most sensitive to changes in the ordering of an ionomer as will be shown in sections 4.3 and 4.4. No difference in peak positions or intensities are observed other than an apparent peak position change which is due to narrowing of the SCF_2 resonance in comparison to the sidechain CF_2 resonances. So while the mobility of the fluorines at the end of the sidechain is affected by grating of the ionomer the spectrum is otherwise unchanged. Spectra (a), (d) and (e) of the longer sidechain ionomers show a similar pattern of differences with only the SCF_2 and CF_3 peaks, likely the most mobile species in the sidechain because of their small peak widths, narrowing in the rolled ionomer spectra. Again apparent peak position changes are observed but likely due to overlapping peaks changing

widths at different rates. In summary, the spectral differences due to preparation method of the ionomers is minor compared to those shown in section 4.3.2. This means that the conclusions drawn in 4.3.1 about the lack of influence of sidechain length and EW on mobility are valid regardless of preparation method.

As alluded to above, the equivalent weight of an ionomer can be calculated by ^{19}F NMR. The EW values quoted so far have been given by the manufacturers and are almost certainly the result of titration experiments. While it is possible to fit the spectra of the Solvay samples so that the relative intensities of all but the SCF_2 peak are consistent with one another. A more accurate EW value will result from summing the SCF_2 with the backbone fluorines and taking this into account when calculating the number of backbone $–CF_2–$ links between sidechains. This same approach is taken with the other three spectra for which no convincing deconvolution can be obtained. Instead only the relative intensities of spectral areas is considered. In order to calculate the equivalent weight of an ionomer from ^{19}F NMR it is necessary to compare the relative intensity from the backbone and SCF_2 fluorines (*A*) with respect to the intensity of the other sidechain fluorines in the structure (*B*). As the intensity contribution per fluorine will be the same for backbone and sidechain fluorines (assuming complete relaxation) it follows that:

$$\frac{F(b)+\Theta}{A}=\frac{\Phi}{B} \qquad [4.1]$$

where *F(b)* is the number of backbone fluorines in a repeat group, Φ is the known number of CF, CF_3 and OCF_2 fluorines on each sidechain and Θ is the number of other CF_2 fluorines on the sidechain. This rearranges to:

$$F(b)=\frac{\Phi A}{B}-\Theta\,. \qquad [4.2]$$

The equivalent weight of an ionomer is therefore given by half *F(b)* (the number of backbone CF_2 units) multiplied by the molecular mass of a CF_2 group (50) added to the molecular mass of one sidechain (Λ)

$$EW = 25\left(\frac{\Phi A}{B} - \Theta\right) + \Lambda . \qquad [4.3]$$

Therefore the equivalent weight of a Solvay ionomer is given by:

$$EW = 25\left(\frac{3A}{B} - 2\right) + 227 , \qquad [4.4]$$

and that of the Nafion or Aciplex ionomers by:

$$EW = 25\left(\frac{9A}{B} - 2\right) + 393. \qquad [4.5]$$

By analysing the spectra shown in figure 4.5 equivalent weights were calculated and are compared to the supplier's values in table 4.2.

There is a striking difference in the disagreement between the NMR and supplier values between the short chain Solvay samples and the longer chain ionomers. While the ^{19}F NMR results suggest a value 3-4% above the supplier value for both Solvay samples, the calculated EW for Nafion and Aciplex ionomers is 7-14% lower than would be expected.

Ionomer	Supplier's EW Value	NMR Calculated Value	NMR/Supplier Ratio
Nafion	920	852 ± 10	0.93
Solvay	820	847 ± 5	1.03
Solvay	750	780 ± 5	1.04
Nafion	1100	942 ± 10	0.86
Aciplex	1000	881 ± 10	0.88

Table 4.2: Comparison of calculated and supplied values of the equivalent weight of Solvay ionomers. Ratio is expressed as a fraction of the supplier's value.

If the supplier's values are based on titration results its is possible that NMR would detect some sulphonic acid groups that do not have access to the wider water network and would therefore not interact in any titration experiments leading to an overestimation of the EW by suppliers. It is unclear what could cause a systematic difference between titration and NMR results such that NMR would detect less sulphonic groups in a given mass of ionomer. However, it is quite possible that the EW values quoted by suppliers are in fact averages and individual membranes and batches vary despite efforts to control synthesis to produce ionomers of a certain EW. Additionally the different manufacturers may use different techniques to measure and control the EW of their ionomers, resulting in the range of discrepancies seen in table 4.2

While ^{19}F NMR was used to explore the effect of preparation method on the ionomers and to calculate equivalent weights, ^{1}H NMR was used to probe the water in the ionomers. Figure 4.6 shows these spectra for each of the five ionomers. Chemical shifts for the water peaks vary from 5.9 to 7.2 ppm, a reflection of the different average water to acid group ratios that are a result of variation of water uptake between the ionomers [36]. More significant are the widths and lineshapes of the water spectra which could indicate the distribution of water molecules to acid group ratios among micelles in the ionomer. A narrow line indicating a similar pH in all micelles while a broad line suggests greater inhomogeniety in the water distribution in the ionomer. While not all the lineshapes were symmetrical peaks they were characterised by their FWHM as an approximation to their overall distribution width as shown below in table 4.3.

There is no trend between equivalent weight or sidechain length and the width of the ^{1}H spectrum. It may be that the method by which the ionomer is formed into a membrane is the most significant factor in determining the homogeneity of pH in the ionomer. A difference between extruded and cast membranes may be significant but without more detailed information about the manufacturing of the ionomers this cannot be determined in this study.

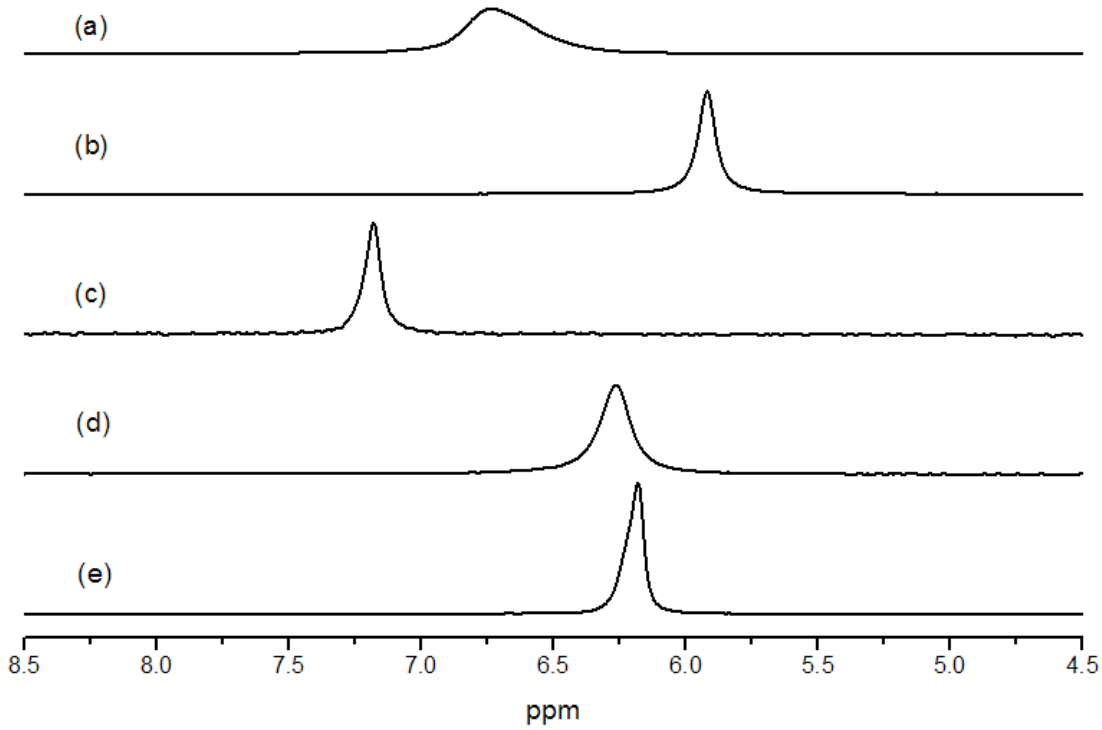

Figure 4.6: Stacked plot of ^{1}H MAS spectra of water in rolled ionomers stored at 100% RH at standard temperature and pressure before packing . The manufacturer and quoted equivalent weights are as follows; (a) Nafion EW 920, (b) Solvay EW 820, (c) Solvay EW 750, (d) Nafion EW 1100 and (e) Aciplex EW 1000. All spectra taken at 500 MHz, spinning at 12.5 kHz.

Ionomer	^{1}H NMR line width (± 0.01 ppm)
Nafion 920	0.29
Solvay 820	0.08
Solvay 750	0.07
Nafion 1100	0.13
Aciplex 1000	0.07

Table 4.3: ^{1}H NMR linewidths of water in rolled ionomers stored at 100% RH at standard temperature and pressure before packing. Ionomers are listed by manufacturer and equivalent weight.

The ^{1}H NMR data of the ionomers can be used to inform our understanding of the ^{19}F NMR as other work suggests a clear link between water content and sidechain mobility. If a link between the length and mobility of sidechain is to be confirmed the variable of water content must be eliminated as a cause of the differences. Figure 4.6 shows that the Solvay 820 ionomer has the highest water to acid ratio yet the mobility of its sidechain groups appears less than the longer chain ionomers with lower water content.

4.3 ^{19}F and ^{1}H NMR of Cast Nafion Membranes

While in section 4.2 solid-state NMR was used to investigate the differences in structure and dynamics of PTFE-based ionomers from several different manufacturers, this section will consider only the DuPont ionomer Nafion. It is desirable for JM to be able to dissolve the received ionomer and cast it to their own specifications for use in membrane electrode assemblies. These cast membranes exhibit different mechanical properties, a key area of study for the commercial use of these materials, dependent upon the method by which they are cast. This section will attempt to understand these differences by studying several cast membranes by ^{19}F and ^{1}H NMR.

Both methods of preparation for NMR, detailed in section 3.1.1, were used for materials studied here. First the grating method which prepares the material in the manner most suited for high speed MAS will be considered in section 4.3.1, followed by the rolling method in section 4.3.2 which seeks to maintain the properties of the material as close as possible to those of membranes in a functioning MEA.

4.3.1 ^{19}F and ^{1}H NMR of Grated Cast Nafion Membranes

Initial studies on the cast Nafion samples supplied by JM used the grating method of preparation and packing as described in section 3.1.1. It was immediately apparent that the variability in the ambient humidity during preparation was sufficient to cause differences in both ^{1}H and ^{19}F NMR spectra of samples prepared on different days different.

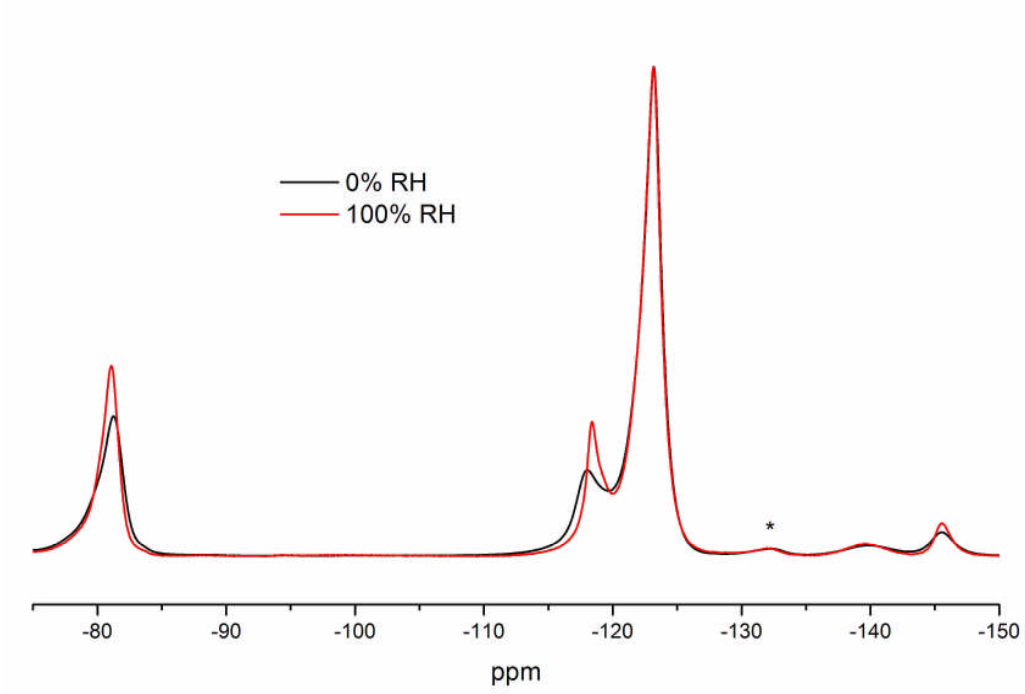

Figure 4.7: Overlaid plot of ^{19}F MAS NMR spectra of a grated Nafion cast membrane stored in different humidity conditions. Spectra taken at 470 MHz, spinning at 24 kHz.

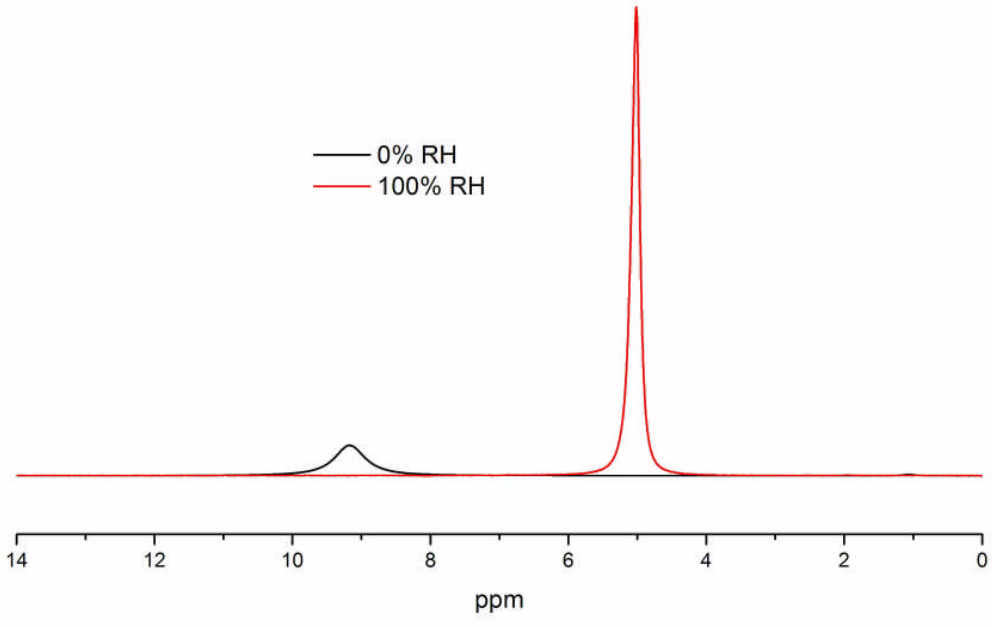

Figure 4.8: Overlaid plot of ^{1}H MAS NMR spectra of water in grated Nafion cast membranes stored in different humidity conditions. Spectra taken at 500 MHz, spinning at 12.5 kHz.

There are three noteworthy effects of increasing the water content in these cast membranes and one noteworthy similarity. The first effect is the narrowing of the fluorine peaks assigned to groups on the side chains of the ionomer. As these peaks will narrow further with an increase in MAS spinning speed as shown in section 4.5, this is more likely to be caused by increasing mobility of the fluorines on the side chain rather than a reduction in static disorder. It is also noteworthy that hydration has no effect on the width of the sidechain or branch CF fluorines. A lack of change in mobility or order suggests that the hydrophobic helical backbone does not change in confirmation with uptake or removal of water. This is perhaps surprising as the ionomer will swell with water uptake. These two observations can be most simply reconciled by supposing that the backbone bundles move closer or further away from one another with changes in water content, but do not become significantly more or less disordered to accommodate the water within the multiphasic structure.

Moving onto the ^{1}H spectra shown in figure 4.8 it is expected that an increase in water within the membrane will result in a shift of the water resonance. As the water phase within the membrane is interacting with a fixed number of sulphonic acid groups the pH will vary greatly with the membrane water content. The relationship between the chemical shift of a ^{1}H water resonance and the pH of the liquid is well known[36]. Water appears at 4.8 ppm without acid and shifts towards 14 ppm as acid concentration increases. This is because there are in fact two distinct water proton environments in an acid. One that is closely associated with an acid group and another that is not and therefore appears as pH neutral water. However, exchange between these two environments is so rapid compared to the NMR time scale that only one resonance appears in the spectrum. The chemical shift of this combined resonance is a weighted average of the two distinct environments, determined by the relative amounts of water protons in each state. The low humidity membrane will have less water and a higher acid concentration and therefore lower pH resulting in a more positive chemical shift of the water resonance than the water in the high humidity membrane.

In all subsequent studies, samples were stored at a controlled humidity before or after packing so as to eliminate this undesirable effect. Of course there is no guarantee that all membranes will have the same water content if stored at the same

relative humidity, but it can be said that any particular membrane will have a similar water content throughout all experiments. While keeping the membranes at a high water content most accurately simulates their condition in an operating fuel cell [7], the low water content condition allows the membranes to be compared to one another with a smaller disparity in water content between samples as initial experiments revealed that the membranes will contain different proportions of water if there is humidity in their environment. In a completely dry state the membranes will relinquish all water apart from one molecule per acid group. For this reason ^{19}F and ^{1}H NMR of the membranes in both states are included.

When comparing the ^{19}F MAS NMR spectra shown in figure 4.9 it should first be noted that the membranes cast from aqueous and organic solvent were formed from ionomer stock of different equivalent weight, 1100 for the aqueous membranes and 1000 for the organic. The most significant result of this disparity will be a change in the relative intensity of the -CF_2- backbone resonances which will be greater for the aqueous membranes as there are more backbone fluorines per repeat unit of the ionomer. Even at the relatively high field of 11.7 T and spinning at 30 kHz, a one dimensional spectrum does not allow the clear identification of individual peaks from the side chain CF, CF_2 and CF_3 groups. Rather we observe groups of peaks which do not necessarily allow us to discern which resonance or resonances are causing changes in the spectral line shape and whether these changes are in peak width or position.

Even so, several useful observations can be made from the spectra in figure 4.9. The greatest contrast is between the two membranes cast from aqueous solution. The air dried sample has the narrowest spectral features associated with side chain fluorine groups of the four spectra while the rapidly IR dried sample has the widest. In light of the results from variable spinning speed, variable temperature and experiments at higher water content that are presented in later in this chapter it seems reasonable to explain these differences in terms of the mobility of fluorine groups on

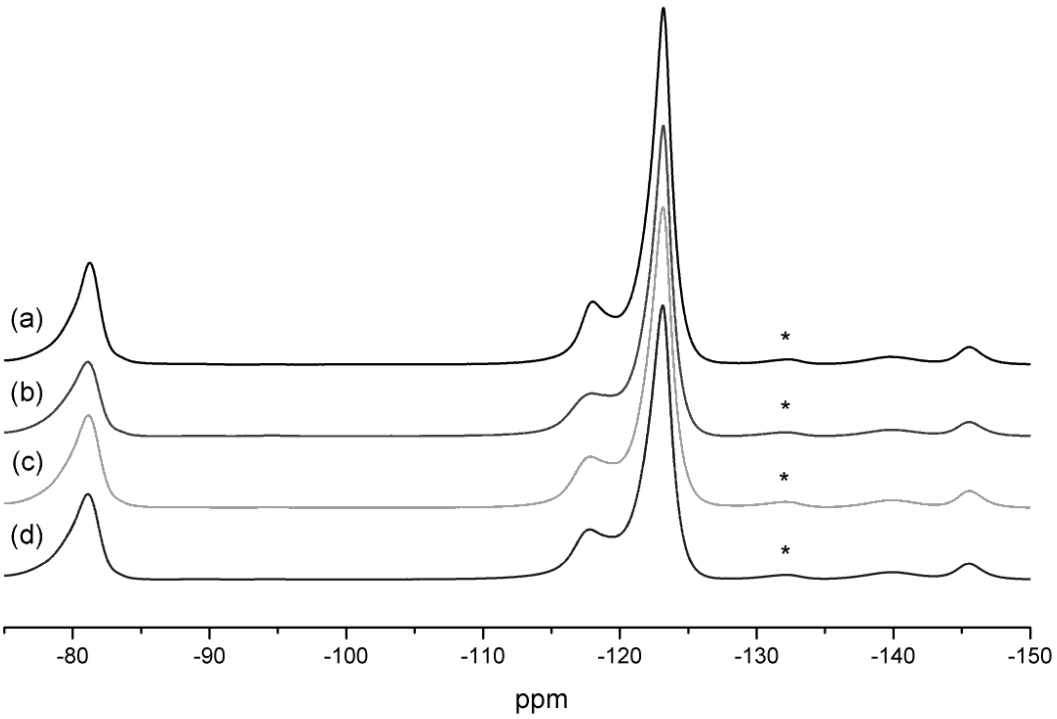

Figure 4.9: Stacked plot of ^{19}F MAS NMR spectra of grated Nafion cast membranes stored at 0% RH at standard temperature and pressure after packing. The membranes were cast and dried as follows; (a) aqueous solvent air dried, (b) aqueous solvent IR dried, (c) organic solvent air dried and (d) organic solvent IR dried. All spectra taken at 470 MHz, spinning at 24 kHz.

the side chains of the ionomers. There is little observable difference between the organic cast membranes under these conditions, but the side chain mobility of these ionomers appears to lie in between the two aqueous samples. Finally it should be noted that within each pair of membranes of similar EW there is no difference in the width of the resonances assigned to the fluorines in the CF_2 groups on the ionomer backbone.

Figure 4.10 shows ^{19}F MAS NMR spectra of the same four membranes stored under high humidity conditions so as to observe the ionomers in a state of higher water content. It is immediately clear that linewidths are narrower in these spectra than the corresponding spectra shown in figure 4.9. Once again the peaks of the sidechain CF, CF_2 and CF_3 are narrower from the air dried aqueous sample than from the IR dried aqueous sample. We also see a narrower peak corresponding to the backbone

fluorines than was not observed when the samples were kept dry before the experiment. As seen in figure 4.9 IR drying appears to have a less dramatic effect on the spectra of the membranes cast from organic solvent, but unlike the dry ionomers, differences in line widths are large enough for confidence to be had in their significance. In figure 4.10 we see narrower CF_2 and CF_3 side chain resonances in the

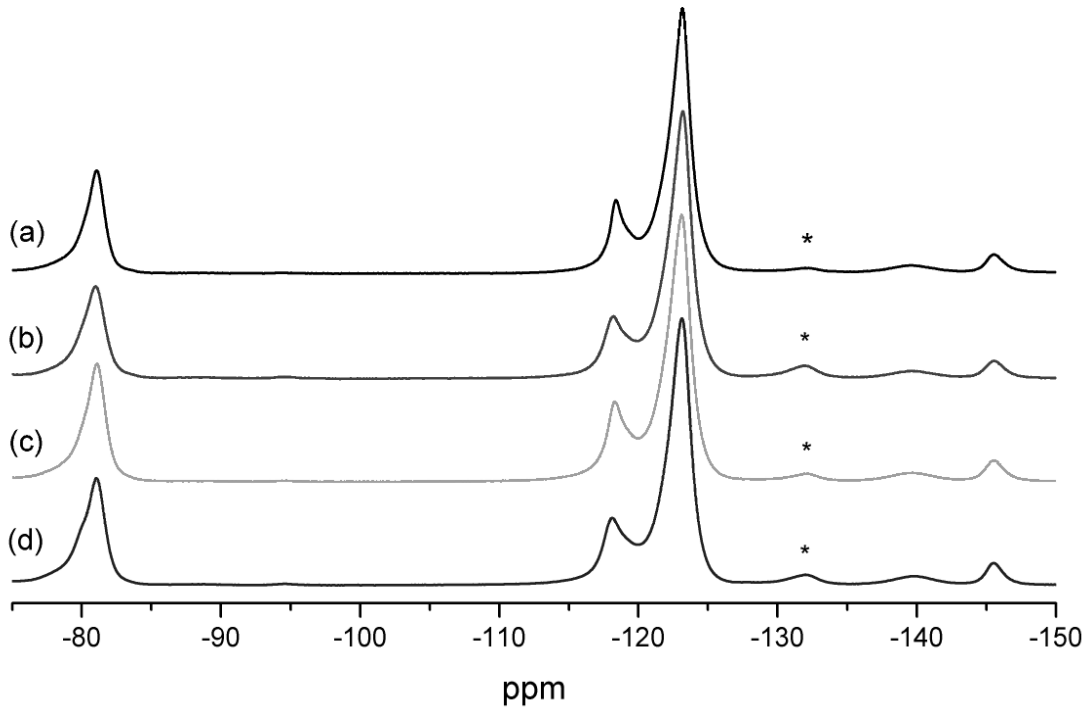

Figure 4.10: Stacked plot of ^{19}F MAS NMR spectra of grated Nafion cast membranes stored at 100% RH at standard temperature and pressure before packing. The membranes were cast and dried as follows; (a) aqueous solvent air dried, (b) aqueous solvent IR dried, (c) organic solvent air dried, (d) organic solvent IR dried. All spectra taken at 470 MHz, spinning at 24 kHz.

air dried membrane, but no change or the opposite trend in the branch point and side chain CF fluorines respectively. No difference in line width is seen in the backbone CF_2 peak.

The comparison of the aqueous and organic cast membranes is more complex for the wet stored ionomers. For the CF_3 and OCF_2 groups, the air dried aqueous membrane has the narrowest peaks, the organic air dried the second narrowest peaks, followed by the organic IR dried membrane and the aqueous IR dried spectrum gives

the widest resonances. This matches the order seen in the dry membranes. The fluorines closest to the end of the side chain in the SCF_2 group appear most mobile in the aqueous air dried sample, followed by the organic air dried sample which is more mobile than the IR dried membranes which have equally wide peaks. The CF branch point peak is indistinguishable across all samples and the backbone peaks are not comparable due to variations in EW across the sample set. The side chain CF group differs from the trends observed above with the organic IR dried membrane having the narrowest peak, but the order being otherwise unchanged. It is possible that with such a small peak this is the result of phasing and baseline correction rather than a morphological effect.

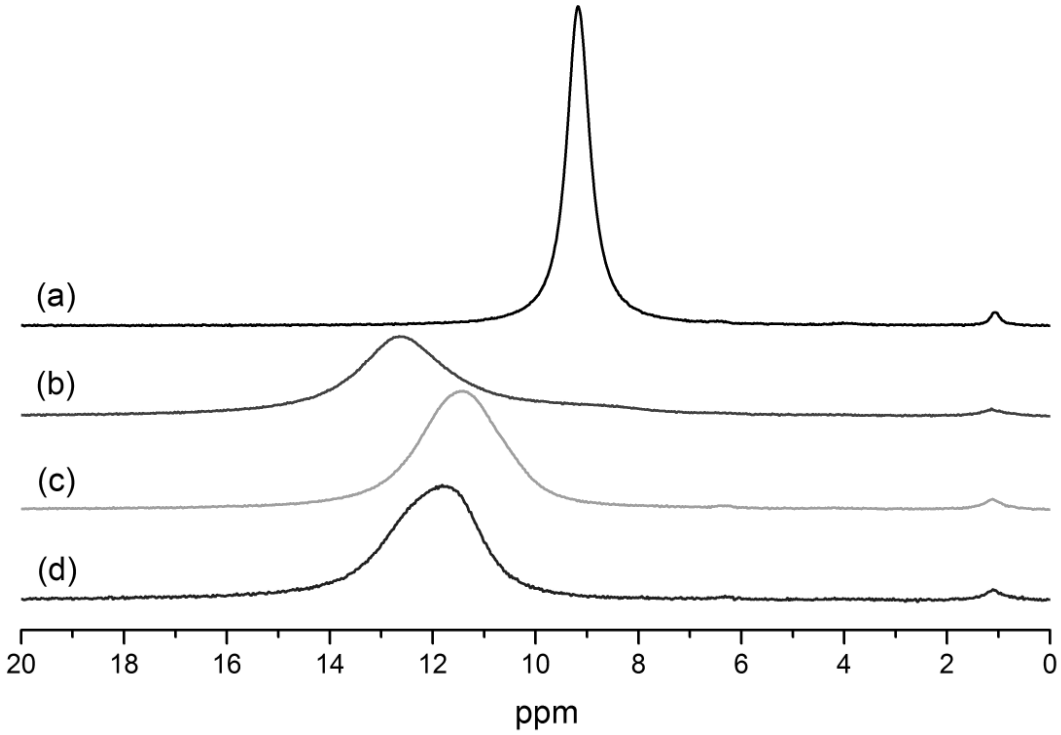

Figure 4.11: Stacked plot of ^{1}H MAS NMR spectra of water in grated Nafion cast membranes stored at 0% RH at standard temperature and pressure after packing. The membranes were cast and dried as follows; (a) aqueous solvent air dried, (b) aqueous solvent IR dried, (c) organic solvent air dried and (d) organic solvent IR dried. All spectra taken at 500 MHz, spinning at 12.5 kHz.

While the ^{19}F spectra of the dry grated Nafion cast membranes showed variation only in peak widths, the ^{1}H data shown in Figure 4.11 differs in the number and position of peaks as well as their widths. The main feature of each spectrum

which is observed between 7 and 16 ppm is attributed to water that is bound inside the membranes [34-35]. The exchange of the water between the bulk and hydrogen bonded states result in a positive shift from bulk liquid water found at ~4.8 ppm. The second, much smaller feature found at 1.1 ppm in all spectra is likely due to the presence of residual organic solvent left within the membrane or indicate the presence of alkane protons on the ionomer itself due to incomplete fluorination of the ionomer. In neither case is this peak significant for the comparison of the membranes.

Although broad and overlapping, there are sufficiently few peaks to allow a reliable quantitative deconvolution of all four spectra. As throughout this work, single peaks are fitted to a combination of Gaussian and Lorentztian broadening that best expresses the line shape of the data. Deconvolutions with multiple peaks are then fit using the same ratios as found in the spectra with the fewest numbers of peaks. These are presented below with a table summarising the fits.

Peak Position (ppm)	AqnAir		AqnIR		OrgnAir		OrgnIR	
	Int %	Width	Int %	Width	Int %	Width	Int %	Width
9.2	98	0.53 ± 0.05	15	3.70 ± 0.1	-	-	-	-
12.6	-	-	82	2.04 ± 0.1	-	-	-	-
11.4	-	-	-	-	97	1.91 ± 0.1	32	1.03 ± 0.1
11.9	-	-	-	-	-	-	15	0.91 ± 0.1
12.5	-	-	-	-	-	-	50	1.63 ± 0.1
1.1	2	0.30 ± 0.05	3	0.70 ± 0.05	3	0.53	3	0.55 ± 0.05

Table 4.4: Deconvolution data for the fits of figures 4.12. Intensities are calculated by DMfit and given as a percentage of the total intensity of the fit (not the raw data) rounded to the nearest percent. Widths, also given by DMfit are FWHM in ppm. All peaks are a 50:50 weighted combination of Gaussian and Lorentzian lineshapes.

The spectrum of the air dried membrane cast from water shows a single Gaussian water peak at 9.2 ppm, significantly shifted from bulk water, but seemingly the closest environment to bulk water observed in this data set. The deconvolution of the aqueous IR membrane shown in (b) of figure 4.12 contains the same peak at

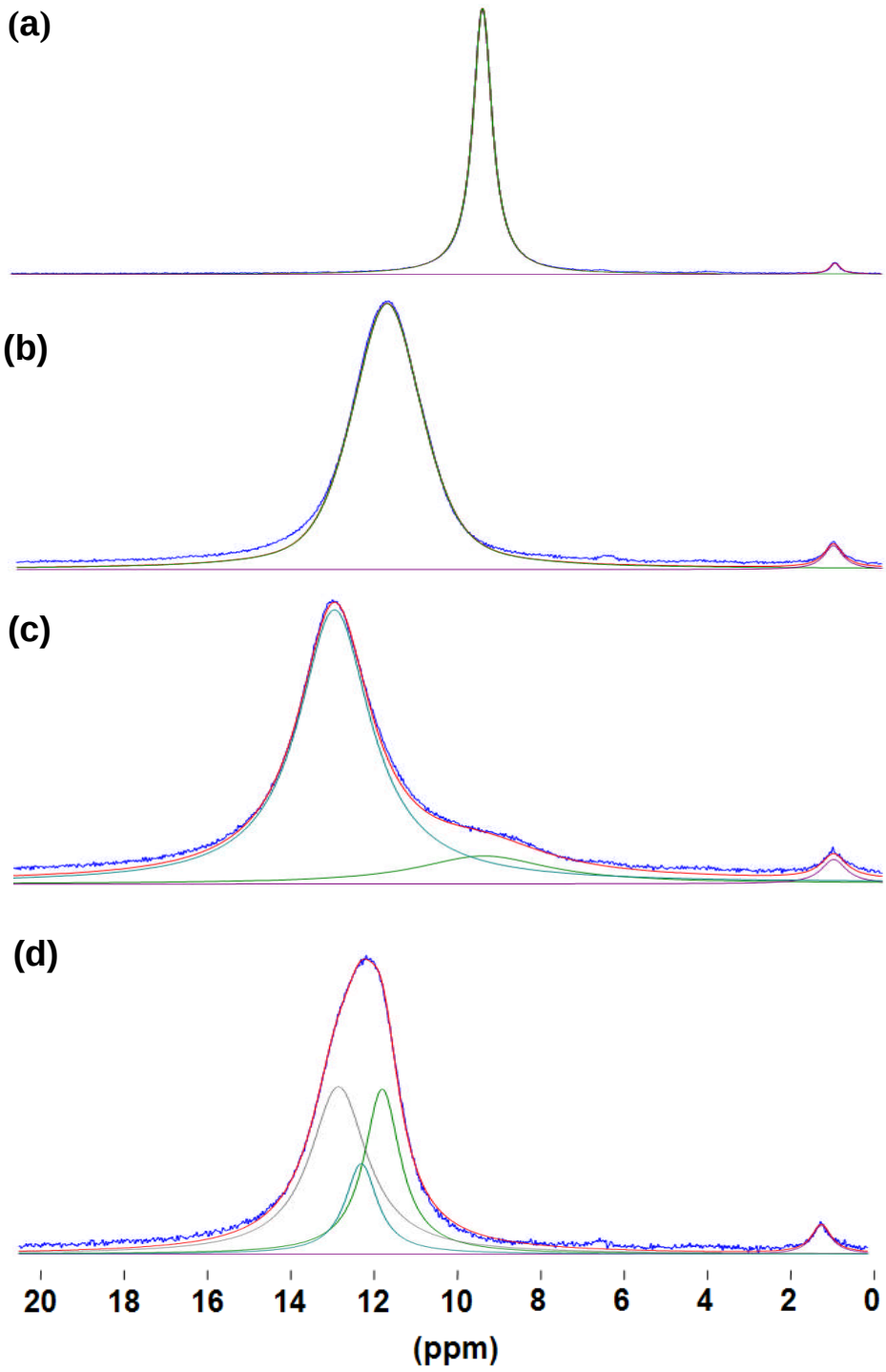

Figure 4.12: Stacked plot of deconvoluted ^{1}H MAS NMR spectra of grated Nafion cast membranes stored at 0% RH at standard temperature and pressure after packing. The membranes were cast and dried as follows; (a) aqueous solvent air dried, (b) aqueous solvent IR dried, (c) organic solvent air dried and (d) organic solvent IR dried. All spectra taken at 500 MHz, spinning at 12.5 kHz.

9.2ppm observed in (a), but broader and greatly reduced in intensity. Additionally, 85% of the water in the membranes is observed in a peak at 12.6 ppm. Like the other slow dried sample, the air dried membrane cast from organic solvent displays a single water environment but more positively shifted at 11.4 ppm. The water feature fitted in (d) is deconvoluted into three peaks centred at 11.4, 11.9 and 12.5 ppm and while a good fit can be made easily by automatic iteration within DMfit, the exact fit parameters cannot necessarily be relied upon. It can be stated with confidence that more than two environments exist as no good fit can be found with only two peaks. However, whether there are three environments with a Gaussian/Lorentzian distribution or in fact a greater numbers of these or other patterns of distribution cannot be determined with confidence with a one dimensional experiment. In all four deconvolutions the peak at 1.1 ppm is taken to be protons from CH_3 groups in residual organic molecules within the membrane.

When the cast membranes were hydrated by storage at 100% relative humidity the proton spectra were all significantly different to those recorded when the samples were kept at 0% RH. It was possible to fit the water protons in the ^1H spectra of the aqueous air, aqueous IR and organic air samples using a single peak, the deconvolutions are shown in figure 4.17 and the details of the fits from DMfit are summarised in table 4.5. The spectrum of the hydrated organic IR dried could not be fit by less than five overlapping peaks so it was decided any fit would be poorly constrained. Two common trends can be identified across all three fitted spectra. All peaks are shifted to lower positive ppm values towards the bulk water environment and are narrowed when compared to lower humidity conditions, (b) and (c) of figure 4.14 show a single peak while the same samples exhibited multiple Gaussian/Lorentzian distributions at low RH. The spectrum of the organic IR dried membrane also shows a shift of 1.5-2 ppm towards the bulk water environment. Peaks 4 and 5 were attributed to residual organic molecules.

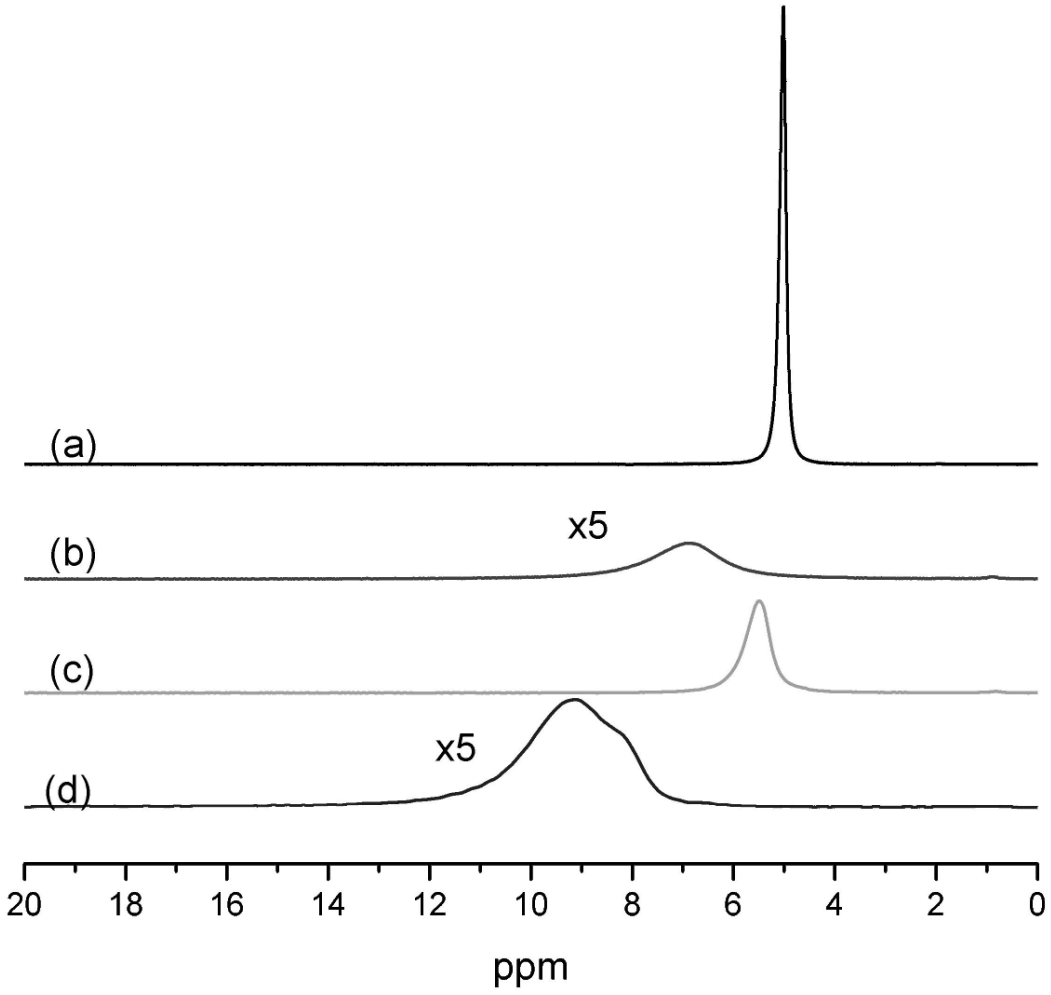

Figure 4.13: Stacked plot of ^{1}H MAS NMR spectra of water in grated Nafion cast membranes stored at 100% RH at standard temperature and pressure before packing. The membranes were cast and dried as follows; (a) aqueous solvent air dried, (b) aqueous solvent IR dried, (c) organic solvent air dried, (d) organic solvent IR dried. All spectra taken at 500 MHz, spinning at 12.5 kHz.

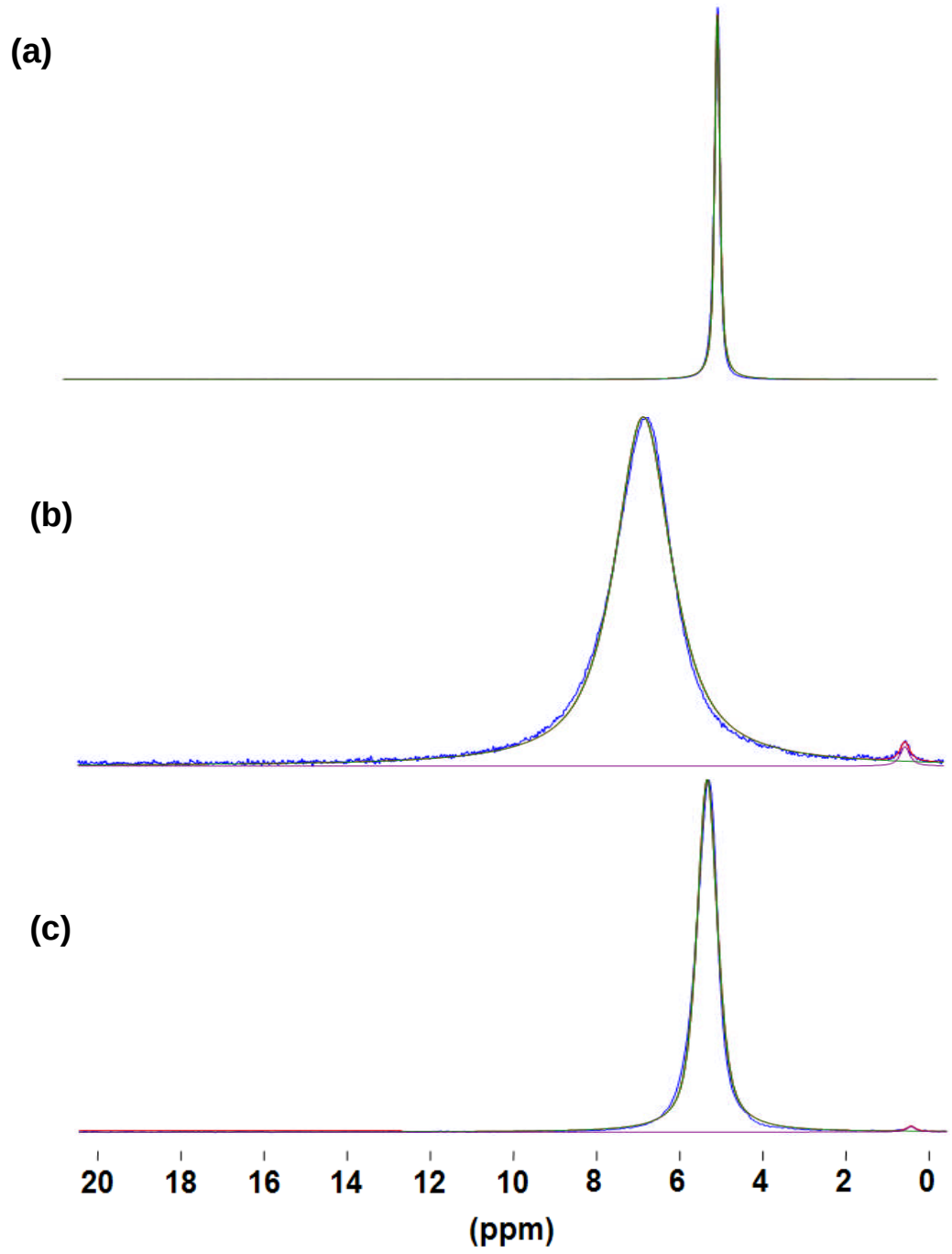

Figure 4.14: Stacked plot of deconvoluted ^{1}H MAS NMR spectra of water in grated Nafion cast membranes stored at 100% RH at standard temperature and pressure before packing. The membranes were cast and dried as follows; (a) aqueous solvent air dried, (b) aqueous solvent IR dried, (c) organic solvent air dried. All spectra taken at 500 MHz, spinning at 12.5 kHz.

Position	AqnAir		AqnIR		OrgnAir	
	Int %	Width	Int %	Width	Int %	Width
5.0	100	0.15 ± 0.01				
6.9			99	1.58 ± 0.1		
5.5					99	0.56 ± 0.05
0.9			1	0.26 ± 0.05		
0.8					1	0.23 ± 0.05

Table 4.5: Deconvolution data for the fits of figure 4.14. Intensities are calculated by DMfit and given as a percentage of the total intensity of the fit (not the raw data) rounded to the nearest percent. Widths, also given by DMfit are FWHM in ppm.

In summary, ^{19}F and ^{1}H NMR spectra of the grated cast membranes showed variation across the four samples. The differences were more pronounced in spectra of both nuclei when the samples were kept dry than when stored at 100% RH. This could be explained if the presence of more water in the membranes leads to a greater freedom of motion of both water protons and fluorine nuclei on a time scale faster than NMR. This increase in mobility could then be masking variations in disorder or interactions with or between side chains. It is expected that membranes swollen with more water would have larger water micelles and channels in which the water molecules would be in a bulk-like state for a longer proportion of the time.

The correlations between the relative shift and width of the water features appearing in the ^{1}H NMR spectra and the width of the side-chain fluorine peaks in the ^{19}F NMR spectra is strong. When sorted according to these spectral measurements the high humidity samples appear in the same order in all three cases. A different but equally consistent order is found in the low humidity observations. This is clear evidence that the same morphological change or changes are causing the variation in the NMR spectra of both nuclei. While there are trends seen across the sample set at both humidity levels, the same degree of variation is not observed when the samples are not grated in section 4.3.2. This leads to the conclusion that the large differences in the spectra are a result of the different mechanical properties of the membranes rather than a cause of them. For this reason discussion of the links between casting method and the NMR spectra will be left for section 4.3.2.

4.3.2 ^{19}F and ^{1}H NMR of Rolled Cast Nafion Membranes

Although the grating method of ionomer preparation detailed in section 3.1.1 allows for the greatest mass of sample in a rotor it is clear from figure 4.20 and 4.21 that significant changes in the ^{19}F and ^{1}H NMR spectra result from morphological changes likely caused by the stress on the ionomer during grating.

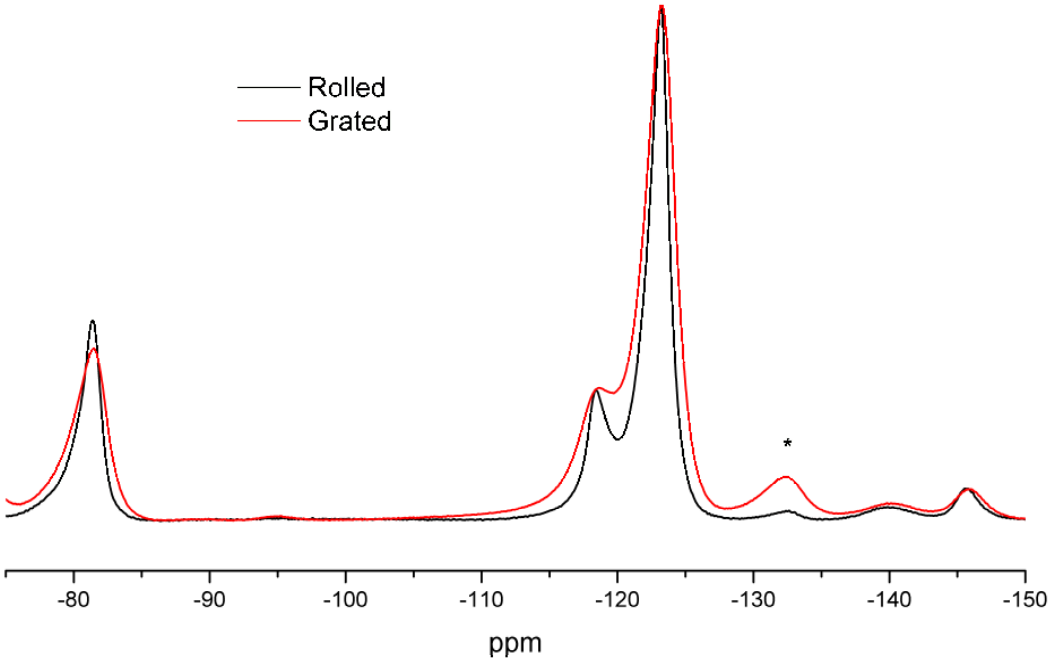

Figure 4.15: Overlaid plot of ^{19}F spectra of rolled and grated Nafion cast membranes stored at ambient humidity before packing. Spectra taken at 470 MHz, spinning at 24 kHz. Spectra normalized to intensity of backbone peak.

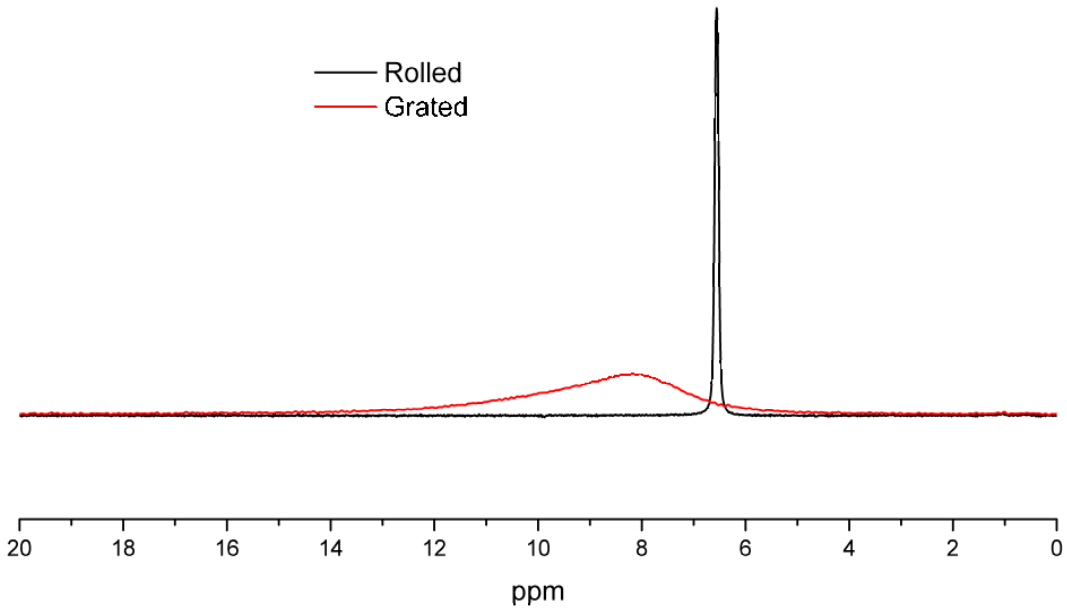

Figure 4.16: Overlaid plot of ^{1}H spectra of water in rolled and grated Nafion cast membranes stored at ambient humidity before packing. Spectra taken at 500 MHz, spinning at 12.5 kHz.

Both the rolled and grated samples were kept hydrated at 100% RH so Figure 4.15 shows that grating the membrane has a significant effect on the structure or dynamics of the ionomer, indicated by a broadening of all the peaks in the spectra. The sensitivity of peak width of both rolled and grated membranes to higher MAS spinning speeds suggests that the peaks still contain an element of broadening from interactions that are averaged by MAS rather than being purely due to chemical shift variation from disorder in the solid. So while it is possible that static disorder has caused the broadening, the MAS dependency of peak width and the knowledge that both sidechains and backbone are mobile [47] especially with a high water content, supports the argument that a difference in the ionomer dynamics results from the stress and strain on the membrane caused by grating.

Meanwhile, the ^{1}H NMR comparison in figure 4.16 shows a narrow water peak at 6.6 ppm in the spectrum of the rolled membrane which contrasts very

markedly with a much broader grated membrane water spectrum. As the lineshapes are both wider than bulk liquid water and their widths are insensitive to MAS speed above 5 kHz it can be surmised that their width is purely dependent upon the degree of variation in the ratio of water molecules to sulphonic acid groups in the local environment. This leads to the conclusion that the grated membrane does not absorb as much water as the average chemical shift is higher and that the inhomogeneity of the local pH is much greater after grating. It is likely that grating breaks connectivity in the water network as otherwise it might be expected that such a large degree of variation would be eliminated by diffusion through the network.

The evidence presented in figures 4.15 and 4.16 suggests that the grating method does not maintain the ionomer in a similar conformation as supplied and used in fuel cells. Therefore it would be unwise to attribute spectral differences in figures 4.7-4.19 to changes due to casting method rather than the membranes' different responses to grating. While section 4.3.1 does not inform us about the membranes properties as would be found *in-situ* it has provided valuable information on how structural and dynamic differences between ionomers can be determined from a combination of ^{1}H and ^{19}F NMR.

All experiments in this chapter unless otherwise specified were carried out with the temperature of the sample controlled within ± 0.1°C of 21°C or 25°C. However, as PEMFCs routinely operate at temperatures up to and exceeding 100°C [7] variable temperature experiments were conducted in an attempt to determine whether the materials experience any significant changes when heated.

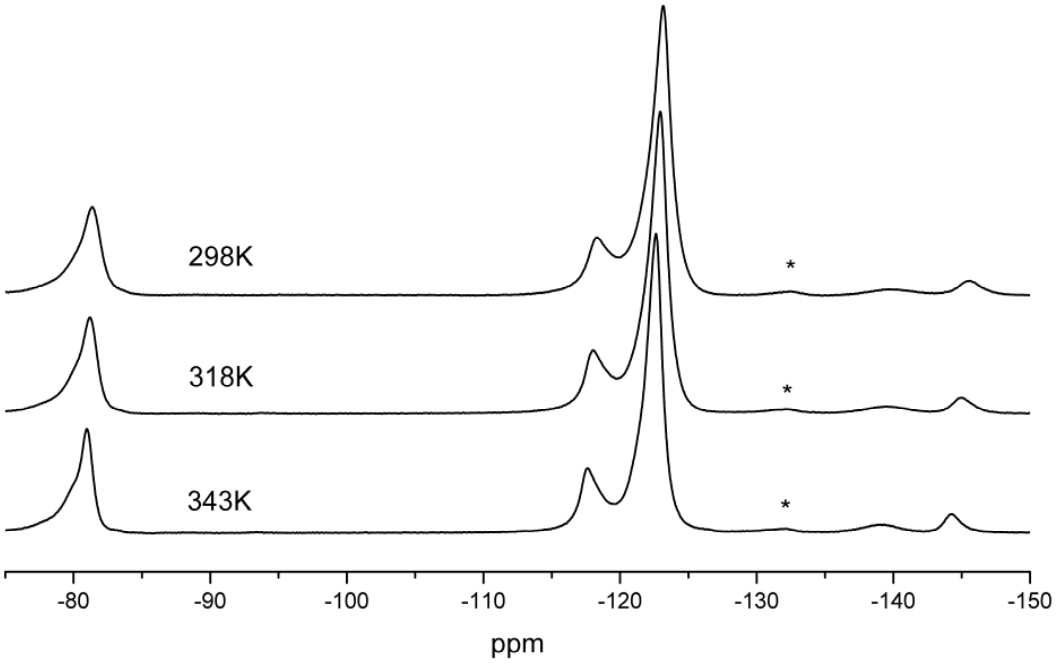

Figure 4.17: Stacked plot of ^{19}F MAS NMR spectra of a rolled Nafion cast membrane kept at different temperatures during acquisition. Spectra taken at 470 MHz, spinning at 24 kHz.

The effect of an increase of sample temperature on the ^{19}F spectrum of a rolled membrane is shown in Figure 4.17. Two spectral trends with increasing temperature emerge. Firstly all resonances narrow including those assigned to the backbone which is consistent with increasing mobility throughout the ionomer, as would be expected at higher temperature. Secondly, the entire spectrum is shifted to higher chemical shifts, indicating overall reduced shielding throughout the molecule. The most likely explanation for a reduction in general electron shielding in the solid is a reduction in density. No such shift changes are observed with swelling with water absorption so this change with temperature must be of a different nature.

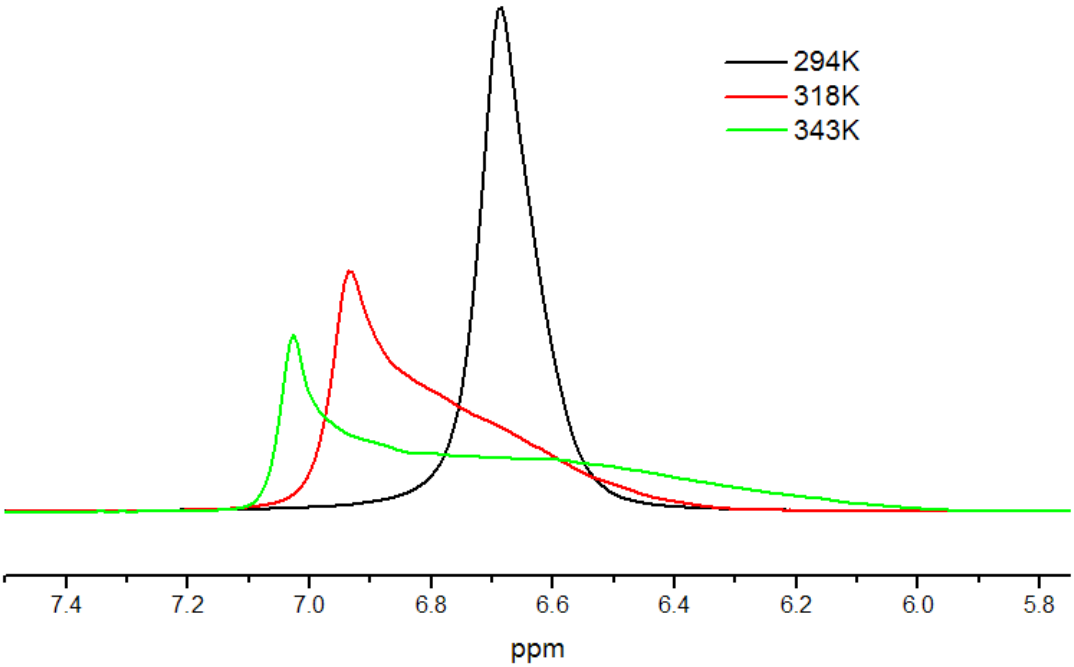

Figure 4.18: Overlaid plot of ^{1}H MAS NMR spectra of water in a rolled Nafion cast membrane kept at different temperatures during acquisition. Spectra taken at 500 MHz, spinning at 12.5 kHz.

Figure 4.18 shows the changes in the ^{1}H spectrum over the same temperature range. The lineshapes found at elevated temperatures are unlike any observed previously, it is most likely that it arises from a distribution of temperature, hydration or both through the membrane. The samples were kept at temperature for 15 minutes before acquisition which did not lead to a narrower line so it is possible that the equipment cannot produce a perfectly consistent temperature and level of hydration through the material by the application of heated gas to the exterior of the rotor. This makes any analysis of structure or dynamics from the spectrum impossible.

With preparation and temperature effects considered and isolated a comparison of the differing casting methods can be made. While figure 4.19 shows differences in peak widths they are not nearly as divergent as those in figure 4.10 (grated samples).

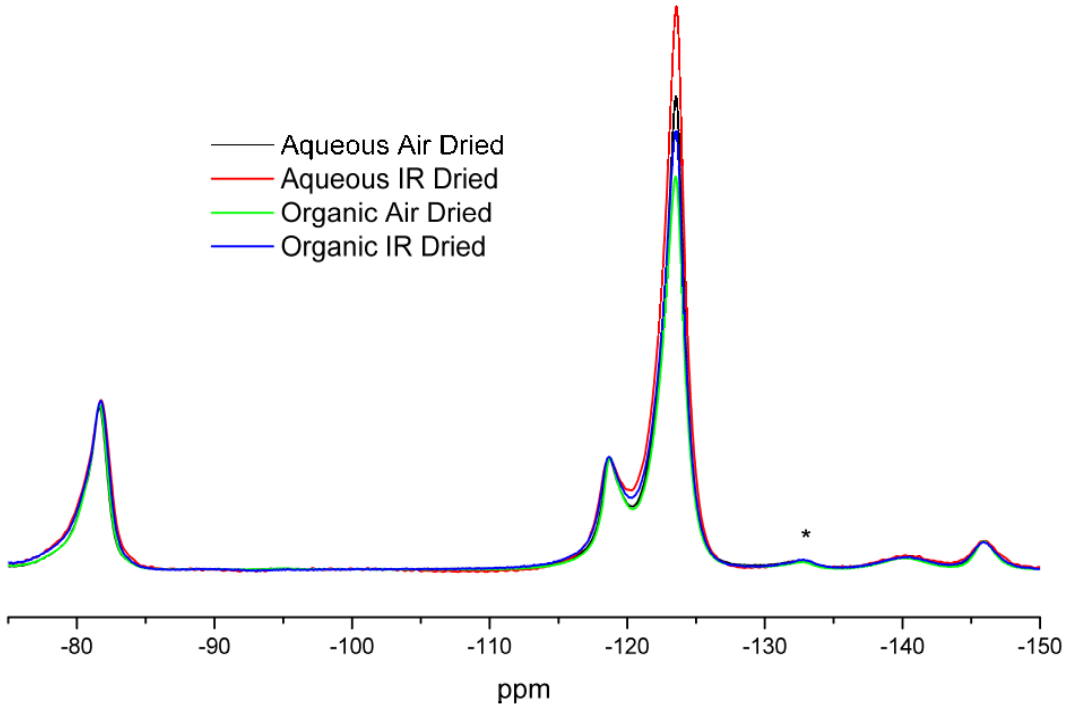

Figure 4.19: Overlaid plot of ^{19}F MAS NMR spectra of rolled Nafion cast membranes stored at 100% RH at standard temperature and pressure before packing. The temperature of the samples was regulated at 294K. All spectra taken at 470 MHz, spinning at 24 kHz. Spectra normalized to intensity of sidechain peaks

The samples were heated and compared at a higher temperature in figure 4.20 in order to see if larger differences emerged between the membranes with the improved resolution brought by higher temperatures and thus higher mobilities. As in figure 4.19 the air dried membranes produce almost identical spectra while the IR dried membranes seem more similar at elevated temperatures than at room temperature. Combined with an inability to use the ^{1}H NMR at elevated temperatures for material analysis due to the effect of temperature gradients across the sample, all remaining experiments were conducted at room temperature. Before attributing any differences in peak widths in figures 4.19 and 4.20 as being caused by casting methods the ^{1}H NMR at room temperature must be considered.

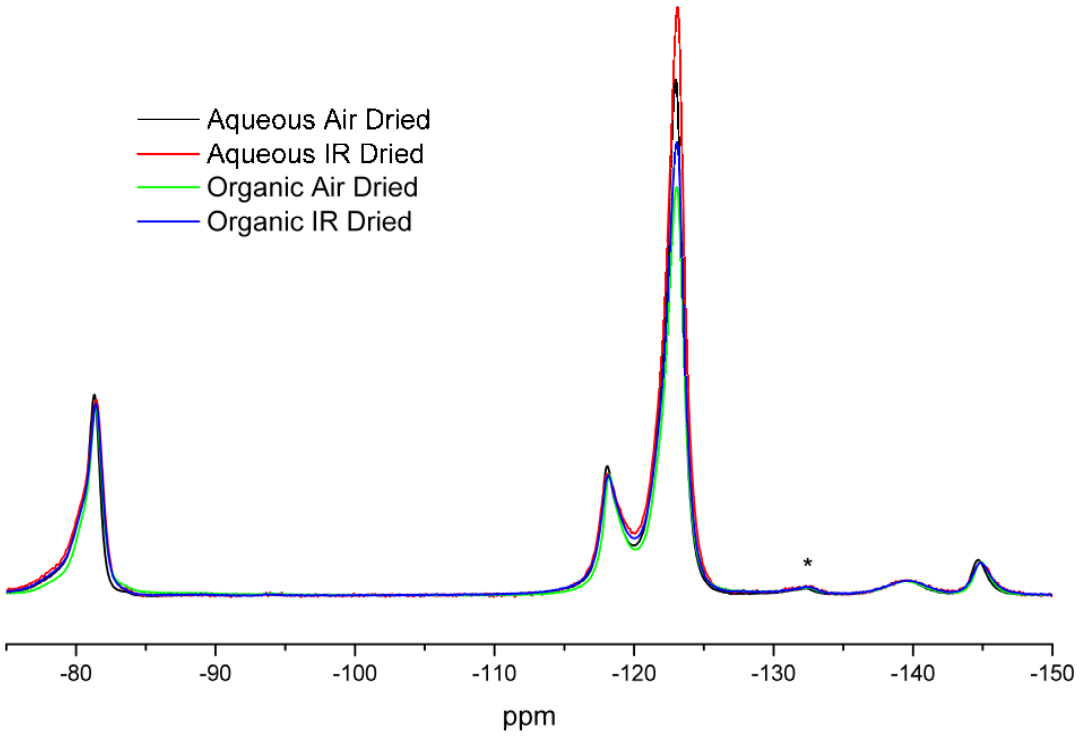

Figure 4.20: Overlaid plot of ^{19}F MAS NMR spectra of rolled Nafion cast membranes stored at 100% RH at standard temperature and pressure before packing. The temperature of the samples was regulated at 343K. All spectra taken at 470 MHz, spinning at 24 kHz. Spectra normalized to intensity of sidechain peaks

Both the position and width of the water peaks vary greatly. Firstly, the position of the peaks and thus the water content of the membranes inversely correlate with the peak widths observed in figures 4.19 and 4.20. Therefore, no conclusions about membrane structure and dynamics beyond water uptake can be made from those spectra as water content has been shown to have a strong effect on ionomer mobility. Table 4.6 shows that the water peak width is dependent upon both casting solvent and drying method. However, before drawing conclusions from this data it is important to isolate and control the water content to remove it as a factor in comparing these membranes. This is achieved by drying the membranes at 0% RH after packing. Figure 4.22 and 4.23 show the ^{19}F and ^{1}H NMR spectra of these dried rolled membranes.

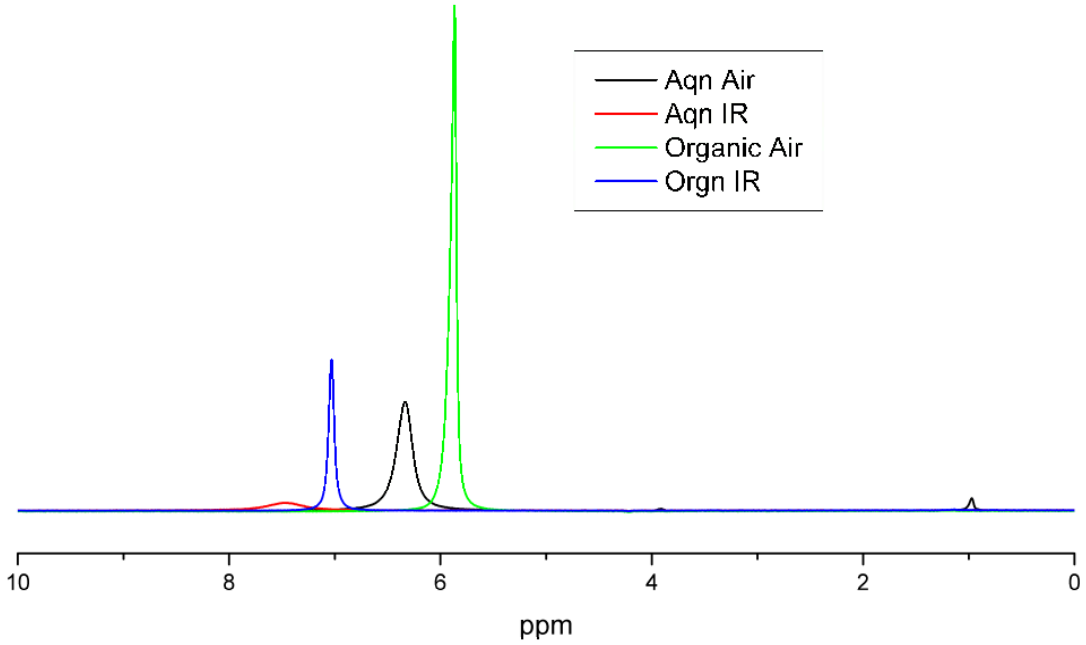

Figure 4.21: Overlaid plot of ^{1}H MAS NMR spectra of water in rolled Nafion cast membranes stored at 100% RH at standard temperature and pressure before packing. The temperature of the samples was regulated at 318K. All spectra taken at 500 MHz, spinning at 12.5 kHz.

Membrane	^{1}H NMR Lineshape Position ± 0.005 ppm	^{1}H NMR Lineshape Width ± 0.01 ppm
Aqueous Air Dried	6.33	0.17
Aqueous IR Dried	7.47	0.43
Organic Air Dried	5.87	0.06
Organic IR Dried	7.03	0.06

Table 4.6: ^{1}H NMR linewidths of rolled cast membranes stored at 100% RH at standard temperature and pressure before packing.

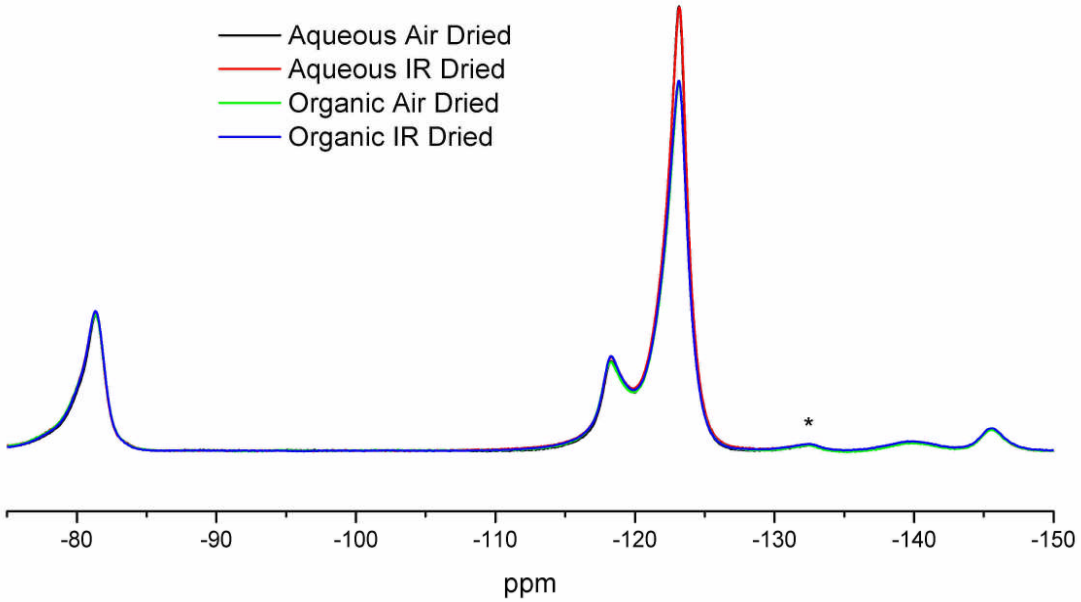

Figure 4.22: Overlaid plot of ^{19}F MAS NMR spectra of rolled Nafion cast membranes stored at 0% RH at standard temperature and pressure after packing. All spectra taken at 470 MHz, spinning at 24 kHz. Spectra normalized to intensity of sidechain peaks.

With nearly identical water content the ^{19}F spectra of the membranes differ only in the backbone resonance intensity which is dependent upon equivalent weight. Other than indicating relative water uptake it would appear that ^{19}F solid-state NMR cannot detect any differences in the membrane due to casting method.

The peak positions of the ^{1}H water peaks now vary by only hundredths of a ppm confirming that there is little difference in the overall water content of the membranes. Differences in the peak widths persist however and are recorded in table 4.7 below.

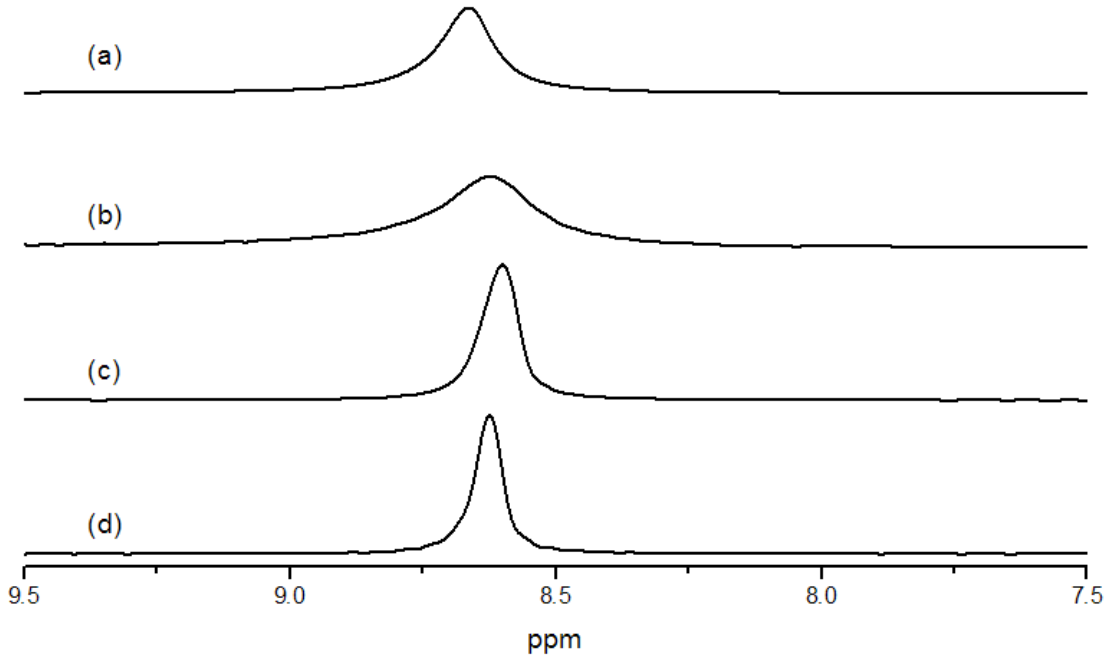

Figure 4.23: Stacked plot of ^{1}H MAS NMR spectra of water in rolled Nafion cast membranes stored at 0% RH at standard temperature and pressure before packing. The temperature of the samples was regulated at 318K. The membranes were cast and dried as follows; (a) aqueous solvent air dried, (b) aqueous solvent IR dried, (c) organic solvent air dried, (d) organic solvent IR dried. All spectra taken at 500 MHz, spinning at 12.5 kHz.

Membrane	^{1}H NMR Lineshape Position ± 0.005 ppm	^{1}H NMR Lineshape Width ± 0.01 ppm
Aqueous Air Dried	8.66	0.12
Aqueous IR Dried	8.62	0.22
Organic Air Dried	8.60	0.08
Organic IR Dried	8.62	0.06

Table 4.7: ^{1}H NMR linewidths of rolled cast membranes stored at 0% RH at standard temperature and pressure before packing.

It is clear that the differences in linewidths are related to the method by which the membrane is cast and not just its water content. Before these differences are explored it must be established what the linewidth of these spectra represent. The position of the ^{1}H NMR peak of water within an ionomer is dependent upon the ratio of water molecules that are hydrogen bonded with an acid group and those that are not. The chemical shift of the peak observed is in fact a weighted average of the peak positions of water associated with the acid groups and water that is not. The averaging is caused by exchange between the two states on a timescale faster than the NMR experiments in at least one direction. It is a similar effect as seen when the shifts of two species that can exchange through a set of reversible reactions are averaged. Therefore the water chemical shift is a measure of the ratio of water molecule to acid groups in the water network of the ionomer. If the increased linewidths observed in figures 4.21 and 4.23 were due to residual broadening from interactions between the nuclear spins and those of surrounding spins then we would expect them to be sensitive to MAS speed which is not the case. The presence of non-Gaussian distributions in the case of the air dried membranes is further reason to reject this explanation. It is therefore suggested that the linewidths are in fact distributions of water environment ratios within the ionomer. A membrane with a large linewidth has a wide distribution of water to acid ratios in localities (micelles or channels) in the water network while a membrane with a narrower linewidth has a far more homogeneous water distribution throughout the material.

With this established it is possible to consider the effects that different casting methods have on Nafion membranes. Membranes cast from aqueous solution have a much greater degree of inhomogeneity in the water to acid ratio than those cast from organic solution. The fact that relatively water rich and water poor localities exist suggest that either the connectivity of the water network is lower in aqueous membranes or that the solid forms with these inequalities and the diffusive processes are insufficient to equalise them once cast and dried. The rapidly dried aqueous membrane has a considerably wider peak than the air dried membrane in both wet and dry conditions, while IR drying appears to have little effect or slightly narrow the water peak of the membrane when cast from organic solution. IR drying appears to have different effects on the aqueous and organic membranes, making the structure of a membrane from aqueous solution less homogeneous and an organic membrane more

homogeneous. Whatever the cause of the inhomogeneity IR drying does not appear to make the aqueous membrane more like the structure of the organic, but rather less like it.

4.3.3 ^{19}F-^{13}C NMR of Cast Nafion Membranes

While most of the NMR properties of the ^{13}C nucleus are not as favourable as those of the ^{1}H and ^{19}F nuclei it is advantageous to study as many nuclei in the Nafion molecule as possible so as to acquire as complete an understanding of its structure and dynamics as can be determined from solid-state NMR. Signal-to-noise is the key limiting factor to ^{13}C NMR at natural abundance so the grating method was chosen for the first ^{13}C Cross-Polarisation (CP) experiments as it allows for a greater mass of sample in the rotor. Figure 6.24 shows the ^{19}F-^{13}C CP spectra of all four cast Nafion membranes that have been hydrated at 100% RH. Assignment of the ^{13}C spectrum of Nafion [49] is very similar to ^{19}F spectra with a backbone CF_2 peak dominating and the sidechain resonances positioned relative to it and one another in the same manner. The OCF_2 and CF_3 peaks are at the higher end of the chemical shift range at 118.5 and 117.7 ppm respectively. The SCF_2 peak, although not resolved from the backbone peak without the use of filtering as employed in [46], is found at a slightly higher shift than the backbone CF_2 chain centred at 111.8 ppm. The CF resonances are found at lower shifts, the branch point peak at 108.5 ppm and the sidechain CF at 103.6 ppm. Comparing the spectra there is no sign of peak position changes within the sample set and the only trend observable in the peak widths is that the aqueous air dried and organic IR dried samples have narrower backbone and sidechain peaks than the other two membranes which are comparable. Without variable MAS or T_2 measurements it cannot be confirmed that this variation is caused by higher carbon mobility or greater disorder. The peak width variations across the sample set are not consistent with the ^{19}F spectra of the same samples prepared in the same manner in figure 4.10. However, the effect of water content on NMR spectra of these materials cannot be underestimated and it could well be the case that the water content of samples were not consistent across and within the two series of experiments. It would appear that ^{13}C NMR, like ^{1}H and ^{19}F NMR, is also sensitive to the dynamic changes of the Nafion molecule. However, its usefulness as a technique for comparing membranes in the same state as found in operating fuel cells is limited by its sensitivity. ^{19}F-^{13}C CP

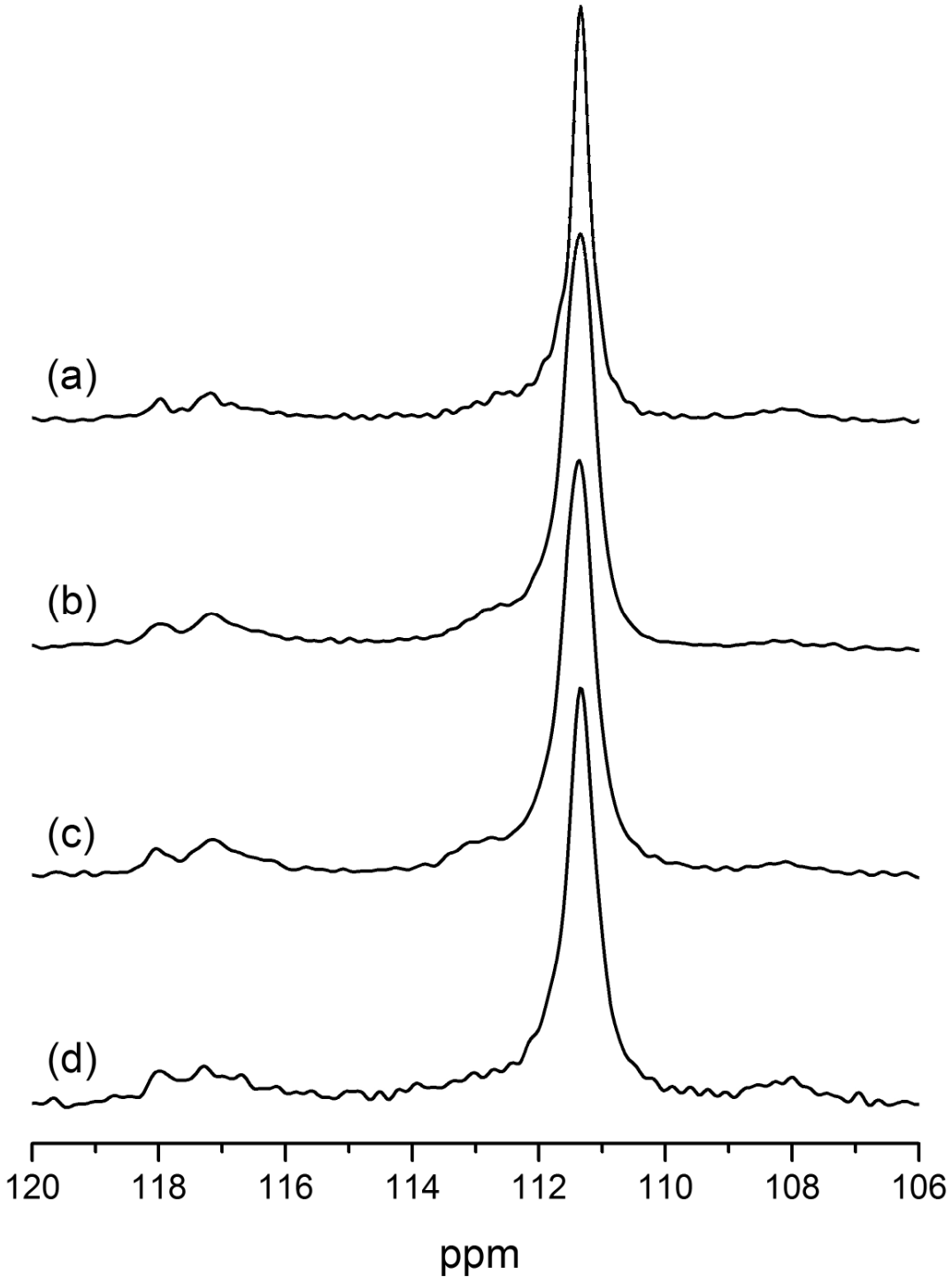

Figure 4.24: Stacked plot of ^{19}F-^{13}C CP MAS NMR spectra of grated Nafion cast membranes stored at 100% RH at standard temperature and pressure before packing. The membranes were cast and dried as follows; (a) aqueous solvent air dried, (b) aqueous solvent IR dried, (c) organic solvent air dried, (d) organic solvent IR dried. All spectra taken at 75.5 MHz, spinning at 28 kHz.

NMR was also attempted on rolled Nafion samples, but the reduced mass of sample (2 mg rather than 20 mg) meant the timescale required for appropriate signal-to-noise was unrealistic.

4.4 ^{19}F and ^{1}H NMR of the Ionomer Component of Dried Nafion Inks

While sections 4.2 and 4.3 studied Nafion and other ionomers in their bulk state as it would be prepared as a fuel cell electrolyte, this is not the only form of ionomer present in an MEA. As described in Section 1.1.3 it is necessary for reactants and both positive and negative charges to be transported to and from the point of oxidation or reduction, the platinum surface. While the low density, high surface area platinum nanoparticles supported on a graphitic aggregate allows both gas access and provides electron conductivity, a proton conduction route to and from the metal surface is required. This is achieved by a thin coating of proton exchange ionomer applied to the catalyst surface, around a single molecule thick. This layer ensures conductive contact between catalyst and electrolyte and is a vital part of the fuel cell.

Although the material to be studied was a mono-molecular surface layer the high receptivity of both the ^{1}H and ^{19}F nuclei ensured acceptable signal-to-noise within several minutes in the case of ^{19}F and an hour for ^{1}H NMR. The ^{19}F MAS NMR spectra of the catalyst ink powders kept in a hydrated state are shown below in figure 4.25.

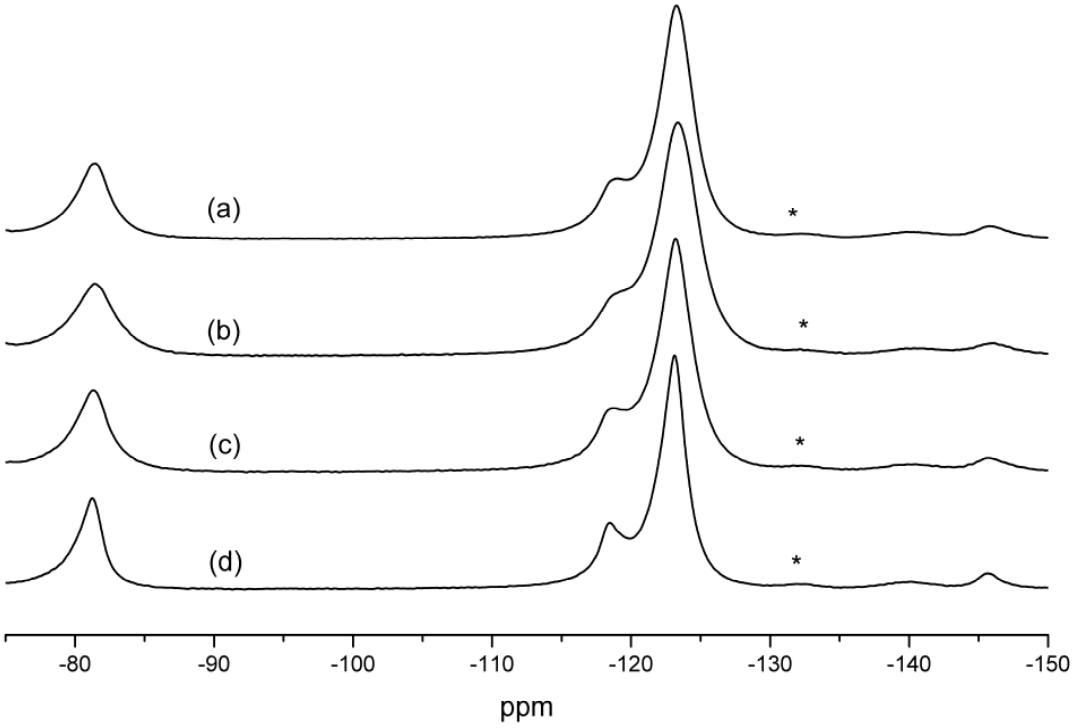

Figure 4.25: Stacked plot of ^{19}F MAS NMR spectra of fuel cell catalyst inks stored at 100% RH at standard temperature and pressure before packing. The solvents and ionomer loadings were as follows: (a) aqueous solvent carbon ratio of 80, (b) aqueous solvent carbon ratio of 120, (c) organic solvent, carbon ratio of 80, (d) organic solvent, carbon ratio of 120. All spectra taken at 470 MHz, spinning at 24 kHz.

It is immediately apparent from the universally wider peaks that the entire ionomer molecule is less mobile or ordered in the form of a catalyst coating than it is as a bulk membrane. The spectra look more like those of the grated membranes studied in section 4.3.1. Peak positions and relative intensities are unchanged within error with respect to the bulk Nafion studied in section 4.3. At an ionomer loading of 80 to 100 carbons of catalyst support the aqueous and organic cast inks are indistinguishable from one another. However at the higher 120 loading, at which point the ionomer layer will be multiple molecular layers thick, the organic ink becomes more ‘bulk-like’ while the aqueous ink becomes less ‘bulk-like’. It should be noted that none of the inks appear polyphasic in ^{19}F NMR, so any interaction between the ionomer and catalyst surface unique to the closest layer to the surface is not detectable. The data in figure 4.25 does suggest that the addition of extra ionomer

alters the conformation of the layer in different ways dependent upon the solution in which it is formed. The ^{1}H MAS NMR spectra shown in figure 4.26 shed additional light on these conformational differences.

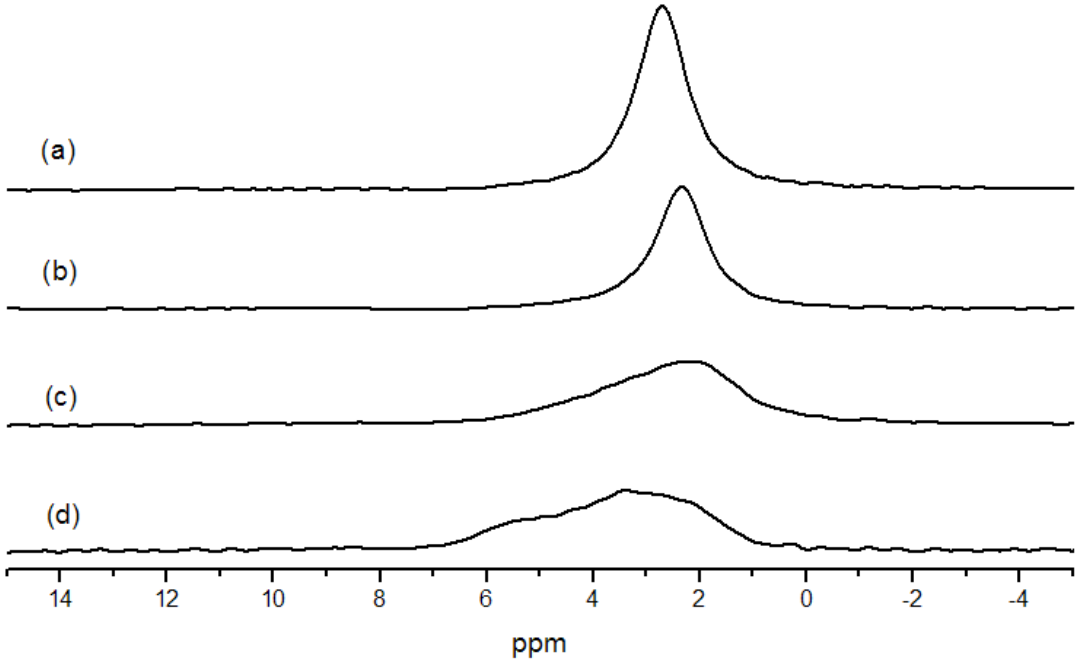

Figure 4.26: Stacked plot of ^{1}H MAS NMR spectra of water in fuel cell catalyst inks stored at 100% RH at standard temperature and pressure before packing. The solvents and ionomer loadings were as follows: (a) aqueous solvent carbon ratio of 80, (b) aqueous solvent carbon ratio of 120, (c) organic solvent, carbon ratio of 80, (d) organic solvent, carbon ratio of 120. All spectra taken at 500 MHz, spinning at 24 kHz.

Unlike the ^{1}H spectra of all bulk ionomers and membranes much of the signal is found at chemical shifts below 4.5 ppm, the position of bulk water. If the chemical shift is not a weighted average between 4.5 ppm and a highly hydrogen bonded resonance at around 11 ppm then the water cannot be exchanging between a bulk-like water and acid associated hydrogen bonded states. Instead majority of the water peaks are centred < 3 ppm and are significantly broader. There are similarities with water bound in a low dimensional state such as the surface of a hydrophobic material [114]. However, the large differences between the spectra are indicative of the water being associated with the ionomer in different ways rather than just collected on the surface of the catalyst ink. It is proposed that water resonances < 4.5 ppm should be attributed to water that is not associated with the sulphonic acid groups in the same way as in bulk Nafion.

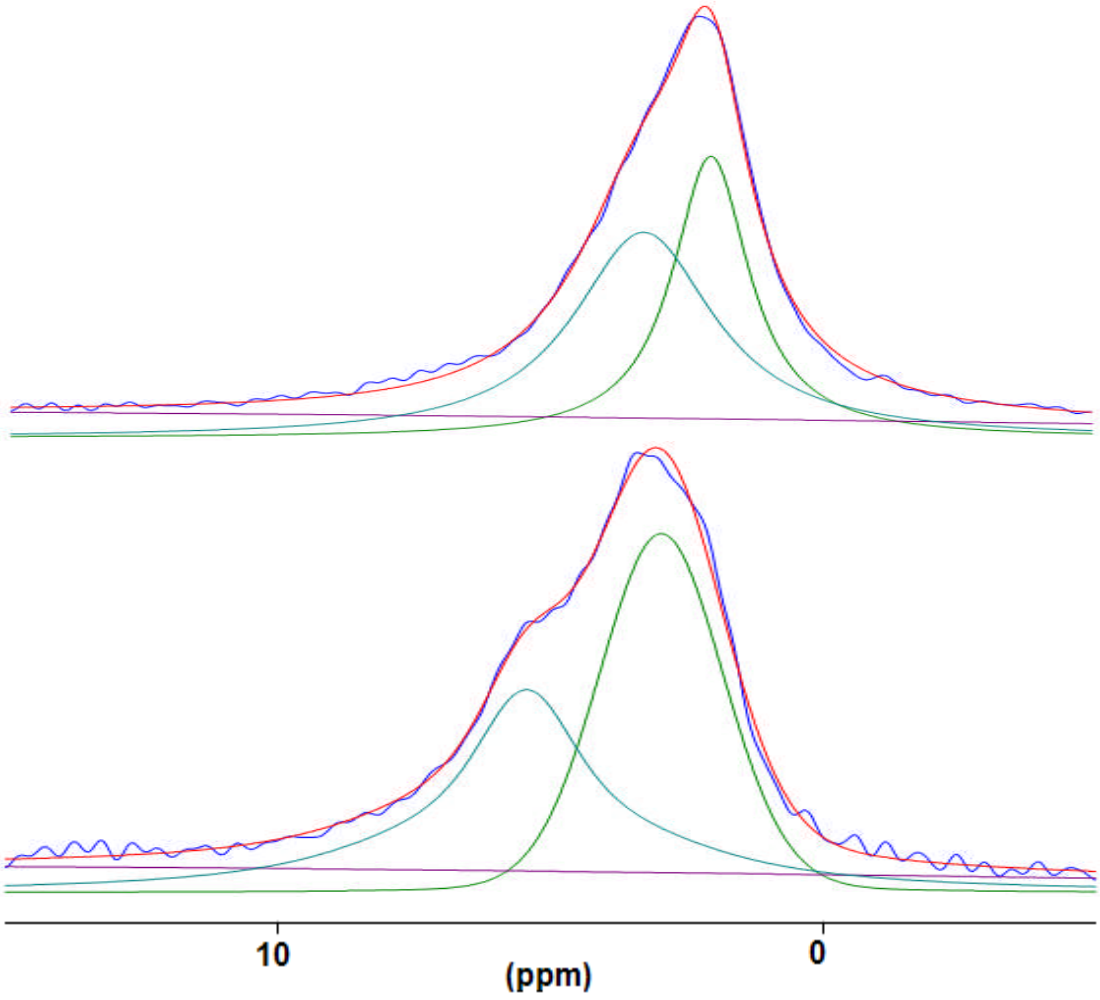

Figure 4.27: ^{1}H deconvoluted spectra of the ^{1}H MAS NMR spectra of water in fuel cell catalyst inks stored at 100% RH at standard temperature and pressure before packing. (a) organic ink with an ionomer carbon ratio of 80, (b) organic ink with an ionomer carbon ratio of 120. Spectra taken at 500 MHz, spinning at 24 kHz.

Spectra (a) and (b) appear to contain water exclusively in a non-bulk environment, excluding the possibility of water micelle or nanotube formation. It is necessary to deconvolute spectra (c) and (d) as they cannot be fit to a single symmetrical line and these deconvolutions are shown in figure 4.27. Both spectra can be modelled with acceptable accuracy with just two peaks, the third broad line seen (purple) is the peak representing the equipment background and as such is not relevant to the analysis.

Ink	Peak 1		Peak 2	
	Position ±0.05 ppm	Width ± 0.05 ppm	Position ± 0.05 ppm	Width ± 0.05 ppm
Aqueous 80	2.71	1.11	-	-
Aqueous 120	2.35	1.12	-	-
Organic 80	2.05	1.72	3.29	3.17
Organic 120	2.97	2.69	5.44	3.02

Table 4.8: Peak positions and widths from the deconvolutions of the spectra in figure 4.26-28.

Table 4.8 is a summary of the data from the deconvolutions shown in figures 4.27 and 4.28 and also from spectra (a) and (b) in figure 4.26. The modelled peaks positions show that the Organic 120 ink is the only one to contain a detectable amount of its water at a chemical shift consistent with a water network interacting with the sulphonic acid groups. It is noteworthy that the average shift of the water peaks of an ink is negatively correlated with ^{19}F peak widths. A water shift below bulk water and an immobile ionomer point to a configuration of Nafion that is unrelated to the micelle or nanotube water network models proposed for the bulk material.

Figures 4.29 and 4.30 show ^{19}F and ^{1}H NMR of catalyst inks dried at 0% RH.

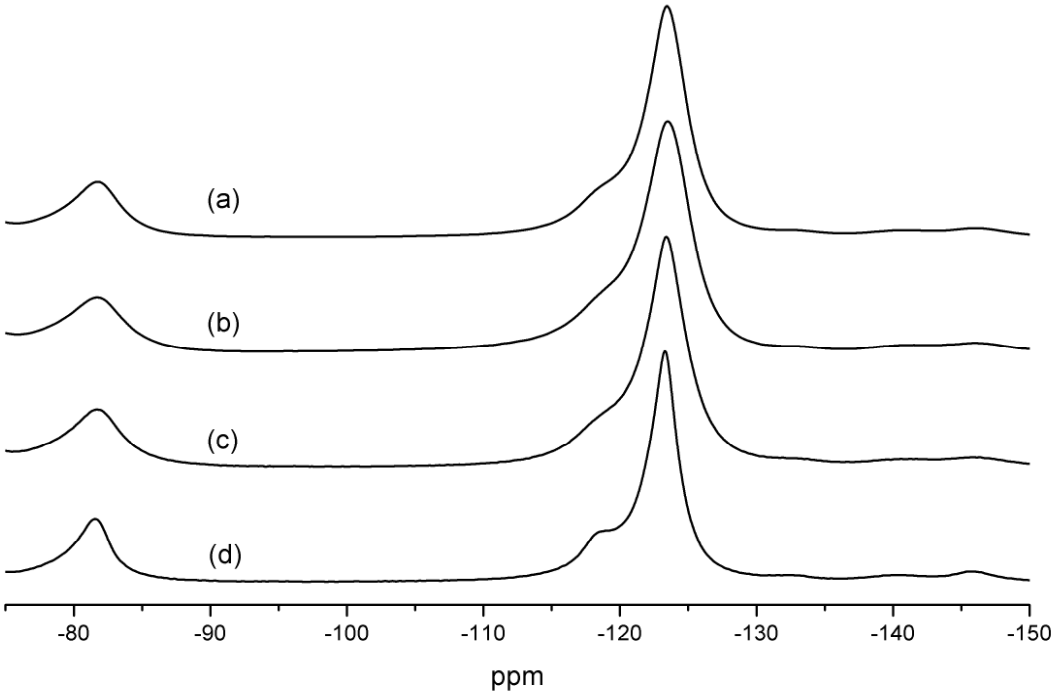

Figure 4.29: Stacked plot of ^{19}F MAS NMR spectra of fuel cell catalyst inks stored at 0% RH at standard temperature and pressure after packing. The solvents and ionomer loadings were as follows: (a) aqueous solvent carbon ratio of 80, (b) aqueous solvent carbon ratio of 120, (c) organic solvent, carbon ratio of 80, (d) organic solvent, carbon ratio of 120. All spectra taken at 470 MHz, spinning at 24 kHz.

Figure 4.29 shows that at low water content the same peak width patterns observed in the hydrated ink are maintained. The 80 carbon inks are once again indistinguishable by ^{19}F NMR, the aqueous 120 ink is broader and the organic 120 ink narrower. This confirms that the linewidth differences were not the result of differential water content.

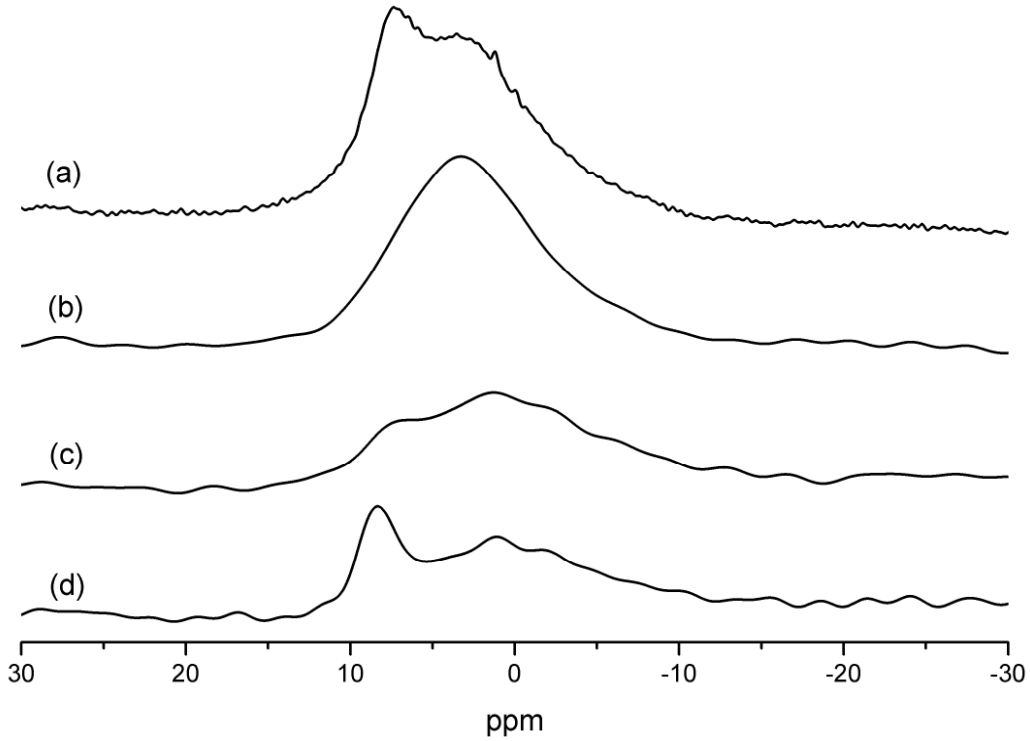

Figure 4.30: Stacked plot of ^{1}H MAS NMR spectra of water in fuel cell catalyst inks stored at 0% RH at standard temperature and pressure after packing. The solvents and ionomer loadings were as follows: (a) aqueous solvent carbon ratio of 80, (b) aqueous solvent carbon ratio of 120, (c) organic solvent, carbon ratio of 80, (d) organic solvent, carbon ratio of 120. All spectra taken at 500 MHz, spinning at 12.5 kHz.

There are two key differences between figures 4.26 and 4.30, firstly the width of the lineshapes is much greater in figure 4.30, around 10 ppm compared to a maximum of 5 ppm. Secondly, spectra (a) and (d) show narrower peaks centred about 5 ppm that suggest a proportion of the water is associated with acid groups. Once again these spectra must be deconvoluted for analysis, figures 4.31 and 4.32 show the multiple-peak deconvolutions of spectra (a) and (d) and table 4.9 summarises all the data.

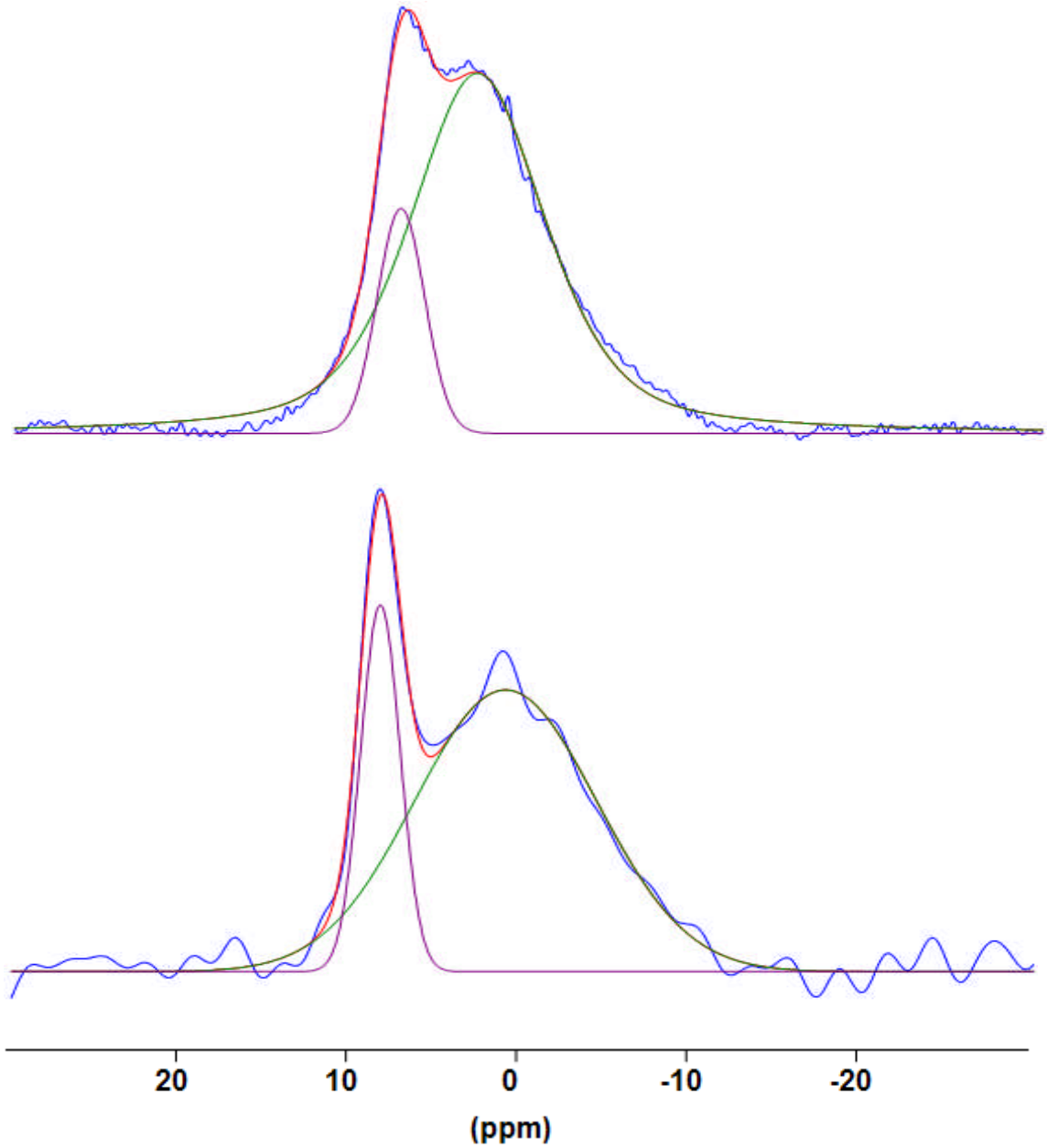

Figure 4.31: ^{1}H deconvoluted spectra of ^{1}H MAS NMR spectra of water in fuel cell catalyst inks stored at 0% RH at standard temperature and pressure before packing. (a) aqueous ink with an ionomer carbon ratio of 80, (b) organic ink with an ionomer carbon ratio of 120. Spectra taken at 500 MHz, spinning at 12.5 kHz.

While all the inks were hydrated, only the organic 120 ink showed clear evidence of an acid-water network but as figure 4.31 shows in the dry state 15% of the signal of the aqueous 80 ink is in a peak centred at 7.46 ppm and therefore could correspond to water in a micelle or nanotube. In the organic 120 ink the peak assigned to water associated with acid groups makes up 22% of the signal while the organic 80

ink may also contain water-acid environments but better signal-to-noise is required to be confident.

Ink	Peak 1		Peak 2	
	Position ± 0.05 ppm	Width ± 0.05 ppm	Position ± 0.05 ppm	Width ± 0.05 ppm
Aqueous 80	2.99	9.31	7.46	3.26
Aqueous 120	3.11	10.00	-	-
Organic 80	1.29	13.03	-	-
Organic 120	0.98	12.58	8.33	2.73

Table 4.9: Peak positions and widths from the deconvolutions of the spectra in figure 4.30-31.

In all four spectra a majority of the proton signal is not associated with water exchanging with the acid groups and may not be water protons at all. The larger width and much reduced intensity of these peaks in the dry condition allow the possibility that the signal comes from protons in the carbon support. Higher spinning speeds had an effect of narrowing the spectra so it is reasonable to suppose that hetero- or homonuclear dipolar coupling is broadening these peaks.

4.5 Undesirable effects of MAS on NMR Spectra of Ionomers

Although fewer spinning sidebands are observed in the ^{19}F spectra of rolled membranes than in those of grated membranes their presence suggests that interactions are not yet fully averaged and lineshapes may be narrower at higher spinning speeds. Figure 4.38 shows the overlaid spectra of the same cast membrane acquired at three different MAS speeds.

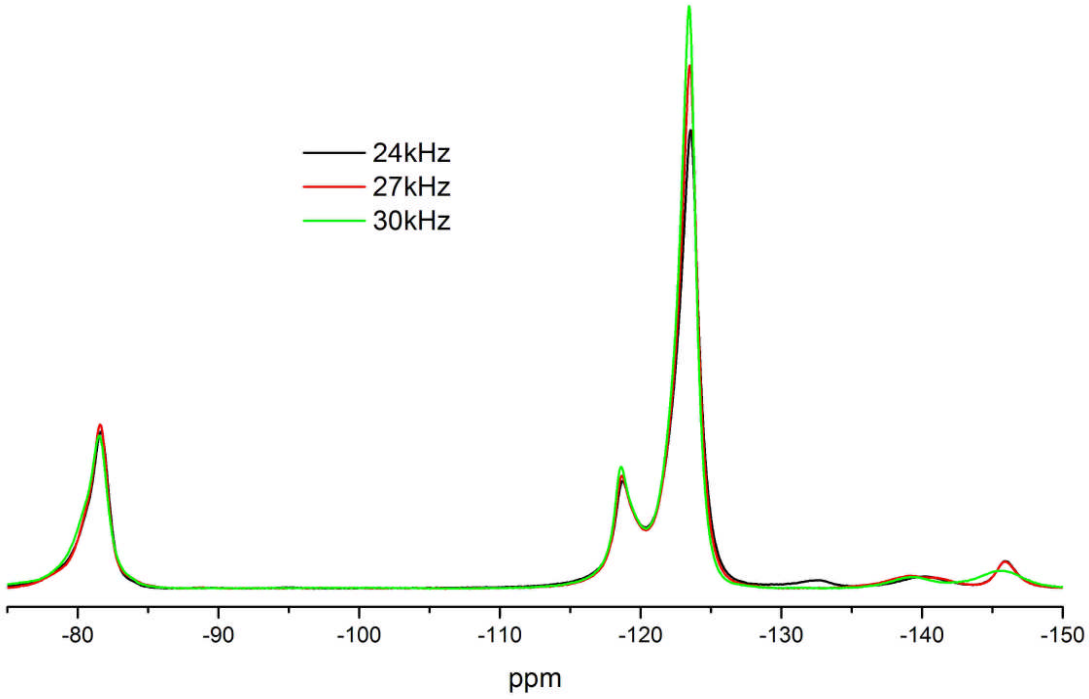

Figure 4.32 Overlaid plot of ^{19}F MAS NMR spectra at three different MAS speeds of rolled Nafion membrane cast from water and air dried, stored at 100% RH at standard temperature and pressure before packing. All spectra taken at 470 MHz.

It is immediately clear that at 24 kHz, the chosen spinning speed for a majority of the ^{19}F NMR in this chapter, the interactions causing broadening in the lineshape are not being entirely averaged by the magic angle spinning as higher spinning speeds result in narrower peaks. This is valuable information for these samples as it tells us that differences in the widths of peaks are due to the size or the dynamic averaging of interactions dependent upon $(3\cos^2\theta-1)$. If the differences were entirely due to static disorder in the system we would see no such width variation at different spinning speeds.

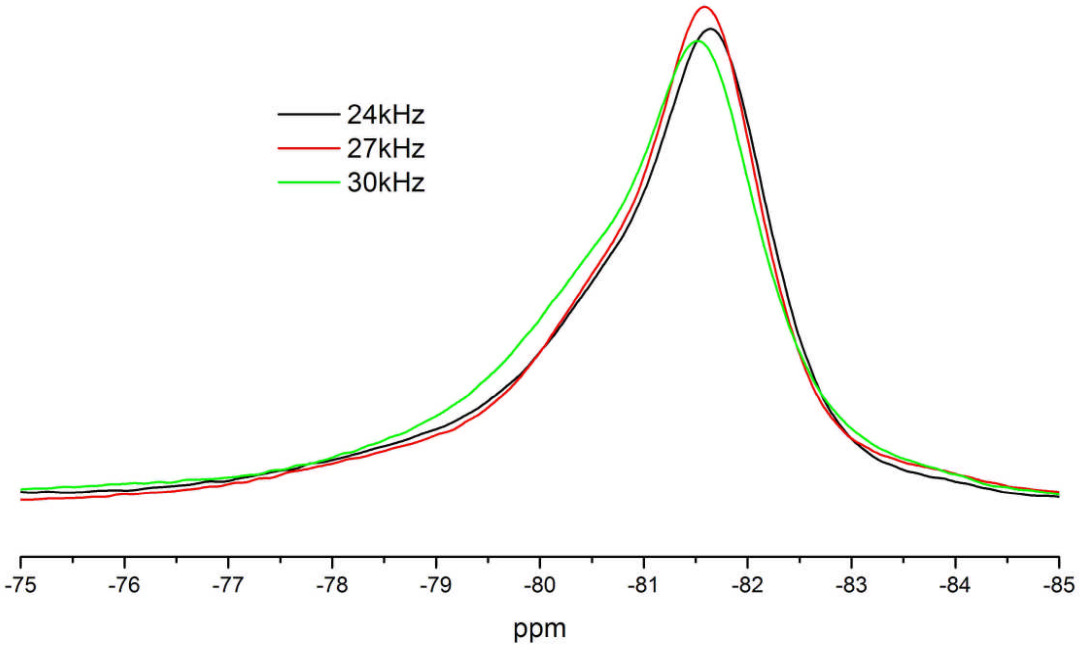

Figure 4.34: Overlaid plot of a section of ^{19}F spectra at three different MAS speeds of rolled Nafion membrane cast from water and air dried, stored at 100% RH at standard temperature and pressure before packing. Samples were kept at 25°C by variable temperature control. All spectra taken at 470 MHz.

The way that the main spectral features vary, narrowing by faster spinning is also of note. While the differences between the 24 kHz and 27kHz spectra are clearly a result of the narrowing of at least one of the three peaks that make up this spectral feature, there is an apparent shift in the position of the peaks to higher chemical shift when the sample is spun to 30kHz. The peaks also seem to have broadened when compared to those observed at 27 kHz. This is evidence of a morphological change in the ionomer due to spinning at speeds close to the maximum specified by the probe manufacturer. As the temperature of the rotor is being controlled within ± 0.05°C this change must be a result of the pressure the sample is under during spinning.

Additional evidence for a change in the way the ionomer molecules are ordered at high spinning speeds is found in high speed MAS spectra ^{1}H of the same membranes.

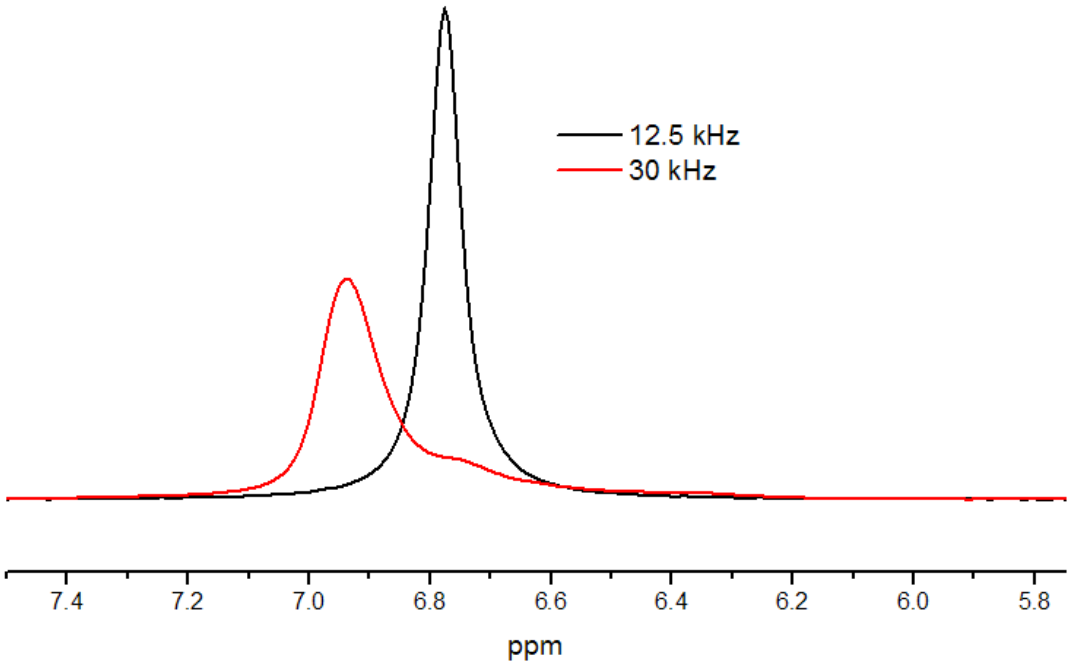

Figure 4.35: Overlaid plot of ^{1}H MAS NMR spectra at two different MAS speeds of water in a rolled Nafion membrane cast from water and air dried, stored at 100% RH at standard temperature and pressure before packing. Samples were kept at 25°C by variable temperature control. All spectra taken at 500 MHz.

At low spinning speeds (6-27 kHz) a single peak at is observed, this is the standard water peak observed in perfluorosulphonic ionomers. However, under 30 kHz MAS the water appears as at least two peaks shifted upfield. The deconvolutions of the spectra shown in figure 4.35 are displayed below.

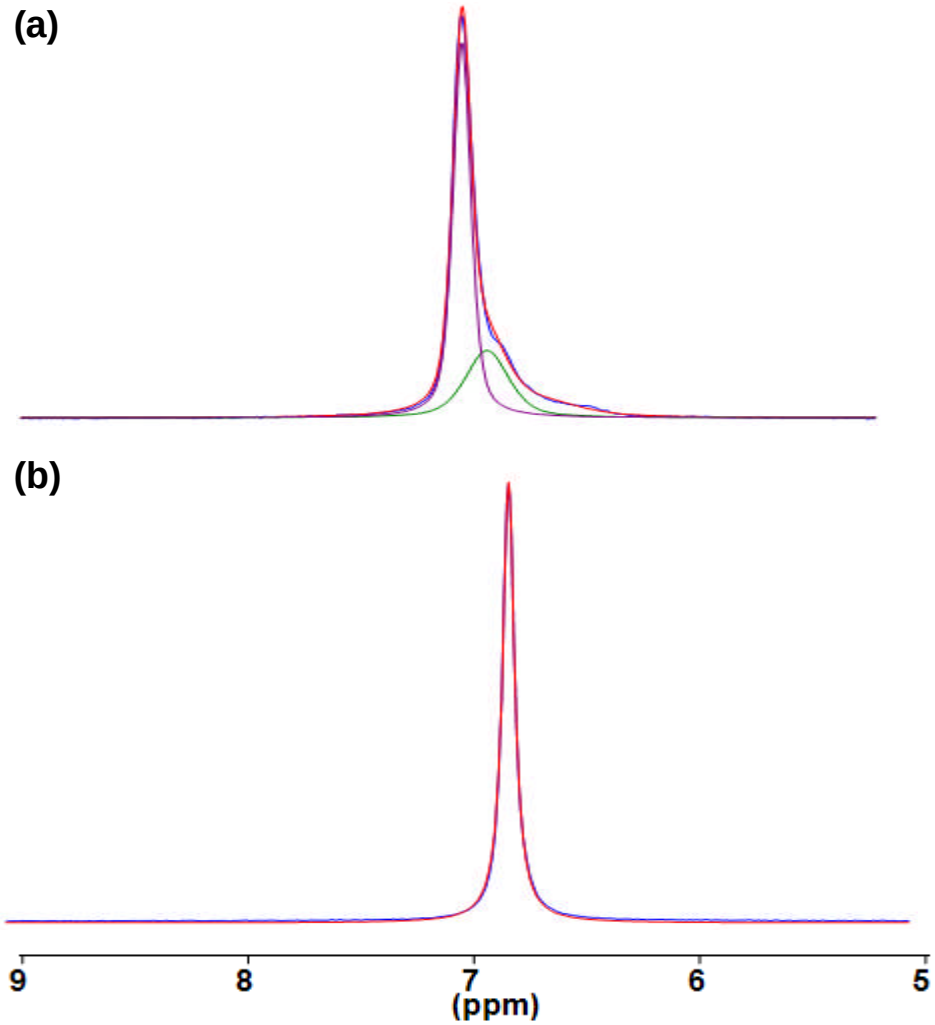

Figure 4.36: Deconvolution of ^{1}H MAS NMR spectra of water in a rolled Nafion membrane cast from water and air dried, stored at 100% RH at standard temperature and pressure before packing. (a) spinning at 30kHz (b) spinning at 12.5 kHz. Samples were kept at 25°C by variable temperature control. Spectra taken at 470 MHz.

Position ± 0.01 ppm	12.5 kHz		30kHz	
	Int %	Width ± 0.01 ppm	Int %	Width 0.01 ppm
6.50	-	-	8	0.40
6.78	100	0.06	27	0.24
6.94	-	-	65	0.10

Table 4.10: Deconvolution data for the fits of figure 4.36. Intensities are calculated by DMfit and given as a percentage of the total intensity of the fit (not the raw data) to the nearest percent). Widths, also given by DMfit are FWHM in ppm.

Changes in line shape that are observed with increasing MAS speed cannot be explained as the spinning out of broadening interactions. The assertion that high speed MAS causes an alteration of the environment of the water protons within the sample is supported by changes in the ^{19}F and ^{1}H chemical shift. MAS subjects the sample to temperature changes and high pressures. Common experience shows that the pressure on the sample during MAS will not have a noticeable effect on the spectrum assuming standard packing conditions. That is, if the sample consists of closely packed spherical particles that do not deform under the pressures experienced. In this case any structural changes in the sample are confined to areas of contact between the particles which make up a very small proportion of the total volume and therefore no spectral changes are observable. However, the ionomers studied cannot be prepared and packed in this manner and matters are complicated by the presence of a liquid phase within the sample. Additionally, it is known that pH variation can have a significant effect on the ^{1}H spectrum of bulk water[15].

4.6 Conclusions

In this chapter ^{1}H, ^{19}F and ^{19}F-^{13}C CP MAS NMR have been applied to a range of materials suitable for use in PEMFCS and which contain perfluorosulphonic ionomers. These include a range of commercial or experimental ionomer samples, Nafion cast membranes and dried catalyst inks, each of which will be considered in turn.

It was shown that the ^{19}F MAS NMR spectra of short chain Solvay ionomers is insensitive to EW changes even though this technique has been shown to detect the sidechain mobility changes caused by variations in temperature and water content. It is therefore proposed that any effect that the distance between sidechain has on their mobility or interactions is significantly smaller than the effect of changes to these environmental conditions. The same studies revealed that the sidechain structure, in particular the number of ester links in the sidechain, have a significant effect on the ^{19}F NMR peak positions of all sidechain peaks. Differences of up to 2 ppm in the resonance frequencies of sidechain fluorocarbon groups between the short chain Solvay ionomer with a single ester link, and the longer chain ionomers with two ester links per sidechain, were observed. This allows for the unambiguous determination of

a key feature of the ionomer structure by ^{19}F NMR. Further work could explore whether chemical shift differences are also observable by ^{13}C NMR. ^{19}F NMR was also used to calculate the equivalent weights (EW) of a selection of commercial and experimental ionomers. In the case of the short chain ionomers the EW determined by NMR were 3 to 4 % greater than values quoted by manufacturers. While estimates for the longer chain ionomers were 7 to 14 % below quoted values; a discrepancy greater than the experimental error. Without further information concerning the synthesis of these materials and the subsequent analysis that leads to the EW given by manufacturers the cause of the difference between the two sets of values cannot be known. Such information would also inform the interpretation of ^{1}H peak widths as to whether variation is caused by structure, method of synthesis or both.

A combination of ^{19}F and ^{1}H MAS NMR was used to determine key variables in the treatment and preparation of Nafion samples that may affect their NMR spectra. Water content, thermal history, MAS above 24 kHz, room temperature grinding of membranes and inhomogeneous heating of the sample were all identified as altering NMR spectra and were therefore controlled when necessary. Once these variables were controlled there were no discernable differences in ^{19}F NMR spectra of a series of Nafion membranes that had been cast from aqueous and organic solution and dried at room temperature or under an IR lamp. However, peak width differences did persist in ^{1}H MAS NMR spectra. It was proposed that the water proton peak widths are a function of the homogeneity of the water environments within the membrane. The organic cast membranes displayed greater homogeneity than the aqueous membrane. This was interpreted as increased inhomogeneity in water-to-acid ratios among local regions of the membrane. This would in turn imply greater variation in the size of water clusters or tubes within the ionomer structure which could well affect water and thus proton conductivity as well as mechanical properties. It had been proposed that the rapid drying of a membrane cast from water could make it more similar in structure to those cast from organic solvent. NMR results in fact show the opposite with the IR dried aqueous membrane exhibiting even wider ^{1}H water peaks.

While ^{19}F remains a useful tool as a check of sidechain structure and relative equivalent weights it appears to have limited value in aiding the development of bulk polymer membranes. ^{19}F-^{13}C CP NMR linewidths showed a similar dependency on

ionomer mobility as ^{19}F NMR but signal-to-noise for realistic timescales was insufficient when using cut or rolled membrane samples making it an unfavourable technique for studies of larger sample sets to aid fuel cell development

Both ^{19}F and ^{1}H NMR were used to study Nafion coated on the surface of dried fuel cell catalyst inks and it was found that the manner in which Nafion and water are arranged is categorically different to the bulk. Monomolecular layers of Nafion deposited from either aqueous or organic solvent are less mobile, ordered or both than their bulk analogues. Adding extra ionomer to the aqueous ink makes the ionomer even less bulk-like and alters the conformation to reduce or eliminate the fraction of water associated with the acid groups at the ends of the sidechain. Adding ionomer to the organic inks has the opposite effects, making the general structure and/or dynamics more bulk-like and establishing an acid-water network. While this final effect can be intuitively understood as the material becomes more like the bulk as the layer becomes thicker, the reasons for solvent differences and the behaviour of the aqueous ink with higher ionomer loading is less clear. It is possible that the polar sidechain of the ionomer becomes more closely associated with the surface of the catalyst when deposited from water as the ionomer is not bound so tightly in its micellular structure in an abundance of water. The Nafion in the organic inks could maintain its micelles better as the polar water and sidechains associate with one another and are separated from the hydrophobic backbones and solvent. These results could have important implications for the optimisation of the proton conductivity of these inks as it is likely that any morphologically differences are at least partially the result of the interaction between the ionomer and the catalyst, and significantly affect the water and thus the mode of charge transport. A better understanding of how the solvent and ionomer concentration influences this boundary could well result in improvements in overall MEA conductivity.

Chapter 5

5. Fuel Cell Catalysts

5.1 Introduction

As mentioned in Section 1.1.3, solid-state NMR is an established technique for the study of the metallic nanoparticles in supported fuel cell catalysts. ^{195}Pt NMR is predominant both because it is the most commonly used metal in the catalysts and because of its relatively high gyromagnetic ratio compared to ^{99}Ru, ^{101}Ru, ^{103}Rh and ^{105}Pd. Due to the Knight shift range of the particles, the signal is distributed across a range greater than 3 MHz on a 7.05 T NMR system which is far larger than the maximum acquisition bandwidth. Standard Fourier transform techniques are therefore not appropriate and a point-by-point linewidth reconstruction technique has been the norm throughout the literature. However, this work is primarily concerned with an FT field sweep method that offers a more complete reconstruction of the lineshape along with improved quantification and full automation. A full discussion of these techniques can be found in section 2.4.3.

5.2 Point by Point ^{195}Pt NMR

Although the aim of this work is to prove the application of field sweep NMR to metallic nanoparticles, a comparison with results using the existing technique on the same samples is beneficial for several reasons. Firstly, the samples were research materials supplied by JMTC and therefore not guaranteed to be comparable to commercial samples studied in the literature. The methods of synthesis and distribution of the particles onto their support will influence particle size distributions which in turn will change NMR spectra. Secondly, the surface signal has been widely shown to be sensitive to adsorbates and it is possible that the exact nature of the support even when compared to other graphitic materials could be a source of spectral variation. Finally, the common practice in the literature is to reduce the particles electrochemically for NMR but this convention was not followed and therefore direct comparisons with the literature are not valid. Details of the methodology used for point by point experiments are detailed in section 3.2.3.

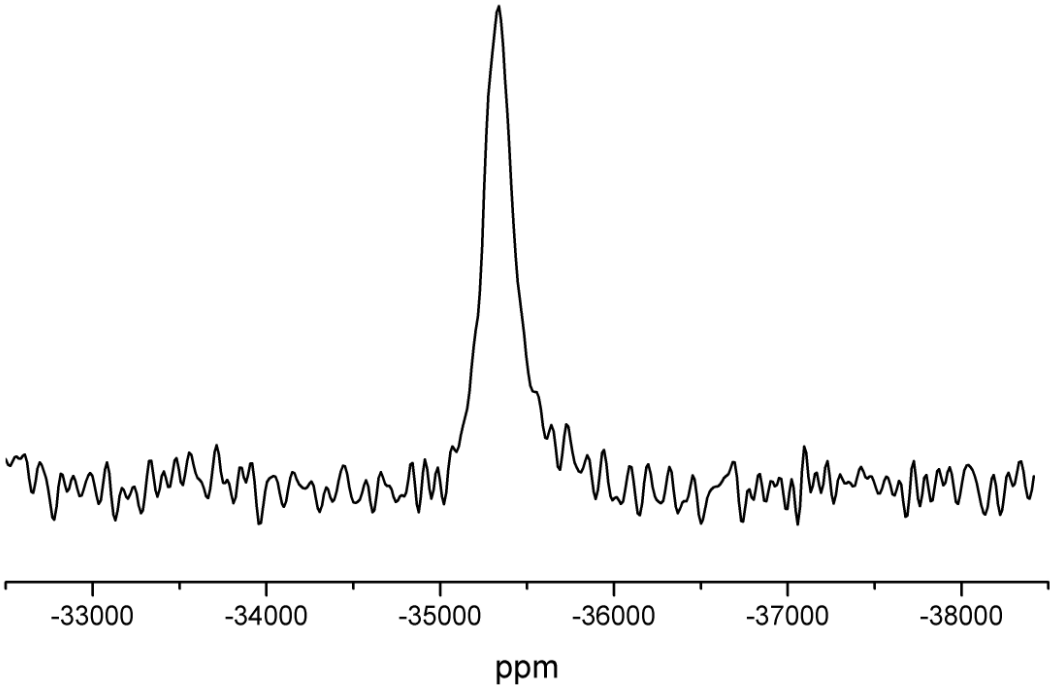

Figure 5.1: ^{195}Pt NMR spectrum of mesh325 platinum metal particles.

Figure 5.1 shows the ^{195}Pt spectrum of 'bulk' platinum. These are platinum particles filtered through a mesh which only lets particles with a diameter smaller than 44 μm pass through it. The small particle size is necessary to combat the skin depth effect which prevents the NMR pulse from penetrating through a conductor. As shown in section 3.2.1 the skin depth for platinum is 20.85 μm at 62.2 MHz and therefore the rf field strength will be within a few percent of the field strength at the surface for almost the entire particle even if it is as large as the 44 μm allows. The particles could be considerably smaller than the maximum filter width but the size at which they cease to appear bulk-like in ^{195}Pt NMR is expected to be around 0.02μm and figure 5.1 suggests that the platinum close to the mesh325 particles surface is too small a proportion of the total to be detected. The bulk site observed in figure 5.1 is positioned at –35350 ppm and its FWHM is 190 ppm or 12.25 kHz.

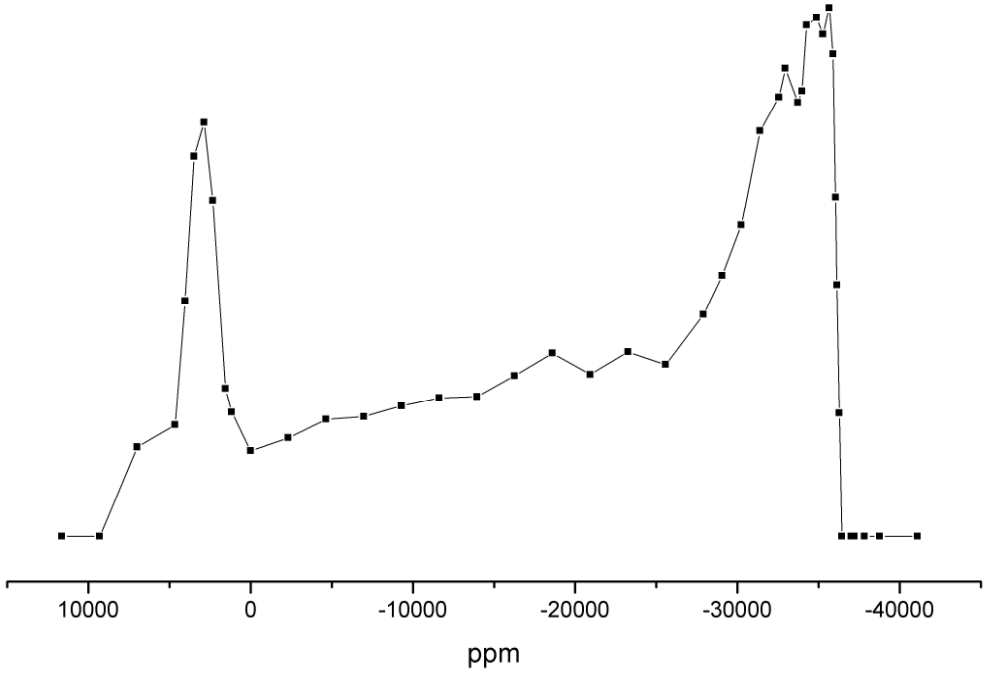

Figure 5.2: Point-by-point ^{195}Pt NMR spectrum of an unsupported platinum black. Particle size ~5nm.

As mentioned above, once platinum particles become smaller than around 20 nm surface effects cause a Knight shift distribution [63] over 3 MHz on a 7.05 T spectrometer so standard FT NMR is not suitable and wideline NMR methods must be employed. Figure 5.2 shows the point-by-point spectrum of unsupported platinum particles which have an average particle size of 5 nm as determined by Scherrer analysis of XRD data. It was previously stated in the literature that no such surface effect spectrum could be measured for unsupported particles [67] . It must be assumed that Tong *et al.* were referring to unsupported blacks that were electrochemically reduced before attempting NMR and this may be why a similar spectrum to figure 5.2 could not be recorded. Chemical reduction of the unsupported particles by formic acid as described in equation 5.1 was attempted with an excess of formic acid and the products were packed into a NMR sample holder.

$$PtO + CHOOH \rightarrow Pt + CO_2 + H_2O \qquad [5.1]$$

It was not possible to tune the probe with the reaction mixture inside and it was concluded that the reduction process had formed continuous volumes of conducting platinum with radii greater than the skin depth. If electrochemical reduction had also caused platinum aggregation it would explain the lack of surface effects in the observations of Tong *et al.* Figure 5.2 shows that a spectrum similar in form to that of supported nanoparticles [63] can be recorded for unreduced unsupported particles. As would be expected for an unreduced sample there is a significant peak centred around 2500 ppm that is assigned to platinum oxide close to the surface of the particles. A basic deconvolution of the spectrum suggests that approximately 15% of the signal can be attributed to platinum oxide, however later work (see section 5.2) has calculated that the signal is only 75% of the full real intensity due to T_1 saturation, so a reasonable estimate would be 20% of the platinum is oxidised. This can be compared to the figure of 25% for the amount of platinum in the surface layer given in the model shown in table 5.2, suggesting an almost complete atomic layer of the particles is oxidised.

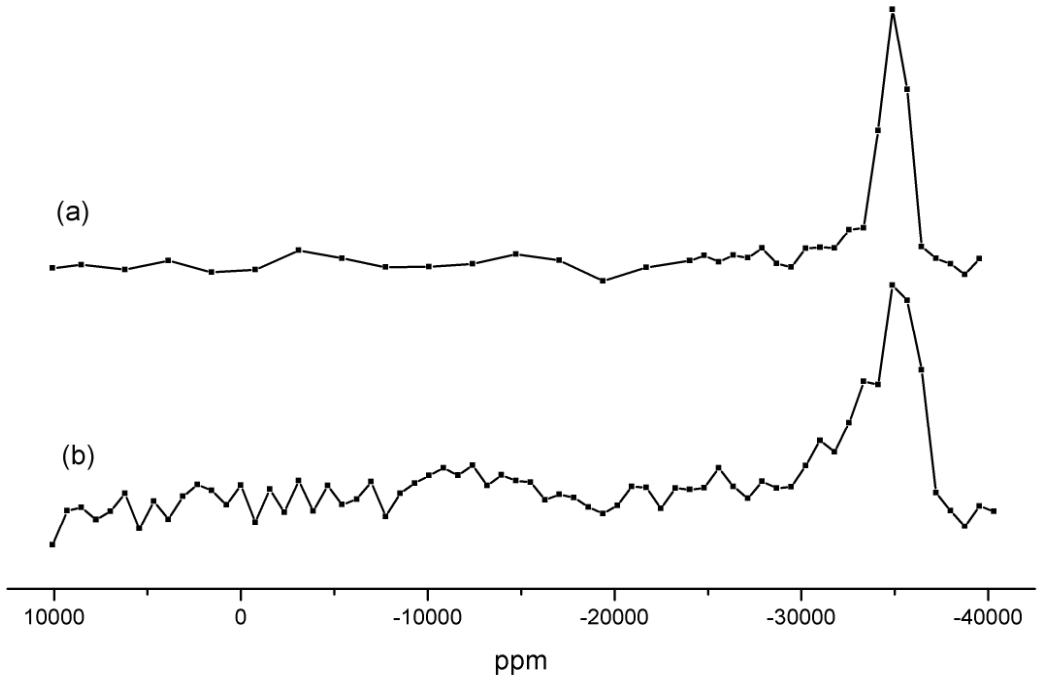

Figure 5.3: Point-by-point ^{195}Pt NMR spectra of platinum (40% metal by weight) blacks supported on a graphitic carbon aggregate. (a) particle size 15 nm (b) particle size 7.7 nm.

Figure 5.3 shows the point-by-point spectra of two supported platinum blacks. Although most recent ^{195}Pt NMR work has concentrated on particles with average sizes of ~2 nm [65-67] spectra of particles with comparable size distributions to both (a) and (b) can be found in [61]. The lack of a high intensity narrow peak at the bulk position around –35000 ppm could simply be the result of insufficient data points in that region. The resolution of narrow features with this method is limited by the sample frequency of the points on the spectrum. The signal-to-noise ratio of figure 5.3 makes the comparison of signal from the surface, sub-surface and oxide layers impossible, but the trend of a broadening distribution with increased contribution from layers further from the bulk resonance observed in figures 2 and 3 is consistent with the literature. In summary, there is no reason to believe the JM samples considered in this chapter will produce significantly different spectral patterns to those already observed in the literature.

5.3 Field Sweep ^{195}Pt NMR

The application of ^{195}Pt NMR to catalyst materials has been well established for decades [59-61]. The model developed by Bucher *et al.* [63] remains the standard but is by self admission not an attempt at a complete quantitative theory. While other more complex models have been developed [65], they do not result in a full model of the spectra found in the literature. It is intuitive that if a more complete and accurate model of these spectra is to emerge its development and assessment would be assisted by comparison with a more complete and quantitative technique for the experimental generation of the lineshapes. Additionally, if metal NMR is to be of use to the process of research and development of catalysts it must be able to detect, identify and interpret the spectral changes that results from variations of metal content, synthesis method and support materials. A mainly qualitative approach will not be sufficient to guide and inform catalyst development as changes between samples with greatly different reaction properties can produce qualitatively comparable spectra, as seen in figure 5.3.

A comparison between field sweep and point-by-point reconstruction requires common samples, so the first two samples, (a) and (b), displayed in figure 5.4 below

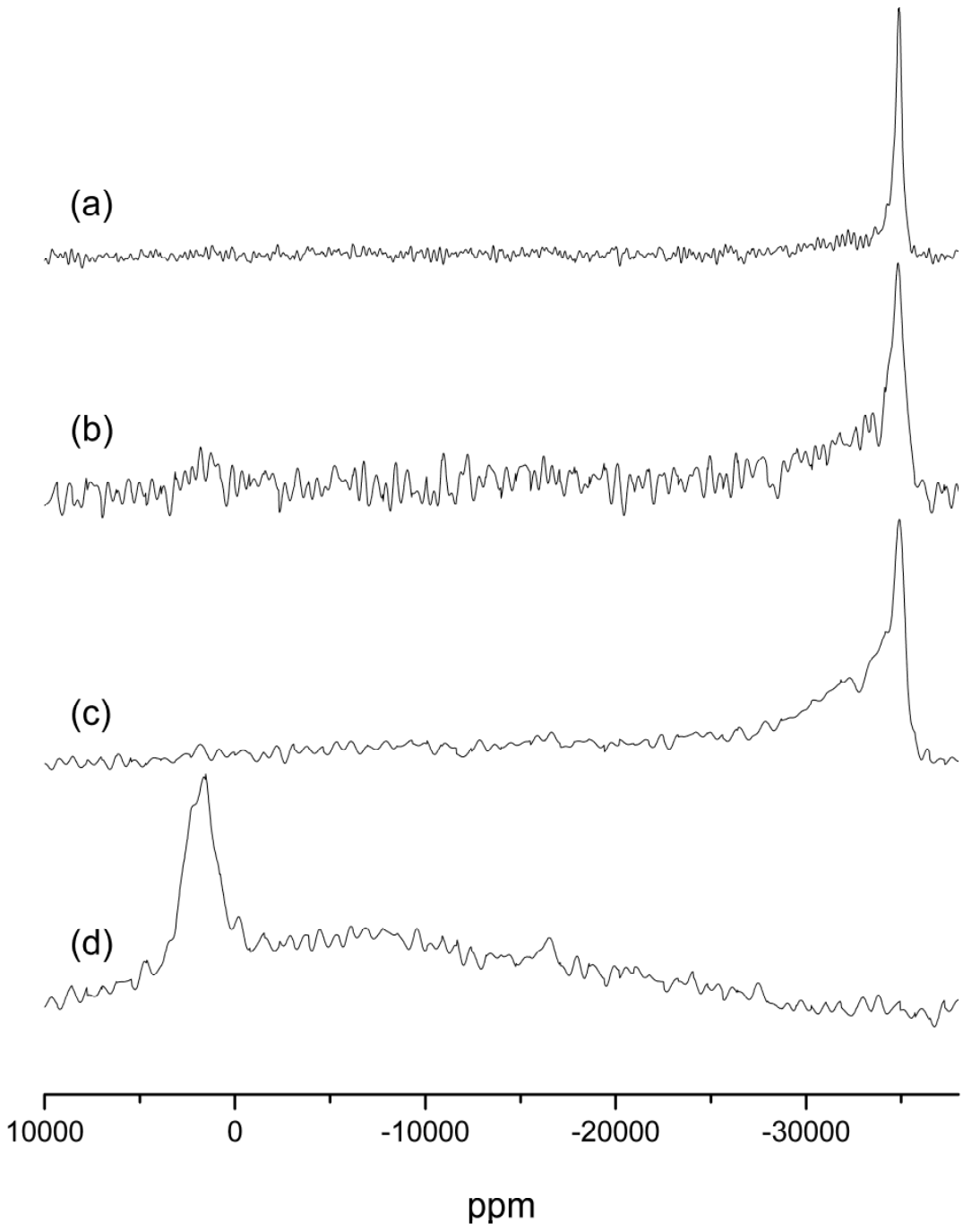

Figure 5.4: ^{195}Pt Static Field Sweep NMR spectra of supported platinum blacks with different particles sizes. (a) 15 nm, (b) 7.7 nm, (c) 5 nm and (d) 1.8 nm. Sample (a) and (b) are 40% platinum by weight while (c) and (d) are 60% platinum.

are identical to those in figure 5.3. At first glance there appears to be a large disparity between the two sets of results as the field sweep method measures much narrower bulk peaks than found in the frequency stepping spectra. However, this can be readily explained if the frequency stepping method is not fully recording the narrowest spectral features. This could be due to the data points being too far apart or because the narrower components of the FID do not contribute to the peak echo height proportional with the broader components. Both pairs of spectra show the same trends but the field sweep data are both more complete and more reliably quantitative.

Spectra (c) and (d) of figure 5.4 are of blacks with smaller particle sizes and a higher platinum content by weight. The higher metal content was necessary to achieve comparable signal-to-noise to (a) and (b) in a realistic time scale at 273K. All four spectra were fit using the shell model described in Section 2.2.4. The peak positions were defined by the healing model of equation 2.15, with K_0 set by the fit of the surface peak in (d) and K_∞ set by figure 5.1. The healing length was defined by the positions of the sub-surface 1 and 2 peaks and was set at 1.5 nm for all samples. The position of the bulk peaks were fit manually. The peaks widths were allowed to change to fit the data but the widths of all but the bulk peak were consistent across all 4 fits and increased monotonically as the layers approached the surface. The resulting fits are shown below in figure 5.5 and the data in tables 5.1-5.3.

.

Peak	**Position (ppm)**	**Width (ppm)**
Oxide	1837 ± 25	1950 ± 100
Surface	–6354 ± 300	17552 ± 1000
Sub-Surface 1	–20463 ± 150	12116 ± 1000
Sub-Surface 2	–27707 ± 50	11000 ± 2000
Sub-Surface 3	–31426 ± 25	4000 ± 250
Sub-Surface 4	–33335 ± 10	3000 ± 250
Sub-Surface 5	–34316 ± 10	1250 ± 100

Table 5.1: Positions and widths of all but the bulk peaks in the fits of figure 5.5

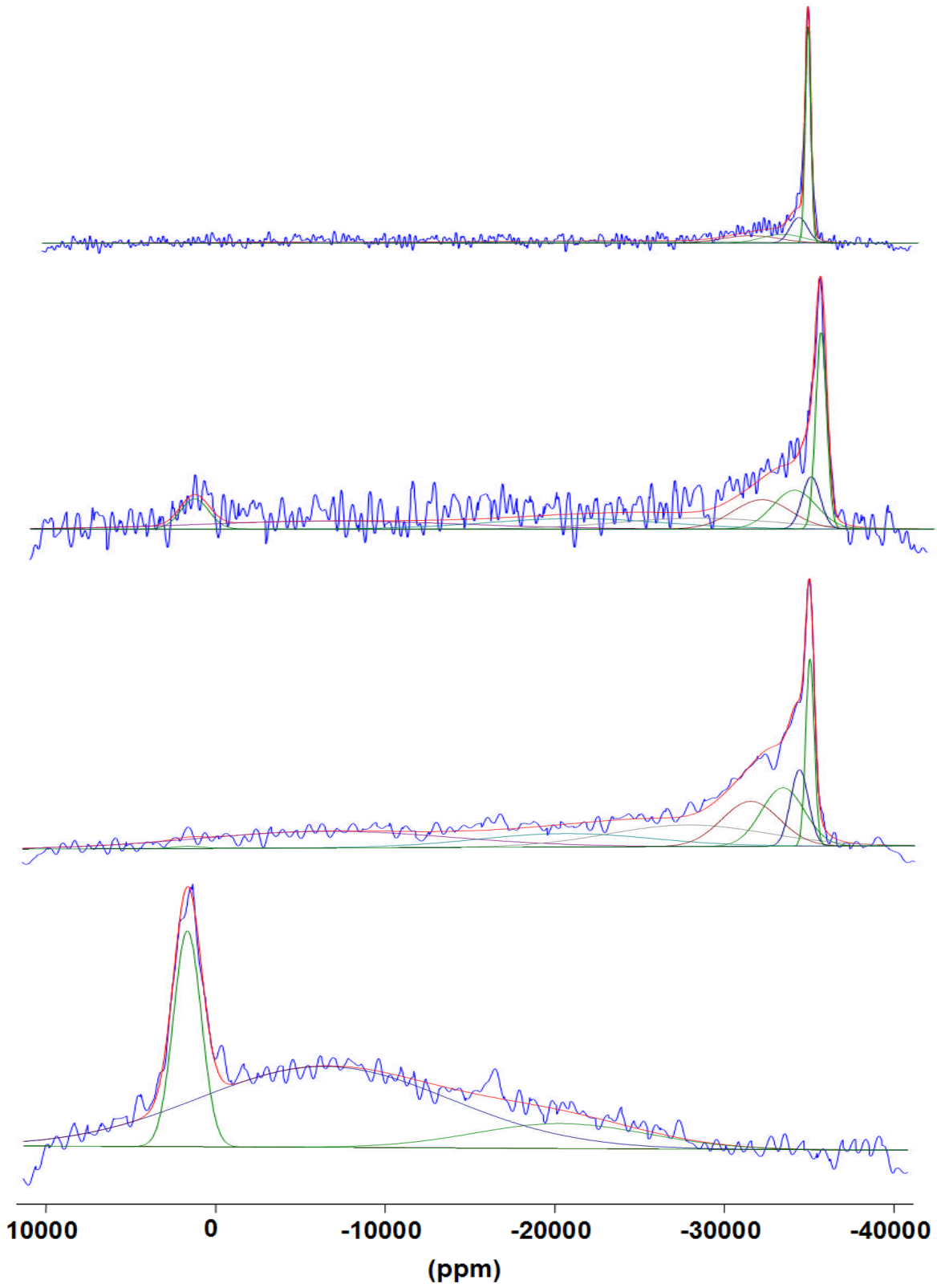

Figure 5.5: ^{195}Pt deconvoluted static Field Sweep NMR spectra of supported platinum blacks with different particles sizes. (a) 15 nm, (b) 7.7 nm, (c) 5 nm and (d) 1.8 nm. Sample (a) and (b) are 40% platinum by weight while (c) and (d) are 60% platinum.

While (a), (b) and (c) follow a clear trend of diminishing bulk content and increased signal in the surface and subsurface peaks as the particle size decreases, spectrum (d) is radically different as all the platinum nuclei are either on the surface or within 1 or 2 layers of it. While the overall agreement between model and experiment is good and the same parameters with identical healing length can be applied to all 4 pure platinum samples as would be expected [115] there are several discrepancies in relative intensities that must be considered. Firstly the intensities of the bulk peaks 15 nm and 7.7 nm catalysts are considerably lower than predicted by the cubooctohedral layer model. Correspondingly the intensities for subsurface 3, 4 and 5 peaks are generally higher than predicted. As both the widths and intensities of these peaks are unconstrained by theory and are overlapping strong conclusions from individual intensities would be unwise but a more general trend can be relied upon.

While the positions of the bulk peaks trend towards the bulk value of –35000 ppm from figure 5.1 with increasing particle size as expected there is great variance in peak widths which is likely another sign of the inability of the model to accurately distinguish individual layers close to the bulk shift. The simplest explanation for intensity shifted from the bulk towards sub-surface peaks without any significant deviation in the surface peaks is that the geometry of the particles are non-spherical. As a particle approaches a more hemispherical configuration a smaller and smaller proportion of atoms will be found 6 or more layers from the surface. The reduced symmetry of such a particle requires a more sophisticated model than is being considered here but no such complete theoretical treatment can be found in the literature likely due to the relativistic complications of a nuclei as heavy as platinum.

Sample	Relative Peak Intensities (%)															
	Oxide		Surface		SS1		SS2		SS3		SS4		SS5		Bulk	
	Fit	Model	Fit	Model	Fit	Model	Fit	Model	Fit	Model	Fit	Model	Fit	Model	Fit	Model
(a) 15 nm	2.0 ± 1	-	8.4 ± 5	8.9 (–0.5)	8.1 ± 5	8.4 (–0.3)	7.3 ± 5	7.9 (–0.6)	12.7 ± 5	7.3 (5.4)	11.1 ± 3	6.9 (4.2)	13.6 ± 3	6.4 (7.2)	36.8 ± 0.5	54.2 (–17.4)
(b) 7.7 nm	6.6 ± 0.5	-	15.7 ± 5	16.2 (–0.5)	14.2 ± 3	14.3 (–0.1)	13.4 ± 3	12.6 (0.8)	13.1 ± 3	11.0 (2.1)	13.0 ± 1	9.5 (3.5)	7.3 ± 0.5	8.1 (–0.8)	16.7 ± 0.5	28.4 (–11.7)
(c) 5 nm	0.3 ± 0.3	-	22.6 ± 1	25.9 (–3.3)	17.7 ± 1	21.0 (–3.3)	16.1 ± 2	16.6 (–0.7)	13.9 ± 1	12.7 (1.2)	13.6 ± 1	9.4 (4.2)	7.4 ± 0.5	6.5 (0.9)	8.5 ± 0.5	8.0 (0.5)
(d) 1.8 nm	19.5 ± 0.5	-	65.6 ± 3	62.6 (3.0)	14.9 ± 0.5	28.6 (–13.7)	0 + 1	8.2 (–8.2)	0 + 0.5	0.7 (–0.7)	0 + 0.5	0 (0)	0 + 0.5	0 (0)	0 + 0.25	0 (0)

Table 5.2: Comparison of relative peak intensities of fits displayed in figure 5.5 compared to those dictated by the layer model described in section 2.2.4. Errors in fit intensities are given below the corresponding result, for fit intensities of zero the maximum intensity within error, x, is denoted as + x. The discrepancy between experimental fit and theory are given below the values predicted by the model, these are presented as fit – model. Model particle sizes were as follows: (a) 14.90 nm 33 layers (b) 8.01 nm 18 layers, (c) 4.8 1nm 11 layers, (d) 1.62 nm 4 layers.

Sample	Position (ppm)	Width (ppm)
15 nm	–34874 ± 25	398 ± 25
7.7 nm	–34895 ± 50	757 ± 25
5 nm	–34934 ± 10	590 ± 25
1.8 nm	-	-

Table 5.3: Positions and widths of bulk peaks in the fits of figures 5-8.

It can be stated using the current model that this loss of symmetry is more pronounced in particles larger than 5 nm. Whether the non-spherical shape of the particles originates in their method of synthesis or is caused by interaction with the support could best be answered by carrying out similar studies on unsupported particles.

Spectrum (d) does not have any intensity concentrated close to the bulk shift and most of the nuclei are to be found at the surface as would be anticipated in such a small particle. The higher than expected ratio of surface to sub-surface platinum suggests that the particles might not be perfect 4-layer cubooctohedrons but have a significant number of defects or vacancies that increase surface area to volume ratio. While a significant proportion of the platinum is oxidised, it is not close to the amount needed for a complete surface layer around the metallic platinum so not every platinum atom on the exterior of the particles is oxidised. This poses a problem for the layer model as it means that some of the metallic ‘surface’ will be exposed to air while other ‘surface’ atoms will be below platinum oxide. A difference in the local electron structure between the two states would be expected and this could be an alternative explanation for the differences between the model and spectrum (d) as no compensation for oxidation is made. Acquiring a spectrum of the same sample in a reduced state would help in determining the strength and nature of any oxide effect.

While spectra (a), (b) and (c) would not expected to be as affected by oxidation to the same degree, the absence of an oxide layer in (c) must be noted and

considered. Once saturation of the oxide peak has been taken into account the intensity of the oxide layers in (a), (b) and (d) represent a covering of the metallic surface between 30 and 50%. Three possible explanations for the lack of detection of the oxide present themselves. Firstly, the oxide layer could be absent from the 5 nm particles, secondly the layer could be undetectable due to longer spin-lattice relaxation or thirdly the oxide resonance could be greatly broadened. It has been proposed that the orientation of the surfaces of metallic nanoparticles can affect its catalytic properties and might be dependent on particles size [7] as an explanation for the activity-size relationship. If this were the case it is possible the same effect is preventing oxidation of the surface or altering its nature, causing longer relaxation or broadening. Another factor could be the separation between particles which would be not only affected by particle size but also metal content. If a higher density of particles on the support discouraged oxide formation it could explain why an oxide layer is present in (a) and (b) with 40% platinum but not in the 5 nm 60% sample.

5.4 Conclusions

^{195}Pt NMR of platinum fuel cell catalysts and an unsupported precursor was carried out by the standard point-by-point method and by a summed Fourier transform field sweep method. Contrary to the literature it was found that unsupported platinum nanoparticles can exhibit the same Knight shift distribution in their ^{195}Pt NMR spectra as supported particles do. However, it is proposed that this will only hold true if the particles are not reduced before undergoing NMR. Complete Fourier transformed ^{195}Pt NMR spectra of platinum catalysts of various particles sizes were presented and fitted according to the standard layer-by-layer model. Experimental values derived from this model suggested that the larger (> 5 nm) particles were sufficiently distorted from the ideal spherical symmetry as to have several percent more nuclei in layers a few atoms from the surface than a cubooctohedral particle would. A corresponding decrease in ‘bulk’ nuclei deep inside the particles was observed. This implies that the platinum particles are non-spherical and are most likely flattened on the side closest to the carbon support. This reduces the surface of the particle available for catalysis. In contrast the 5nm sample showed the smallest deviations in percentage layer content from an octahedral model while the 1.8 nm particle exhibited less intensity below the surface layer than would be expected of a spherically symmetric particle. It is striking

the 5 nm particle shows the highest degree of symmetry given the well known particle size effect of catalytic activity of these particles with a peak in activity per unit surface area at diameters of 5nm. While it was determined that between a third and a half of the surface platinum atoms were oxidised in three of the catalysts, the 5nm particles showed no evidence of oxidation. The orientation of the surfaces exposed for possible oxidation and the distance between these surfaces, a function of the weight content of platinum in the catalyst, are offered as possible explanations. Both sets of observations above suggest that the 5nm sample had unique properties and as this particle size corresponds to the optimum balance between surface area and activity of the surface they provide possible insights into this currently unexplained and vitally important effect.

Chapter 6

6. Aluminoborosilicate Glasses in the BN1 Ceramic

6.1 Introduction

NMR has long been a key technique for advancing the understanding of glasses and other non-crystalline solids. As a technique which can be applied to amorphous materials and probe medium-range order it has value in quantitative analysis of the coordination, connectivity and abundance of many of the nuclei commonly found in glasses. Its elemental specificity, identifying each chemical environment, makes it a good complement to many techniques which study the macroscopic average properties of the glass or the average properties of a certain element such as EXAFS.

The selection of BN1 glass-ceramics described in section 3.3.1 and [79-80] were studied by ^{27}Al, ^{11}B and ^{29}Si NMR in an attempt to discern the composition and structure of the glassy phases in the material. The results are presented below.

6.2 ^{27}Al NMR

Thanks to the favourable NMR properties of the ^{27}Al nucleus shown in table 6.1 and its ubiquity in nature (8.1% of the Earth's crust) it is a well established nucleus for solid state NMR which lends itself to complex and multidimensional experiments. The combination of being the lone stable isotope of aluminium and having a high gyromagnetic ratio grants good sensitivity. The quadrupole moment is small enough that the broadening caused is less than the chemical shift range (400ppm) at high fields, allowing resolution between non-symmetrical environments.

Isotope	Abundance (%)	Spin	Quadrupole Moment (Qm^{-2})	Gyromagnetic Ratio ($radT^{-1}s^{-1}$)	Absolute Sensitivity ($^1H = 1$)
^{27}Al	100	5/2	0.15×10^{28}	6.976×10^{-7}	0.21

Table 6.1: The NMR properties of the ^{27}Al nucleus.

However, the distribution of quadrupolar broadening resulting from disorder in materials like the glasses considered here requires multidimensional experiments to achieve quantitative resolution.

6.2.1 One Dimensional Experiments

The spectra acquired from one pulse experiments at 14.1 T on each of the BN1 samples are show below in figure 6.1. Spectrum (a) of the as cast sample shows a typical ^{27}Al glass spectrum [116] with peaks corresponding to aluminium coordinated with 4, 5 and 6 oxygens from left to right. The sample heat treated to 600 °C for two hours provides a similar spectrum in the 4 and 5 coordinated regions with reduced intensity while the six coordinated peak is positively shifted from 4.0 to 8.0 ppm and now represents a majority of the signal intensity. Once heated above 700 °C the ^{27}Al spectrum of the sample takes on a similar form that evolves from spectra (c) to (f). Broad peaks at 34 and 3 ppm are assigned to 5 and 6 coordinated environments respectively. Each peak represents environments with a range of quadrupolar couplings resulting in the broad featureless lineshapes observed and both remain unchanged in all spectra. A second peak in the five coordinated region appears in spectra (c) to (f) at 41 ppm which becomes narrower as the ceramic is heated at higher temperatures. The sharp feature observed at 0.4 ppm only appears in (f) and is too narrow and defined to be hidden in lower temperature spectra. It is the high shift four coordinated region which sees the most change across spectra (c) to (f). While the glassy 4 coordinated aluminium peak around 53 ppm is found with reducing intensity in spectra (c) and (d), see below for evidence of its presence in (d), it appears to be absent from (e) and (f). Instead a relatively narrow resonance is observed in (d), (e) and (f) at 67.5 ppm which grows in intensity with increasing heat treatment temperature. A second broader feature emerges between 50 and 60 ppm which will be discussed in the following section.

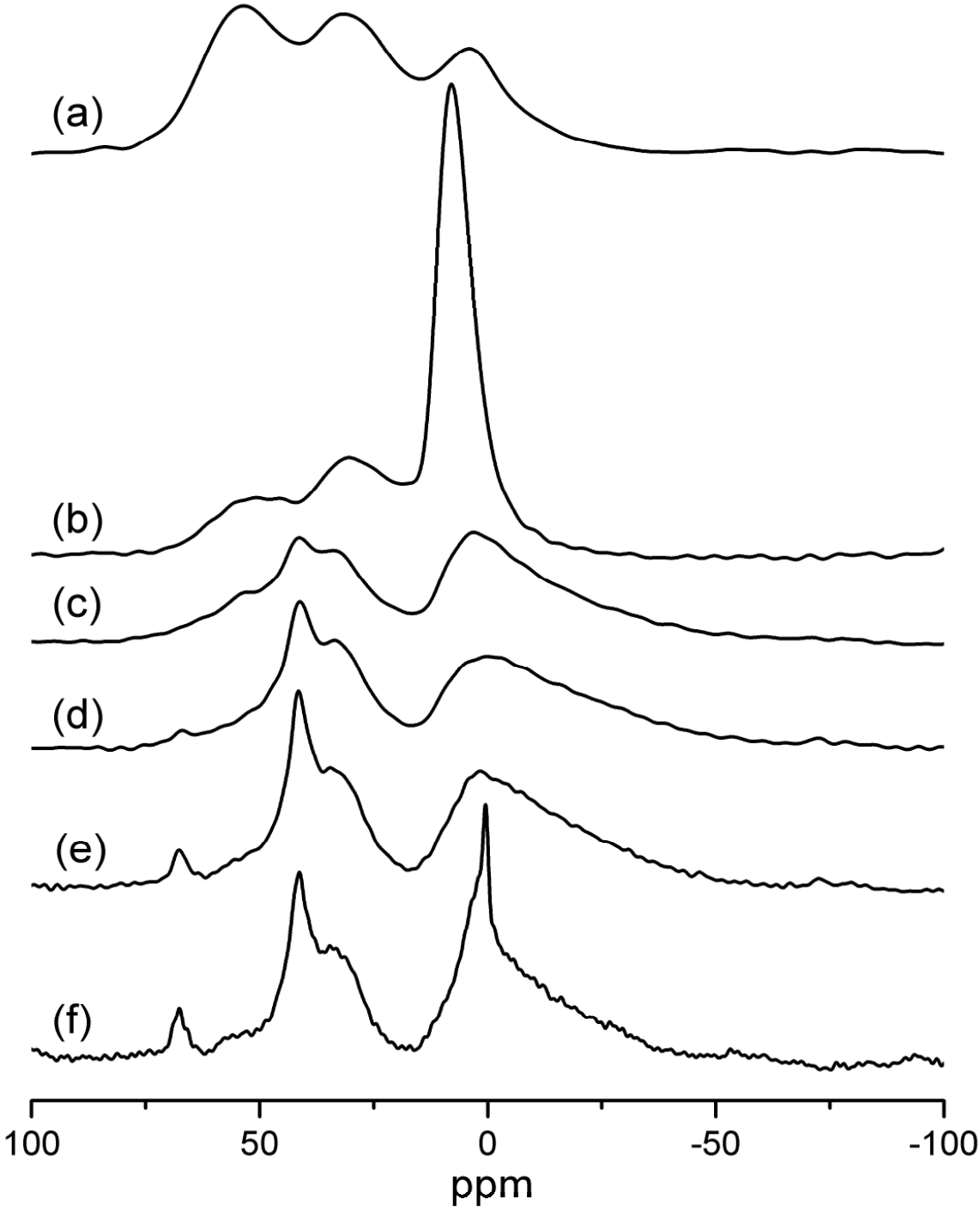

Figure 6.1: Stacked plot of one pulse ^{27}Al NMR spectra of (a) BN1 as cast, (b) BN1 600 °C, (c) BN1 700 °C, (d) BN1 800 °C, (e) BN1 900 °C and (f) BN1 1000 °C. Acquisition at 156.2 MHz, spinning at 14880 Hz.

6.2.2 MQMAS

Three MQMAS spectra were also acquired at 14.1 T in order to better understand the complex set of overlapping peaks observed in figure 6.1. These results are presented in figure 6.2. Spectrum (a) of the as cast material confirms the assignment of three broad peaks corresponding to each of the coordination numbers with no further resolution found in the isotropic dimension. Spectra (b) and (c) show that MQMAS has been successful in separating the lineshapes in the 20 – 60 ppm region into three peaks. The broadest component, centred at 34 ppm, is not further split but the narrower peak at 41 ppm is the result of two separate resonances. Therefore our understanding of the evolution of this peak through spectra (c) to (f) of figure 6.1 can be refined. It appears that rather being a single resonance which narrows at higher temperatures, intensity is transferred from a broader component to a narrower one , both centred at the same chemical shift. The broad peak in the 6–coordinated region remains a single resonance in the MQMAS experiments but the narrower feature which appears only in the 1000°C treated sample is distinct from the broader signal. The peak 67.5 ppm is detected in both samples but the feature between 50 and 60 ppm is only barely detectable above the noise in figure 2 (c).

6.3 ^{11}B NMR

While boron has two NMR active nuclei, in most studies ^{11}B is preferred for its higher gyromagnetic ratio, relative abundance and its half integer spin. Much like ^{27}Al, ^{11}B is a sensitive quadrupolar nucleus suitable for rapid 1-D experiments or a variety of multidimensional experiments on a reasonable time scale.

Isotope	Abundance (%)	Spin	Quadrupole Moment (Qm^{-2})	Gyromagnetic Ratio ($radT^{-1}s^{-1}$)	Absolute Sensitivity ($^1H = 1$)
^{10}B	19.58	3	8.5×10^{26}	2.875×10^{-7}	3.93×10^{-3}
^{11}B	80.42	3/2	4.1×10^{26}	8.584×10^{-7}	0.13

Table 6.2: The NMR properties of Boron nuclei

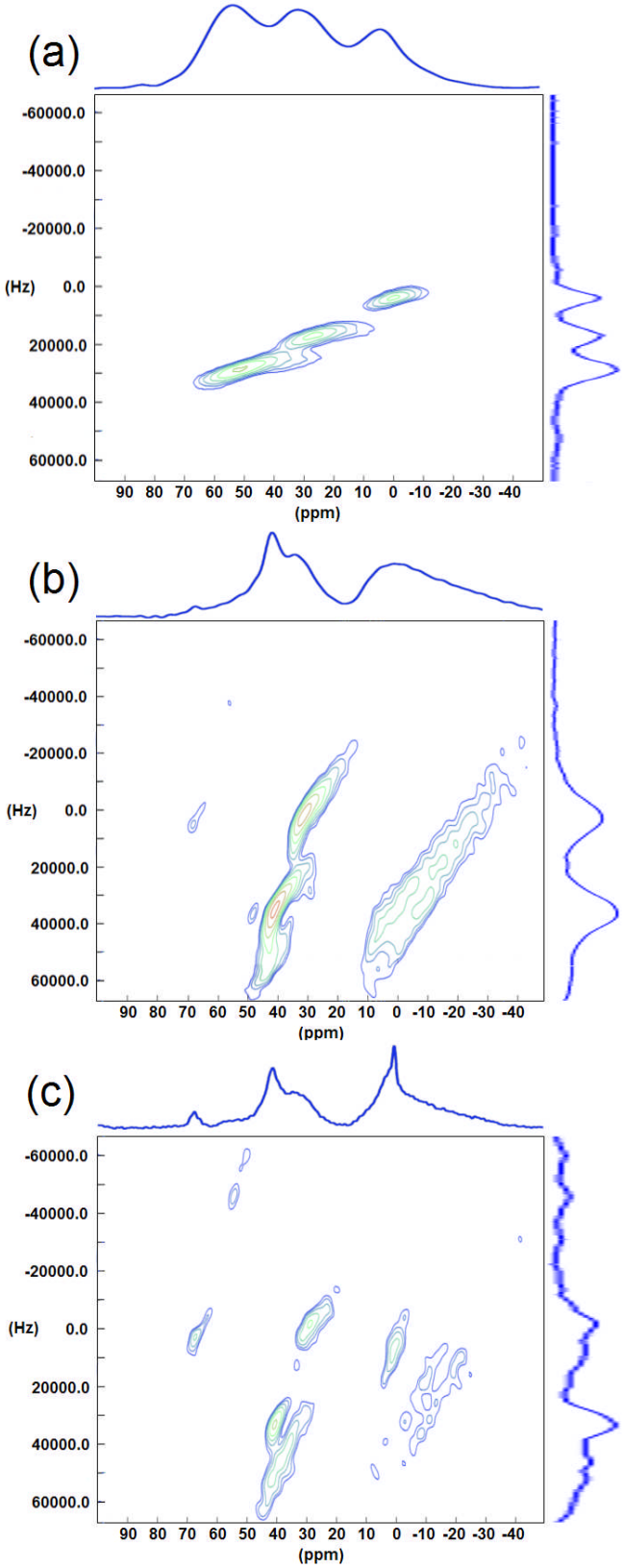

Figure 6.2: ^{27}Al z-filtered MQMAS spectra of (a) BN1 as cast, (b) BN1 800°C and (c) BN1 1000°C. All spectra acquired at 192.3 MHz spinning at 14880 kHz.

It's smaller chemical shift range (~200ppm) is not significant for glass studies as it is large enough to separate BO_3 and BO_4 sites while quadrupolar broadening and parameter distributions due to disorder mean sites of the same coordination can often only be distinguished by 2-D spectra.

6.3.1 One Dimension Experiments

Figure 6.3 shows the ^{11}B one pulse MAS spectra of the BN1 sample set. Two common spectra regions can be discerned from (a) to (f). From 5 to –3 ppm signal from four coordinated boron nuclei is found while [BO_3] resonances feature from 25 to 5 ppm. Across the set of spectra three distinct [BO_4] peaks can be identified. The broadest, centred at 1.5 ppm appears only in the as cast sample in (a). After heat treatment at 600 °C there is still a single four coordinated boron peak but it is narrower and more negatively shifted than in (a). While this peak is also observed in all the higher temperature samples it decreases in intensity monotonically. From spectrum (c) to (f) the narrowest of the three peaks is observed at –0.8 ppm and it grows in intensity at higher temperatures as the broader component diminishes. While it can be said that the [BO_3] region exhibits more defined spectral detail at higher temperatures there is still at least two overlapping quadrupolar lineshapes in (f) and therefore interpretation requires higher dimensional study.

6.3.2 MQMAS

As with ^{27}Al MQMAS, three triple quantum MQMAS experiments were conducted at 14.1 T and are shown in figure 6.4. Much like the corresponding spectrum in figure 6.2 the ^{11}B MQMAS spectrum of the as cast sample separates boron with different coordination numbers but is otherwise featureless. Spectra (b) and (c) however contain more information about the component parts of their corresponding one dimensional MAS spectra. The description of the four coordinated region from one dimensional spectra is confirmed with two separate peaks. Additionally, the broader component is narrower in the isotropic dimension and more

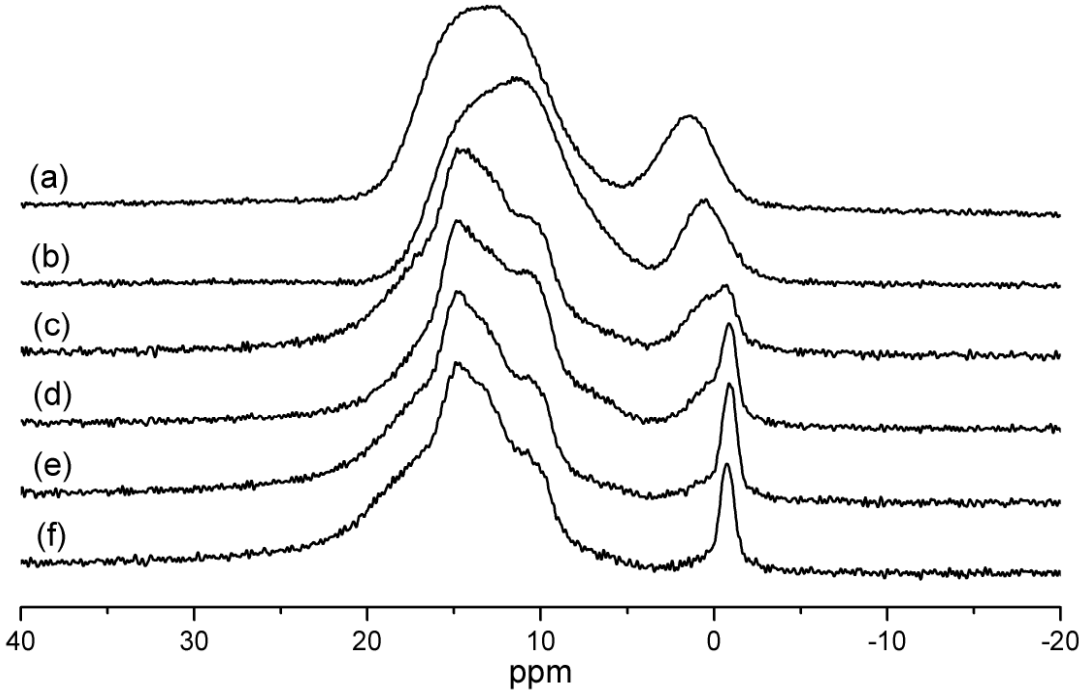

Figure 6.3: Stacked plot of one pulse ^{11}B NMR spectra of (a) BN1 as cast, (b) BN1 600°C, (c) BN1 700°C, (d) BN1 800°C, (e) BN1 900°C, (f) BN1 1000°C. Acquisition at 192.3 MHz, spinning at 14880 Hz.

positively shifted in (c) with respect to (b). It is in the [BO_3] region that the most new information is revealed. Two distinct quadrupolar lineshapes can be resolved in the isotropic dimension indicating multiple ordered three coordinated sites, as well as a smaller proportion of disordered material.

6.4 ^{29}Si NMR

As only a small percentage of silicon nuclei are NMR active at natural abundance, unenriched amorphous silicate samples are only suitable for simple one dimension experiments. Fortunately ^{29}Si is spin = ½ and therefore does not require MQMAS to resolve sites of similar coordination as chemical shift differences are large enough compared to the narrow linewidths of a non-quadrupolar nucleus.

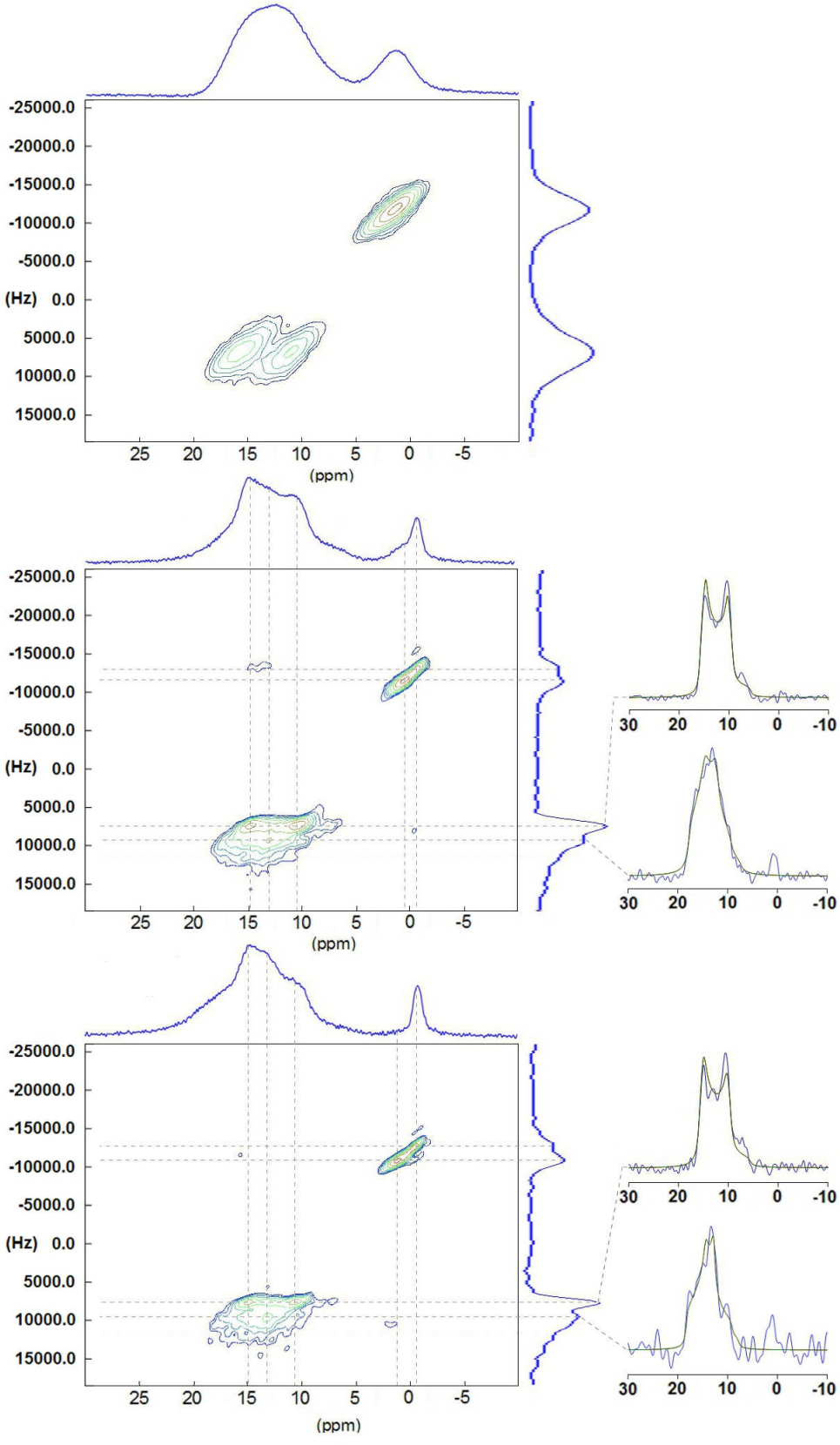

Figure 6.4: ^{11}B z-filtered MQMAS spectra of (a) BN1 as cast, (b) BN1 800°C, and (c) BN1 1000°C. All spectra acquired at 192.3 MHz spinning at 14880 Hz. Quadrupolar lineshapes are shown expanded right.

Isotope	Abundance (%)	Spin	Quadrupole Moment (Qm^{-2})	Gyromagnetic Ratio ($radT^{-1}s^{-1}$)	Relative Sensitivity ($^1H = 1$)
^{29}Si	4.7	1/2	0	-5.3188×10^{-7}	3.69×10^{-4}

Table 6.3: The NMR properties of the ^{29}Si nucleus.

One pulse ^{29}Si experiments are shown stacked below in figure 6.5 and their deconvolutions are shown in figure 6.6 while the positions, widths and intensities of each of the fits are shown in table 6.4. Spectrum (a) can be fit to a single broad Gaussian, as can (b). Spectra (c) to (f) have been fit to the minimum number of peaks possible. A consistent picture emerges from the fits of (c), (e) and (f) with three peaks in similar positions (92-93, 100-105, and 110-112 ppm) while (d) could also be fit to similar three peak model but the broadening of the central peak made a two peak fit possible.

6.5 Discussion

By combining the information gathered from NMR studies of aluminium, boron and silicon it is possible to give a more complete description of all the phases found in the BN1 ceramic when subjected to heat treatments up to 1000 °C than has previously been possible by the application of microscopy and x-ray diffraction [79-80].

The spectra of the as cast sample all point towards a complex glass that contains, 3 and 4 coordinated boron, 4, 5 and 6 coordinated aluminium and a wide range of silicon environments. It is highly likely that bismuth and niobium are distributed within the glass acting as network modifiers as the number of $[AlO_4]^-$ and $[BO_4]^-$ groups exceeds that of the $[AlO_5]^+$ and $[AlO_6]^+$ groups and as non-bridging oxygens are almost certain to exist within the glass also, additional positive ions must be present.

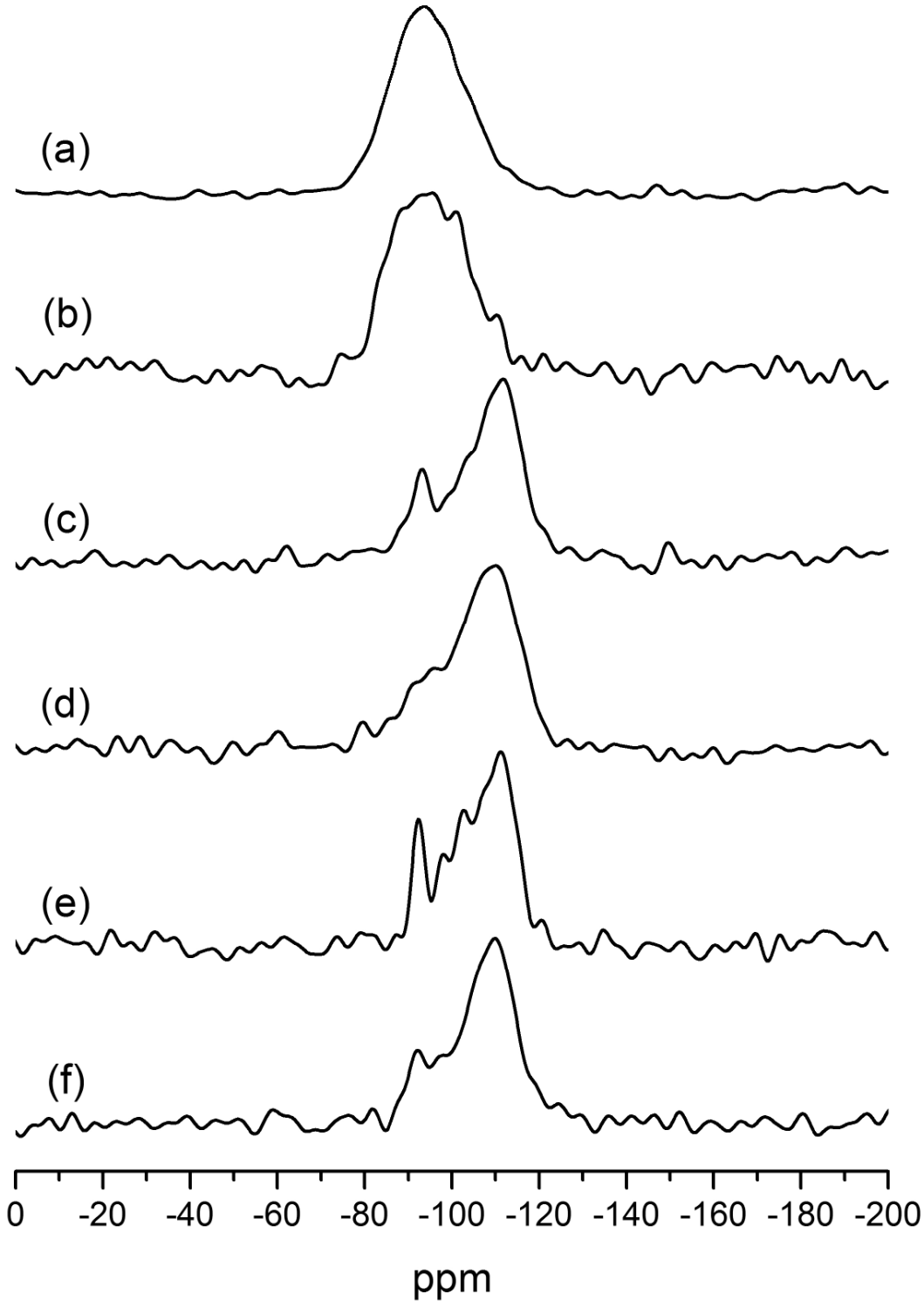

Figure 6.5: Stacked plot of one pulse ^{29}Si NMR spectra of (a) BN1 as cast, (b) BN1 600°C, (c) BN1 700°C, (d) BN1 800°C, (e) BN1 900°C, (f) BN1 1000°C. Acquisition at 59.5 MHz, spinning at 4.5 kHz.

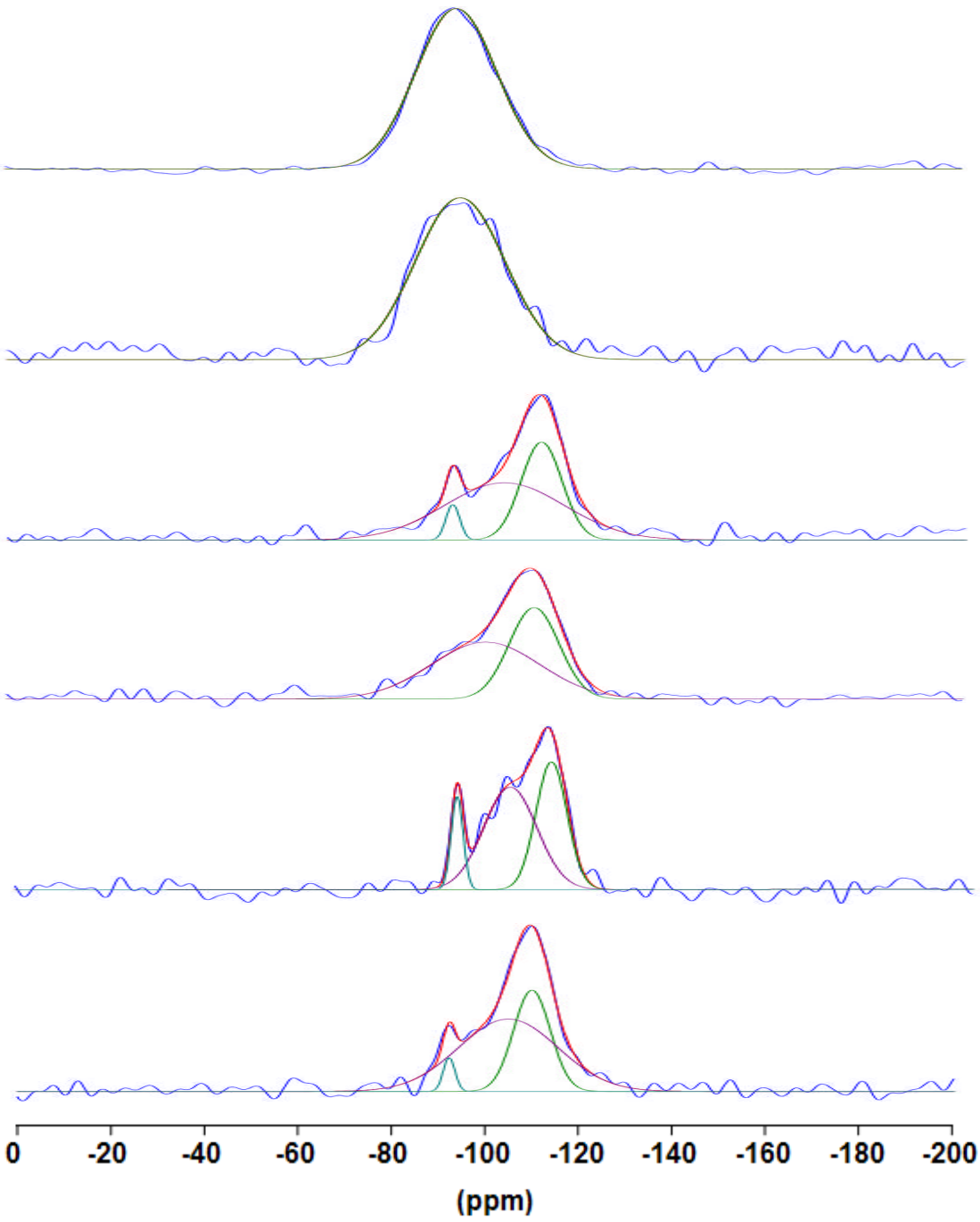

Figure 6.6: Stacked plot of deconvolutions of one pulse ^{29}Si NMR spectra of (a) BN1 as cast, (b) BN1 600°C, (c) BN1 700°C, (d) BN1 800°C, (e) BN1 900°C, (f) BN1 1000°C. Acquired at 59.5 MHz, spinning at 4.5 kHz.

Sample	Peak 1			Peak 2			Peak 3		
	Position (ppm)	Width (ppm)	Intensity (%)	Position (ppm)	Width (ppm)	Intensity (%)	Position (ppm)	Width (ppm)	Intensity (%)
As Cast	–94.2 ± 0.5	20 ± 1	100	-	-	-	-	-	-
600 °C	–95 ± 2	22 ± 1	100	-	-	-	-	-	-
700 °C	–111.3 ± 0.5	10 ± 1	35 ± 3	–103 ± 1	29 ± 1	60 ± 2	–92.8 ± 0.5	3.4 ± 0.5	4 ± 1
800 °C	–110.4 ± 0.5	12 ± 1	42 ± 4	–100.2 ± 0.5	26 ± 2	58 ± 4	-	-	-
900 °C	–111.9 ± 0.5	8 ± 1	38 ± 3	–103 ± 1	13 ± 2	52 ± 4	–92.2 ± 0.5	3.0 ± 0.5	11 ± 2
1000 °C	109.9 ± 0.5	9 ± 1	33 ± 3	–105 ± 1	25 ± 1	63 ± 4	–92.2 ± 0.5	3.0 ± 0.5	4 ± 1

Table 6.4: Table of values of the fits shown in figure 6.6.

While the ^{29}Si and ^{11}B spectra of the 600 °C sample appears similar to the as cast data, the ^{27}Al spectrum shows a large increase in the intensity from six-coordinated aluminium which is consistent with the formation of the Bi_2O_3-Nb_2O_3-Al_2O_3 pyrochlore phase which has been identified by TEM and EDS analysis in [80]. The changes seen in the boron spectra could be interpreted as the effect of some of the network modifying ions leaving the glass network. The unchanged ^{29}Si spectrum suggests that the positive ions are more tightly bound in the silicon rich areas of the glass compared to those primarily composed of boron as the network former.

While the NMR data presented here is consistent with the overall analysis of the structure of the BN1 ceramic once heated to 700 °C or above, and some additional information can be inferred. ^{29}Si NMR spectra of the four samples heated to or above 700 °C show spectra with similar peak positions and widths to those found in meta-kaolin [117] that had been formed from calcined, dealuminated kaolin. The broad $[AlO_5]$ and $[AlO_6]$ peaks observed in the ^{27}Al NMR spectra of the same samples match those observed in the same meta-kaolin materials. However, the relative abundances of each peak in both nuclei vary between the BN1 and dealuminated metakaolin and there is almost no comparable $[AlO_4]$ resonance in the BN1 spectra except shown in figure 6.1 (f) and 6.2 (c). The metakaolin spectra in [117] assign the three ^{29}Si peaks from highest chemical shift to lowest as Q^3 silicon with an $[AlO_6]^-$ next nearest neighbour, Q^3 or Q^4 with an Al next nearest neighbour and Q^4 silica. This analysis is consistent with a high silicon, low aluminium residual amorphous phase analysed by EDS in figure 7(c) of [80].

The boron in the BN1 ceramic is not considered in the analysis of the phase evolution of [80], it is perhaps assumed that it remains as a glass. ^{11}B NMR shows that this is not the case as an increasing proportion of both three and four coordinated boron is found in highly ordered crystalline environments as the heat treatment temperature increases. Additionally, the narrowing resonance at 41 ppm in the ^{27}Al NMR spectra is assigned to $Al(BO)_4$, strong evidence of an increasingly crystalline aluminoborate phase not previously considered.

While the bismuthniobate crystals which perhaps make up a majority of the BN1 ceramic after high temperature treatment are mainly outside the scope of this study the narrow ^{27}Al peak at 67 ppm is indicative of a four coordinated environment with six coordinated next-nearest neighbours and could relate to aluminium impurities in the BN crystals. While the presence of kyanite crystals in between the larger BN crystals is identified in [80] by SEM in samples treated below 1000 °C, ^{27}Al indicates that this phase only makes up a significant proportion of the aluminium content in figure 6.1 (f) by the appearance of a narrow peak at 0.4 ppm. The amount of silicon contained in kyanite crystals is too small for it to appear in the ^{29}Si spectra which would require greater signal to noise to detect such a small proportional of material.

6.6 Conclusions

Previous work on the structure of the BN1 glass-ceramic before and after heat treatment has be refined and augmented by a combination of ^{27}Al, ^{29}Si and ^{11}B NMR. NMR confirms that the as cast sample appears to be a uniform glass with no significant crystalline content. After heat treatment at 600 °C the emergence of an aluminobismuthniobate pyrochlore phase is confirmed by ^{27}Al NMR. Samples treated at higher temperature have another separate phase evolution. While the bismuthniobate crystals that make up a majority of these ceramics are not directly probed ^{27}Al suggests that aluminium impurities in these BN crystals become more common with higher temperature heat treatment. ^{29}Si NMR shows that a majority of the silicon is in a meta-kaolin like phase with a significant proportion of the aluminium. This phase is more ordered than the rapidly diminishing glass phase but cannot said to be crystalline. While previous work detected the growth of kyanite crystals around the larger BN crystals ^{27}Al NMR could only detect kyanite in the sample treated at 1000 °C and there was no sign of it in ^{29}Si spectra. This probably indicates that only a small, undetectable to NMR, amount of kyanite exists below 1000 °C but greatly increases once at this temperature. Finally the aluminoborate phase becomes increasingly ordered between 700 °C and 1000 °C showing a steady shift in proportions of glassy and crystalline material.

Chapter 7

7. Crystalline Platinum (II) Dialkyldithiophosphates

7.1 Introduction

X-ray diffraction studies provide a wealth of information about the short range structure such as bond angles and distances for molecules like the platinum (II) dialkyldithiophosphates ($Pt\{S_2P(O\text{-}R)_2\}_2$) being considered here. Solid-state NMR can provide complementary short-range structural information via the chemical shift and its anisotropy (CSA) along with dipolar and J-coupling, as well as probing the overall dynamics of the molecules. As discussed in Section 1.1.2 sulphur NMR does not have the sensitivity for this kind of study, but both ^{31}P and ^{195}Pt NMR can be applied. While ^{13}C and ^{1}H NMR can and have been applied [75-76] to this class of molecules they only give information about the ligands of the molecule which are varied across the sample set and therefore do not give information that can be compared between samples. The focus will rather be on the platinum-sulphur-phosphorus centres of the molecules and how they are affected by variation in the ligand alkyl groups.

7.2 ^{31}P NMR

While ^{31}P NMR has been reported for some of the complexes previously, they were included in order to facilitate comparison without the worries in differences in batch preparation or methodology between studies. As outlined in section 3.4.2 spectra at two different spinning speeds were recorded in order to allow the calculation of ^{31}P NMR parameters by spinning sideband analysis. All spectra recorded are included in figure 7.1 below.

Before considering the calculated ^{31}P CSA parameters the differences between the isotropic features of the spectra, best displayed in the inset parts of figure 7.1, are worthy of discussion. All complexes apart from the sec-butyl sample clearly show splitting of the peaks with ratios of intensities ~1:4:1 that was evident in previous data

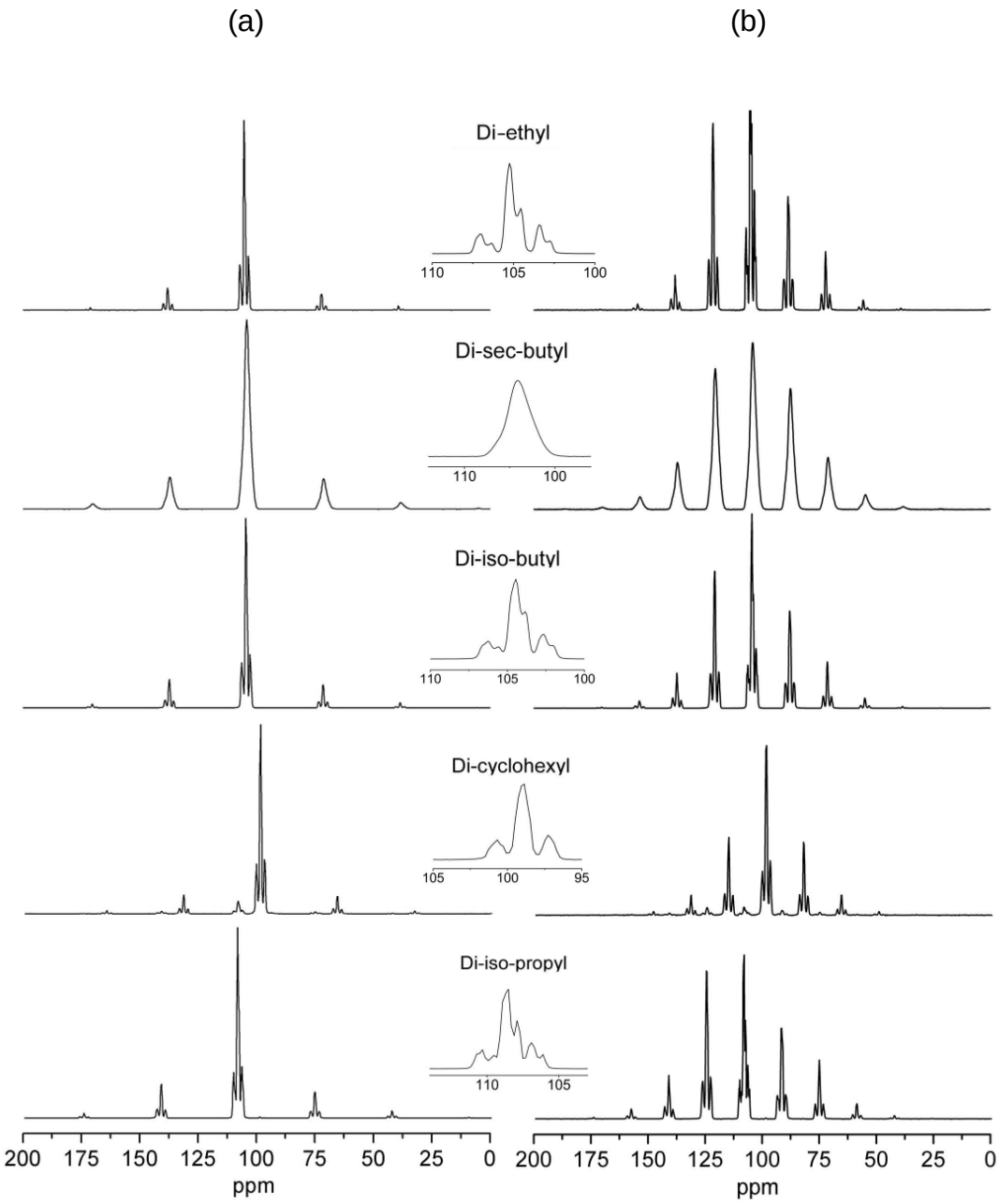

Figure 7.1: Stacked ^{31}P MAS NMR of platinum (II) dialkyldithiophosphate complexes at 121.44 MHz (a): MAS speed 4 kHz, (b): MAS speed 2 kHz, inset: expanded view of isotropic peaks.

and was attributed to ^{195}Pt-^{31}P spin-spin coupling. The natural abundance of ^{195}Pt (33.83%) explains the relative intensities of the satellites as two thirds of the phosphorus nuclei will be neighbouring a non-magnetic platinum nucleus and thus contributing to the central transition while the third of nuclei that are bonded to a ^{195}Pt

nucleus are split between the two satellite peaks by the J-coupling interaction. The polymorphism observed in the cyclohexyl sample is explained as a sample purity issue that occurred in a precipitate from aqueous solution. The signals at lower ppm are from the α-form and the higher shift signals are from the β-form. Fitting of both sets of signals in DMfit [112] suggests a 24:1 ratio of intensity between the α and β forms. The further splitting of all three peaks observed in several of the complexes is likely attributable to the spinning angle of the probe being slightly off the magic angle as similar splitting is not seen in [75-76]. While only a single wide feature is observed in the spectrum of the sec-butyl complex the shape and asymmetry of the spectrum suggests a J-coupled split signal that is broadened to a much greater extent than the spectra of the other complexes. It is proposed that this is caused by a superposition of signals from molecular polymorphs differing in the cis-trans polymorphism of the four butyl groups of the molecule. The six possible configurations are displayed in table 7.3 and discussed in more detail below.

Inspection of the spinning sideband intensity distribution of the ^{31}P MAS NMR spectra of all the complexes suggests a nearly rhombic symmetry of the chemical shift tensors of all the complexes. A statistical estimation of the ^{31}P CSA parameter was made by plotting χ^2 diagrams of δ_{aniso} and η from spinning sideband analysis. The range of values η = 0.72 - 0.95 obtained for all but the ethyl complex suggest a configuration close to a perfectly rhombic arrangement (η = 1). A general trend of increasing η with larger ligand size is observed. The values of δ_{aniso}, some of which have already have been reported in [76], are all the lowest of any metal dialkyldithiophosphates that have been reported [76] indicating that they have the smallest SPS angles [118].

Compound	δ_{iso}, ppm	δ_{aniso}, ppm	η	$^{2}J_{195Pt-31P}$, Hz
$Pt\{S_2P(O\text{-}C_2H_5)_2\}_2$	105.0	-35.1 ± 0.01	0.54 ± 0.01	446 ± 0.5
$Pt\{S_2P(O\text{-}sec\text{-}C_4H_9)_2\}_2$	104.1	-43.2 ± 0.01	0.88 ± 0.02	404 ± 0.6
$Pt\{S_2P(O\text{-}iso\text{-}C_4H_9)_2\}_2$	104.3	-38.8 ± 0.01	0.72 ± 0.01	443 ± 0.5
$Pt\{S_2P(O\text{-}cyclo\text{-}C_6H_{11})_2\}_2$	99.0	-30.8 ± 0.01	0.92 ± 0.02	433 ± 0.5
$Pt\{S_2P(O\text{-}iso\text{-}C_3H_7)_2\}_2$	108.5	-42.7 ± 0.01	0.75 ± 0.02	431 ± 0.7

Table 7.1: ^{31}P chemical shift anisotropy parameters determined by analysis of the spinning sidebands of spectra in figure 7.1.

7.3 ^{195}Pt NMR

Even at relatively low field strength for modern instruments (7.05 T) the width of the ^{195}Pt chemical shift anisotropy of platinum (II) dialkyldithiophosphates (~300 kHz) greatly exceeds the excitation width that the probe coil is capable of (~75 kHz FWHM). This has meant that up to this point ^{195}Pt NMR of these compounds has been incomplete or used a MAS frequency stepping method [75-78]. A field sweep approach as outlined in Section 2.3.4.2 allows the automatic and quantitative (given certain conditions outlined in the sections mentioned) acquisition of the entire CSA lineshape. The field sweep spectra of all five samples are show in figure 7.2 along with a theoretical model of the CSA lineshape assuming an entirely static molecule. The models were created in DMfit [112]. All ^{195}Pt spectra were processed with 20 kHz of exponential broadening and this was also applied to the models.

In contrast to the ^{31}P data in figures 7.1 , the lineshapes of the ^{195}Pt static NMR spectra of all the complexes correspond to an almost axially symmetric chemical shift tensor. This is indicated by the much smaller difference between δ_{11} and δ_{22} than between δ_{11} and δ_{33}. For a fully axially symmetric tensor $\delta_{11} = \delta_{22}$. The spectra of all five complexes are of a similar form to the spectrum of single-crystal Cooperite (natural PtS) and suggest that the platinum is held in a configuration close to the square chromophores (PtS_4) found in Cooperite. However, the δ_{33} component of

the ^{195}Pt of the CSA for these complexes is much smaller than is observed in PtS, leading also to a substantial difference in the isotropic shifts. This suggests that in all the complexes considered there is greater electron shielding in the direction perpendicular to the PtS_4 chromophore than is found in Cooperite. This increased shielding could be attributed to the presence of the alkyl ligands which are positioned outside the axial plane of symmetry of the PtS_4 chromophores and the manner in which the molecules arrange themselves such that offset stacks of chromophores are created which differ from the aligned stacks of the chromophores found in Cooperite.

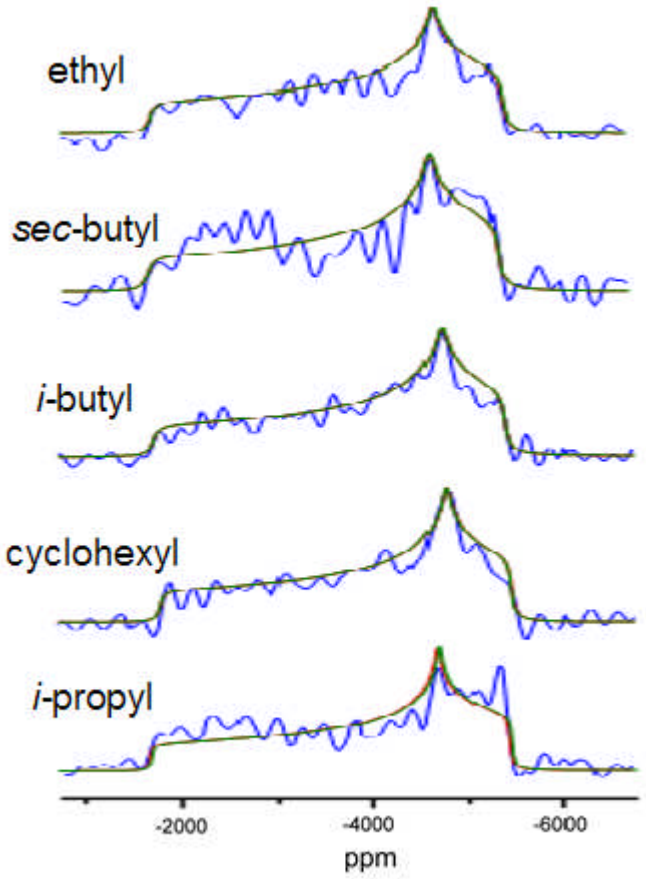

Figure 7.2: Stacked plot of ^{195}Pt field sweep NMR of all complexes, showing both experimental data (blue), and modelled CSA fits (green).

In general, fitting of the CSA lineshapes in DMfit was possible with good agreement for all complexes but the sec-butyl sample. In this case the averaged lineshape is indicative of greater disorder which is also indicated by a T_1 relaxation

time an order of magnitude shorter than the other samples. Complex I has the greatest degree of agreement between experimental spectrum and model.

he iso-butyl, cyclo-hexyl and iso-propyl complexes offer good agreement with their fits, but show some of the same signs of disorder as the sec-butyl complex, which could be attributed to broadened by dipolar coupling with protons. Their peaks at the δ_{22} position are not as intense as predicted by the model, but this discrepancy is not as large as that observed in the sec-butyl complex.

Compound	δ_{iso}, ppm ± 12	δ_{aniso}, ppm ± 30	η ± 0.01
$Pt\{S_2P(O\text{-}C_2H_5)_2\}_2$	-4018	3327	0.31
$Pt\{S_2P(O\text{-}sec\text{-}C_4H_9)_2\}_2$	-3959	3364	0.33
$Pt\{S_2P(O\text{-}iso\text{-}C_4H_9)_2\}_2$	-3958	3339	0.30
$Pt\{S_2P(O\text{-}cyclo\text{-}C_6H_{11})_2\}_2$	-3891	3351	0.33
$Pt\{S_2P(O\text{-}iso\text{-}C_3H_7)_2\}_2$	-3964	3364	0.33

Table 7.2: ^{195}Pt chemical shift anisotropy parameters determined by the fits from figure 7.2. Errors supplied by DMfit except for $Pt\{S_2P(O\text{-}sec\text{-}C_4H_9)_2\}_2$.

As would be expected from visual inspection of the models in figure 7.2, the fit parameters are quite similar to one another. Nevertheless a couple of useful observations can be made from the data in table 7.2. The iso-butyl, cyclo-hexyl and iso-propyl complexes were observed to have very similar values of δ_{aniso} within 12 ppm of one another. The ethyl sample has a smaller anisotropy and corresponding more negative isotropic shift which perhaps indicates closer packing in the direction perpendicular to the PtS_4 chromophore which would follow intuitively from smaller ligand size. The sec-butyl sample has the largest anisotropy which could correlate to a weaker shielding from looser molecular packing which in turn could explain the greater disorder which is inferred from its ^{195}Pt spectrum and spin-lattice relaxation time. While other complexes are assumed to have centrosymmetric structures [75]

with identical ligands allowing uniform and close packing of molecules in the solid, the ligands of the sec-butyl sample experience cis-trans polymorphism. While each sec-butyl group can be one of two polymorphs, molecules can be one of six different arrangements which are outlined below in table 7.3.

Polymorph of $Pt\{S_2P(O\text{-}C_4H_9)_2\}_2$	Orientation of *sec*-butyl groups			
	1	2	3	4
1	cis	cis	cis	cis
2	cis	cis	cis	trans
3	cis	cis	trans	trans
4	cis	trans	cis	trans
5	cis	trans	trans	trans
6	trans	trans	trans	trans

Table 7.3: Table of polymorphs of $Pt\{S_2P(O\text{-}C_4H_9)_2\}_2$ groups 1 and 2 are taken to be on the same ligand as are 3 and 4.

Without an identical ligand structure, close regular packing of molecules becomes less likely and the greater disorder and mobility evidenced by both ^{31}P and ^{195}Pt NMR is the result.

The values of the asymmetry of the ^{195}Pt CSA of all five complexes, η, have also been estimated for the first time and show little variation and no apparent correlation with δ_{aniso}. This is in agreement with XRD data which suggests a lack of tetrahedral distortion of the PtS_4 chromophore in the complexes which have been previously studied.

7.4 Conclusions

The ^{31}P and ^{195}Pt NMR chemical shift anisotropies (CSAs) of five platinum (II) dialkyldithiophosphate complexes have been determined. The ^{31}P NMR spectra of the ethyl and sec-butyl complexes have not been previously presented and none of the samples have had their full ^{195}Pt CSAs characterised until now. The ^{31}P CSA parameters of the sec-butyl and ethyl complexes continued the trend for platinum dialkyldithiophosphates to have the smallest of the known anisotropies and therefore SPS angles. A low (0.55) and high (0.88) value for the asymmetries of the ethyl and sec-butyl complexes respectively. in conjunction with existing data suggests some link between large ligand size and higher asymmetry values. Fitting of the ^{195}Pt CSA results in five similar sets of parameters with the most striking difference being the disorder in the sec-butyl sample. This is a result of cis-trans polymorphism of the ligands and therefore irregular packing of molecules in the solid-state.

Chapter 8

8. Conclusions

Chapters 4 to 7 each contained solid-state NMR studies of a material or class of materials which are of commercial and industrial interest. While the analysis of the NMR data and the information it provides about the materials under investigation was summarised at the end of each chapter, the general conclusions from the thesis as a whole and implications for further study in each area will be covered here.

8.1 Solid State NMR as a Probe of Complex Applied Materials

This thesis has demonstrated practically many of the advantages inherent in a multinuclear NMR approach to solid materials which are multiphasic, amorphous or both. The elemental specificity of the technique has proven useful in the study of the ionomer layers on fuel cell catalyst inks, which can be a single atomic layer thick and make up very little of the total volume of the solid. That this interface between ionomer and catalyst appears to also contain a form of bound water whose properties are dependent on the structure of the ionomer layer makes it an even greater challenge for an analytical technique to match the information provided by NMR. Indeed the only studies of this interface known by the author are TEM images [50] which can provide complimentary information such as the uniformity and thickness of the ionomer layer but could not replace the work found in chapter 4.

This specificity has also facilitated the separate study of the network forming elements within the BN1 glass-ceramic system. Each of the main phases formed as the ceramic is heat treated to higher temperatures could be detected and identified and it could be observed that aluminium, silicon and boron entered crystalline phases at different rates to one another and to the bismuth-niobate phase previously reported. While the bismuth-niobate crystals are of prime concern for the dielectric properties required for its application, the other ingredients make up approximately 45% of the molar composition of the ceramic and are necessary for initial glass formation. While electron dispersive spectroscopy (EDS) can provide elemental compositions of specific phases within the ceramic [80] it cannot supply the structurally specific data which is representative of the entire sample as NMR or XRD can. In this case the analysis of XRD data [80] is complicated by the overlapping reflections of many

amorphous and crystalline phases while studies of each nucleus by NMR reduces the number of unknowns that must be interpreted from a single spectrum.

The BN1 system was not the only one to benefit from the complementary information gathered from a multinuclear study. ^{19}F and ^{1}H NMR of proton exchange membrane fuel cell ionomers combined to give a more complete picture of how variations in the structure and dynamics of the water and ionomer in a membrane are linked to one another. Meanwhile, the main advantage of the study of PEMFC catalysts by solid-state field sweep NMR is the quantitative local information that can be gathered about specific areas of a particle. This has obvious advantages as catalysis is a surface phenomenon and the shape of particles as well as the location of metals in bimetallic systems are key issues for those developing catalysts for the future. The ^{195}Pt Knight shift measured by NMR does not only provide location information on nuclei found in nanoparticles but it also perturbed by electronic changes caused by adsorption and alloying effects providing additional value and scope for application [96]. The chemical shift anisotropy (CSA), another interaction measured by solid-state NMR, also provides detailed information on the electronic environment around a nucleus. The measurement of the ^{31}P and ^{195}Pt CSA of platinum (II) dialkyldithiophosphates in Chapter 7 is a first step to understanding why they form different structures to similar nickel and lead based complexes.

8.2 Proposed Further Study

The aim of chapter 4 was to determine which solid-state NMR experiments were best suited for the study of differences in the perfluoroinonomers used in polymer electrolyte membrane fuel cells and what information they could provide to aid the development of membrane electrode assemblies. The scope of the investigation included comparing different ionomer structures, equivalent weights, membrane casting methods and ionomer layers on catalyst inks. ^{1}H, ^{19}F and ^{19}F-^{13}C CP experiments were carried out for some or all of the samples in combination with different sample preparation techniques. Now that the procedures and techniques best suited to the study and comparison of ionomer membranes and layers have been developed they can easily be applied to wider sample sets to confirm correlations between the preparation variables shown to effect NMR spectra. Alongside

measurements of conductivity and performance a more systematic approach to the tuning of MEA preparation can be developed with the aid of routine solid-state NMR now available to Johnson-Matthey on site. The work of chapter 4 also provides a basis for the use of ^{19}F NMR to measure the equivalent weight and sidechain structure of any ionomer provided. Perhaps the most important consequence to fuel cell development is the need to expand and understand the study ionomer layers on catalysts to confirm the links between the type and concentration of solution and the morphology of ionomer layer and the water bound within it. As some ionomer layers did not appear to contain water associated with acid groups, a condition for the high proton conductivity normally provided by hydrated Nafion, new insights into optimising conductivity across the MEA are possible.

Further study comparing the oxidised regions of the ^{195}Pt spectra in chapter 5 could determine the cause of intensity variations and the apparent lack of oxidation of the 5nm sample. Controlling both the platinum content and particle size in tandem across a larger sample set would allow the determination of which of these variables are responsible for the symmetry and oxidation effects observed. Whether the differences are caused by surface properties linked to particle size, particle shape or whether the higher platinum loading of 60 % discourages oxidation. This study would be important to the development of fuel cells as it mirrors the debate on whether the particle size effect on catalyst activity is caused by the type of surface or the proximity of particles to one another [51-54]. Answers to one question could well inform the other.

The development of a complete and quantitative NMR technique for ^{195}Pt of nanoparticles has implications for bimetallic systems as well as the purely platinum catalysts considered in chapter 5. The position of the platinum within bimetallic particles and any alloying effects are known to alter the Knight shift [96] and for the first time the proportion of platinum in different states can be calculated with confidence that all material will be accounted for.

There is greater scope for application of SSNMR to the development and understanding of the BN1 glass-ceramic system by applying ^{93}Nb studies to the sample range covered in chapter 6. This work has already begun in the laboratory.

The effect of any alterations to the composition of the as cast glass could be more readily understood with the aid of the NMR techniques and analysis found in this work.

Finally, now that the ^{195}Pt NMR chemical shift anisotropy of a selection of platinum (II) dialkyldithiophosphates have been determined by field sweep NMR they can be benchmarked against the results from more conventional wideline techniques. The ^{31}P and ^{195}Pt CSA parameters can then be used to validate density functional theory studies of these complexes, which could shed important light on the difference in bonding and ligand configurations found between different metal ions in dialkyldithiophosphate compounds. All of the above work is being undertaken in the laboratory.

References

1. U. Bossel, *The Birth of the Fuel Cell* (European Fuel Cell Forum, 2000)
2. D. Hart, *J. Power Sources* **86**, 23 (2000)
3. S. G. Chalk, J. F. Miller and F. W. Wagner, *J. Power Sources* **86**, 40 (2000)
4. A. U. Dufour, *J. Power Sources* **71**, 19 (1998)
5. P. Hoffmann, *Hydrogen and Fuel Cell Letter 15* (2000)
6. P. Hoffmann, *Hydrogen and Fuel Cell Letter 13* (1998)
7. L. Carrette, K.A. Friedrich and U. Stimming, *Fuel Cells* **1**, 5 (2001)
8. K. Kordesch, J. Gsellmann, M. Cifrain, S. Voss, V. Hacker, R. R. Aronson, C. Fabjan, T. Hezje and J. Daniel-Ivad, *J. Power Sources* **80**, 190 (1999)
9. A.J. Appleby, Sci. Am. **45**, 281 (1999)
10. T. R. Ralph and G. A. Hards, *Cbem. Ind,* **9**, 337 **(**1998)
11. S. Srinivasan, *Fuel Cells: From Fundamental to Applications* (Springer, New York, 2006)
12. P. Costamagna and S. Srinivasan, *J. Power Sources* **102**, 242 (1999)
13. P. Costamagna and S. Srinivasan, *J. Power Sources* **102**, 253 (1999)
14. T. R. Ralph and M. P. Hogarth, *Platinum Metals Rev.* **46**, 3 (2002)
15. B. N. Grgur, N.M. Markovic and P. N. Ross, *Electrochimica Acta* **43**, 3631 (1998)
16. B. N. Grgur, N.M. Markovic and P. N. Ross, *J. Electrochem. Soc.* **146**, 1613 (1999)
17. A Küver and K. Potje-Kamloth, *Electrochimica Acta* **43**, 2527 (1998)
18. A Küver and W. Vielstich, *J. Power Sources* **74**, 211 (1998)
19. M. Cappadonia, J. W. Erning, S. M. Saberi Niaki and U. Stimming, *Solid State Ionics, Diffusion & Reactions*, 77 (1995)
20. T. D. Gierke, G. E. Munn and F. C. Wilson, J. *Polym. Sci. Polym. Phys.* **19**, 1687
21. C. Yang, P. Costamagna, S. Srinivasan, J. Benziger and AB Bocarsly, *J. Power Sources* **103**, 1 (2001)
22. C. Heitner-Wirguin, *J. Membrane Sci.* **120**, 1 (1996)
23. K. M. Nouel and P. S. Fedkiw, *Electrochimica Acta* **43**, 2381 (1998)
24. F. N. Buchi B. Gupta, O. Haas and G. G. Scherer, *J. Electrochem. Soc.* **142**, 3044 (1995)
25. F. N. Buchi B. Gupta, O. Haas and G. G. Scherer, *Electrochimica Acta* **40**, 345 (1995)

26. T. Lehtinen, G. Sundholm, S. Holmberg, F. Sundholm, P. Björnbom and M. Bursell, *Electrochimica Acta* **43**, 1881 (1998)
27. Q Chen, K. Schmidt-Rohr, *Macromol. Chem. Phys.*, **208**, 2189 (2007)
28. E. M. Lee, R. K. Thomas A. N. Burgess, D. Y. Barnes, A. K. Soper, and A. R. Rennil, *Macromol.* **25**, 397 (1992)
29. G. Xu, *Polymer* **25**, 3106 (1992)
30. T. D. Gierke, G. E. Munn, F. C. Wilson, *J. Polym. Sci. Pol. Phys.* **19**, 1687 (1981)
31. K. Schmidt-Rohr and Q Chen, *Nature Materials* **9**, 75 (2008)
32. P. Costamagna, S. Grosso, R Di Felice, *J. Power Sources* **178**, 537 (2008)
33. K. A. Mauritz, R. B. Moore, *Chem. Rev.* **104**, 4637 (2004)
34. N. G. Boyle, J. Michael, D. Coey, A. Meagher, V. J. McBrierty, Y. Nakano and W. J. Macknight, *Macromol.* **17** 1331 (1984)
35. G. Xu, Y. S. Pak, *Solid State Ionics* **50**, 339 (1992)
36. A. Y. Nosaka, Y. Nosaka, *J. Power Sources* **180**, 733 (2008)
37. A. Y. Nosaka, Y. Nosaka, *Meet. Abstr. Electrochem. Soc.* **902**, 958 (2009)
38. E. H. Sanders, K. A. McGrady, G. E. Wnek, C. A. Edmondson, J. M. Mueller, J. J. Fontanella, S. Suarez, S. G. Greenbaum, *J. Power Sources* **129**, 55 (2004)
39. T. A. Zawodzinski Jr., M. Neeman, L. O. Sillerud, S. Gottesfeld, *J. Phys. Chem.* **95**, 6040 (1991)
40. A. Y. Nosaka, S. Watanabe, I. Toyoda, Y. Nosaka, *Macromol.* **39**, 4425 (2006)
41. J. Zhang, M. V. Giotto, W. Wen, A. A. Jones, *J. Membrane Sci.* **269**, 118 (2006)
42. G. Ye, C. M. Mills, G. R. Goward, *J. Membrane Sci.* **319**, 238 (2008)
43. G. Ye, N. Janzen, G. R. Goward, *Macomol.* **39**, 3283 (2006)
44. G. Ye, A. Hayden, G. R. Goward, *Macromol.* **40**, 1529 (2007)
45. S. F. Dec, R. A. Wind, G. E. Maciel, *Macromol.* **20**, 2754 (1987)
46. Q. Chen and K. Schmidt-Rohr, *Macromol.* **37**, 5995 (2004)
47. Q. Chen and K. Schmidt-Rohr, *Macromol. Chem. Physic.* **208**, 2189 (2007)
48. K. A. Page, W. Jarrett, R. B. Moore, *J. Polym Sci Pol Phys.* **45**, 2177 (2007)
49. S.-F. Liu and K. Schmidt-Rohr, *Macromol.* **34**, 8416 (2001)
50. T. R. Ralph and M. P. Hogarth, *Platinum Metals Rev.* **46**, 117 (2002)
51. M. L. Sattler and P. N. Ross, *Ultramicroscopy* **20**, 21 (1986)
52. L. J. Bregoli, *Electrochim. Acta* **23**, 489 (1978)
53. Y. Takasu, N. Ohashi, X.-G. Zhang, Y. Murakami, H. Minagawa, S. Sato and K. Yahikozawa, *Electrochim. Acta* **41**, 2595 (1996)

54. M. Watanabe, H. Sei and P. Stonehart, *J. Electroanal. Chem.* **261**, 375 (1989)
55. A. I. Frenkel, C. W. Hills and R. G. Nuzzo, *J. Phys. Chem. B* **105**, 12689 (2001)
56. R. E. Benfield, *J. Chem. Soc. Faraday. Trans.* **88**, 1107(1992)
57. D. Bazin and J. J. Rehr, *J. Phys. Chem. B* **107**, 12398 (2003)
58. Y. Zhang, M. L. Toebes, A van der Eerden, W. E. O'Grady, K. P. de Jong and D. C. Koningsberger, *J. Phys. Chem. B* **108**, 18509 (2004)
59. H. E. Rhodes, P.-K. Wang, H. T. Stokes and C. P. Slichter, *Phys. Rev. B* **26**, 3559 (1982)
60. H. E. Rhodes, P.-K. Wang, C. D. Makowka, S. L. Rudaz, H. T. Stokes and C. P. Slichter, *Phys. Rev. B* **26**, 3569 (1982)
61. H. T. Stokes, H. E. Rhodes, P.-K. Wang, and C. P. Slichter, *Phys. Rev. B* **26**, 3575 (1982)
62. J. P. Bucher and J. J. van der Klink, *Phys. Rev. B* **38**, 11038 (1988)
63. J. P. Bucher, J. Buttet and J. J. van der Klink, Surf. Sci. **214**, 347 (1989)
64. J. Fraissard, *Catal. Today* **51**, 481(1999)]
65. Y. Tong, B. S. Zelakiewicz, B. M. Dy and A. R. Pogozelki, *Chem. Phys. Lett.* **406**, 137 (2005)
66. Y. Tong, P. K. Babu, A. Wieckowski and E. Oldfield, *Chem. Phys. Lett.* **361**, 183 (2002)
67. Y. Tong, C. Rice, N. Godbout. A. Wieckowski and E. Oldfield, *J. Am. Chem. Soc.* **121**, 2996 (1999)
68. Y. Tong, C. Rice, A. Wieckowski and E. Oldfield, *J. Am. Chem. Soc.* **122**, 11921 (2000)
69. B. M. Rush, J. A. Reimer and E. J. Carins, *J. Electrochem. Soc.* **148**, A137 (2001)
70. C. Lu, C. Rice, R. I. Masel, P. K. Babu, P. Waszczuk, H. S. Kim, E. Oldfield and A. Wieckowski, *J. Phys. Chem. B* **106**, 9581 (2002)
71. K. W. Feindel, S. H. Bergens and R. E. Wasylishen, *Phys. Chem. Chem. Phys.* **9**, 1850 (2007)
72. A.-C. Larsson, A. V. Ivanov, O. N. Antzutkin and W. Forsling, *J. Colloid Interf. Sci.* **327**, 370 (2008)
73. A. V. Ivanov, O. N. Antzutkin, A.-C. Larsson, M. Kritikos and W. Forsling, *Inorg. Chim. Acta* **315**, 26 (2001)
74. M. Gianini, W. R. Caseri, V. Gramlich and U. W. Suter, *Inorg. Chim. Acta*, **299**, 199 (2000)

75. A. V. Ivanov, I. A. Lutsenko, M. A. Ivanov, A. V. Gerasimenko and O. N. Antzutkin, *Russ. J. Coord. Chem+* **34**, 584 (2008)
76. A. V. Ivanov, V. I. Palazhchenko, V. E. Strikha, O. N. Antzutkin and W. Forsling, *Dokl. Earth Sci.* **410**, 114 1(2006)
77. V. I. Rozhdestvina, A. V. Ivanov, M. A. Zaremba, O. N. Antzutkin and W. Forsling, *Crystallogr Rep+* **53**, 391 (2008)
78. A. V. Ivanov, T. A. Rodina, M. A. Ivanov, A. V. Gerasimenko and O. N. Antzutkin, *Dokl. Phys. Chem.* **423**, 311 (2008)
79. M. Mirsaneh, O. P. Leisten, B. Zalinska and I. M. Reaney, *Adv. Funct. Mater.* **18**, 2293 (2008)
80. M. Mirsaneh, O. P. Leisten, B. Zalinska and I. M. Reaney, *Unpublished*
81. W. L. Konijnendijk, *The Structure of Borosilicate Glasses*, (Phillips Res. Repts. Suppl, 1975)
82. M. E. Milburg and C. R. Peters, *Phys. Chem. Glasses* **4**, 99 (1969)
83. C. Jager, W. Muller-Warmuth, C. Mundus and L. van Wullen, *J. Non-Cryst Solids* **149**, 209 (1992)
84. R. L. Mozzi and B. E. Warren, *J. Appl. Cryst.* **3**, 251 (1970)
85. J. Krogh-Moe, *J. Non-Cryst Solids* **1**, 269 (1969)
86. P. J. Bray and J. G. O'Keefe, *Phys. Chem. Glasses* **4**, 37 (1963)
87. A. C. Wright, N. M. Vedishcheva and B. A. Shakhmatkin, *J. Non-Cryst Solids* **192-193**, 92 (1995)
88. R. Gresch, W. Muller-Warmuth, H. Dutz, *J. Non-Cryst. Solids* **21**, 31 (1976)
89. B. C. Bunker, R. J. Kirkpatrick, R. K. Brow, G. L. Turner and C. Nelson, *J. Am. Ceram. Soc.* **74**, 1430 (1991)
90. H. Yamashita, K. Inoue, T. Nakajin, H. Inoue and T. Maekawa, *J. Non-Cryst. Solids* **331**, 128 (2003)
91. Z. Gan, J. Am. Chem. Soc. **122**, 3242 (2000)
92. A. Samoson, E. Lippmaa and A. Pines, Mol. Phys. **65**, 1013 (1990)
93. A. Medek, J. S. Harwood and L. Frydman, J. Am. Chem. Soc. **117**, 12779 (1995)
94. M. H. Levitt, *Spin Dynamics: Basics of Nuclear Magnetic Resonance*, (Wiley, Chichester, 2001)
95. R. K. Harris, *Nuclear Magnetic Resonance Spectroscopy: A Physiochemical View*, (Pitman, London, 1983)
96. J. J. Van Der Klink, *Advances in Catalysis* **44**, 2 (1999)

97. J. R. L. Priqueler, I. S. Butler, F. D. Rochon, *Appl. Spectrosc. Rev.* **41**, 185 (2006)
98. S. Meiboom and D. Gill, *Rev. Sci. Instrum.* **29**, 688 (1958)
99. T. Gullion, *J. Magn. Reson*. **89**, 479 (1990)
100. T. Gullion and J. Schaefer, *J. Magn. Reson*. **81**, 196 (1989)
101. W. G. Clark, M. E. Hanson and F. Lefloch and P. Segransan, *Rev. Sci. Instrum.* **66**, 2453 (1995)
102. L. Frydman and J. S. Harwood, *J. Am. Chem. Soc.* **117**, 5367 (1995)
103. A. Medek, L. Frydman and J. S. Harwood, *J. Am. Chem. Soc.* **117**, 12779 (1995)
104. G. Metz, X. Wu and S. O. Smith, *J. Magn Res.* **110**, 219 (1994)
105. A. E. Bennett, C. M. Rienstra, M. Auger, K. V. Lakshmi and R. G. Griffin, *J. Chem. Phys.* **103**, 6951 (1995)
106. F. Bloch, *Phys. Rev.* **111**, 841 (1958)
107. X. Filip, C. Tripon and C. Filip, *J. Magn. Res.* **176**, 239 (2005)
108. A. L. Patterson, *Phys. Rev.* **56**, 978 (1939)
109. J. W. Carlson, *J. Magn. Reson.* **78**, 563 (1988)
110. J.-P. Amoureux, C. Fernandez and S. Steuernagel, *J. Magn. Reson. A* **123**, 116 (1996)
100. K. A. Mauritz and R. B. Moore, *Chem. Rev.* **104**, 4535 (2004)
112. D. Massiot, F. Fayon, M. Capron, I. King, S. Le Calve, B. Alonso, J. O. Durand, B. Bujoli, Z. Gan and G. Hoatson, *Magn. Reson. Chem.* **40**, 70 (2002)
113. L. Ghassemzadeh, M. Marrony, R. Barrera, K. D. Kreuer, J. Maier and K. Muller, *J. Power Sources* **186**, 334 (2009)
114. V. Ladizhansky, G. Hodes and S. Vega, *J. Phys. Chem. B* **104**, 1939 (2000)
115. Y. Y. Tong, T. Yonezawa, N. Toshima and J. J. van der Klink, *J. Phys. Chem.* **100**, 730 (1996)
116. K. J. D. Mackenzie and M. E. Smith, *Multinuclear Solid-State NMR of Inorganic Materials* (Pergamon, Oxford, 2002)
117. J. J. Fitzgerald A. I. Hamza, C. E. Bronnimann and S. F. Dec, *Solid State Ionics* **32/33**, 378 (1988)
118. A.-C. Larsson, A. V. Ivanov, W. Forsling, O. N. Antzutkin, A. E. Abraham and A. C. de Dios, *J. Am. Chem. Soc.* **127**, 2218 (2005)